Interfacial water at hydrophilic surfaces:

Measurement of force at the Nafion-water interface

Ronnie Das

A dissertation

submitted in partial fulfillment of the

requirements for the degree of

Doctor of Philosophy

University of Washington

2012

Reading Committee:

Gerald H. Pollack, Chair

Henry C. Lai

Eric J. Seibel

Program Authorized to Offer Degree:

Bioengineering

University of Washington

Abstract

Interfacial water at hydrophilic surfaces:

Measurement of force at the Nafion-water interface

Ronnie Das

Chair of the Supervisory Committee:

Professor Gerald H. Pollack

Department of Bioengineering

On the microscopic scale, water is complex due to its unique molecular structure and bonding capabilities. This interfacial water has been studied for nearly 200 years, since Helmholtz first proposed his model of water at a charged surface (1850s). In biology, charged surfaces are everywhere and in addition, are hydrophilic, rough and irregular in geometry. These features contribute to interfacial water's spectroscopic, electrical and mechanical distinctiveness from bulk water. While the ordering and extent of interfacial water from a surface has a long, controversial history, long-range water ordering on the hundreds of nanometers to hundreds of microns scale has been confirmed and measured at a variety of biological interfaces and next to many hydrogels and hydrophilic surfaces. One hypothesis for such long-range ordering is called the exclusion zone (EZ). EZs are found next to many hydrophilic surfaces and are characterized by the exclusion of microsphere suspensions, colloids, dyes and some solutes from boundary layers 100-300 μm in thickness. In this dissertation, the EZ phenomenon was established to be based on the separation of charge between the

(negatively charged) interfacial EZ water and the bulk (proton-enriched) water zone beyond the EZ (PEZ). We hypothesize, that based on charge separation, there is a significant electrostatic force that exists between the EZ and PEZ. A Nafion tube, which has previously demonstrated robust EZs, was attached to the tip of a custom-fabricated ribbon-like beam sensor. The geometry of the ribbon blocked one side of the Nafion tube and obstructed proton diffusion, thus unilateral force would develop on the contralateral side and be measured by the sensor. When water was added, the tube hydrated and the sensor measured a force of 22 ± 2 μN. pH-sensitive dye measurements of the region confirmed an electrostatic interaction since proton distributions were confirmed to be heavily weighted on the unblocked side of sensor and in the same direction as the measured deflection. Significant electrostatic forces at hydrophilic interfaces in water may play a role in a diverse array of processes in nature, such as protein folding, adhesion and water harvesting.

TABLE OF CONTENTS

LIST OF FIGURES

Figure Number Page

Chatper 1

Chapter 2

Chapter 2 (continued)

Chapter 4

Chapter 5

Chapter 5 (continued)

Chapter 6

LIST OF TABLES

Table Number Page

Chatper 5

ACKNOWLEDGEMENTS

Special thanks to everyone for helping me on this journey to complete this degree.

Rainer Stahlberg, Mark Fauver, Katya Nagornyak and Jeff Magula — the four individuals who knew my work inside and out, provided endless support and wisdom, and who I am honored to call my friends. Thank you! My gratitude knows no bounds. All of you really helped me when things were difficult and I was struggling, both professionally and personally. There is no way I could have done this without you.

Federico Ienna, Hyok Yoo, Albert Kalganov, Bing-Hua Chai, John Myers, Ariel Meyra and Mina Rohani — specific lab members from the past and present. You folks really helped me in so many ways and were so supportive. I am so glad to have grown so much in your presence, absorbing your good energy, advice and friendship.

Dorian Taylor — although the PhD process can be a long period of time in one's life, I feel like the last 2 years was *incredibly* long, intense and insane; yet at times, it was illuminating when we had our discussions. Thank you so much for your counsel and guidance when my research and work went to Mars.

And of course my PhD committee members, Henry Lai, Eric Seibel, Larry Crum and Alberto Aliseda — thank you all for the meetings and advice on how to proceed with my research. I couldn't have asked for a more supportive, wise and scientifically well-balanced group of individuals. Thank you!

Finally, to my advisor Jerry Pollack — thank you for taking me on as your first PhD student in this new field and a graduate student in your lab after over a decade without having one. It has been at times fun, frustrating, eye-opening, interesting, crazy and, now finally, complete. Thanks and take care of yourself.

DEDICATION

Dedicated to my Mom, Dad, Didi and Laura, I love you.

I did it! It's been a long journey.

I couldn't have done any of it without your love and support.

Chapter 1: Introduction

1.1. Cell water, protein and charged surfaces

Dominated by beautiful, abundant oceans on the surface, planet Earth is like a giant cell floating in space. And while most of its continents have been explored by man, many mysteries of our planet still remain in the vast, unknown depths of the ocean water.

Figure 1: Earth as viewed from the International Space Station in high orbit.

Like the Earth, 75-80% of an average cell constitutes water; 18-20% is protein. Although much is known on the structure and function of protein in the cell, there remain many unanswered questions pertaining to the interface where water meets the protein's surface. These questions are central to our understanding of the most fundamental

biological processes, such as protein folding[1] (**figure 2a**), self-assembly[2], hydration[3] (**figure 2b**) and hydrophilicity[4].

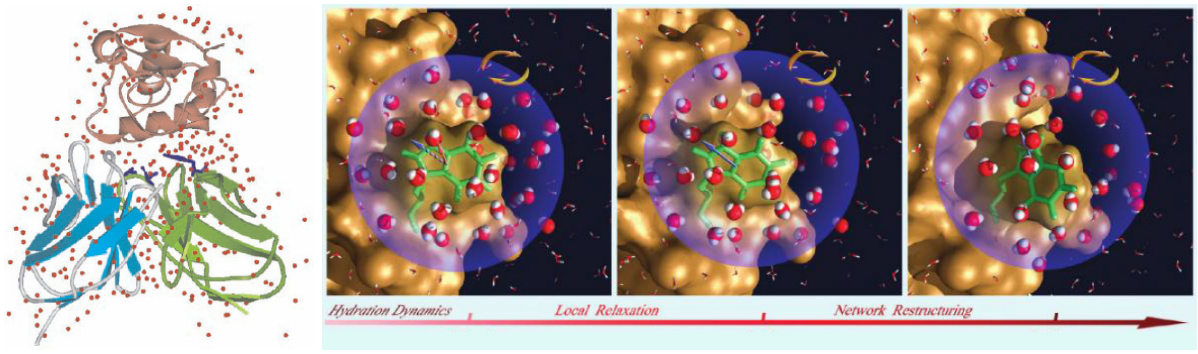

a b

Figure 2: Water and protein interactions. a) Stick diagram of the hydrogen bonding between interfacial water and a protein surface undergoing conformation changes[1]. b) Simulated Molecular Dynamics study of water molecules within the hydration layer of a model apomyoglobin protein[3].

Water's important and complementary role in the cell is immediately recognized when one simply considers size, or even the molecular crowding within the intracellular matrix and the steric interactions of proteins[5-8]. In the cytosol, proteins range in size from 1-1000 nm[9-10]. In comparison to the smallest protein, the water molecule is about 5 times smaller, or approximately 2.5 Å (**figure 3a**). To comprehend these dimensions, if a person 1.7 m tall grew to a height that reached the moon, then relative to this individual, the water molecule would be a small ping-pong ball and the largest protein a blue whale.

Proteins of all sizes crowd the cell's interior (**figure 3b**), but even with crowding, free space between protein surfaces can still be found. An upper estimate for the linear space between corresponding protein surfaces is about 1-5 nm[5-6], or approximately

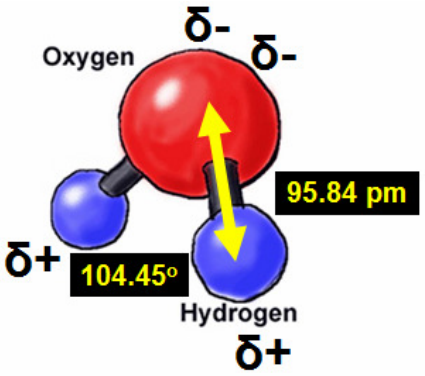

a

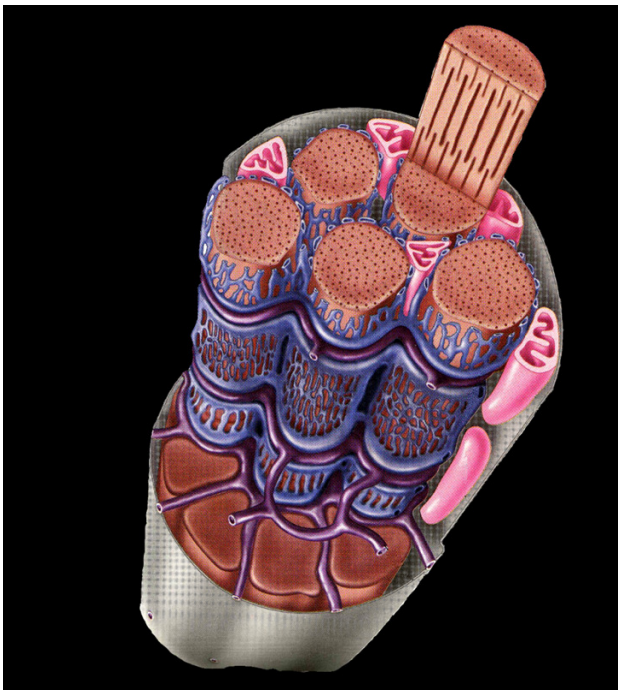

b

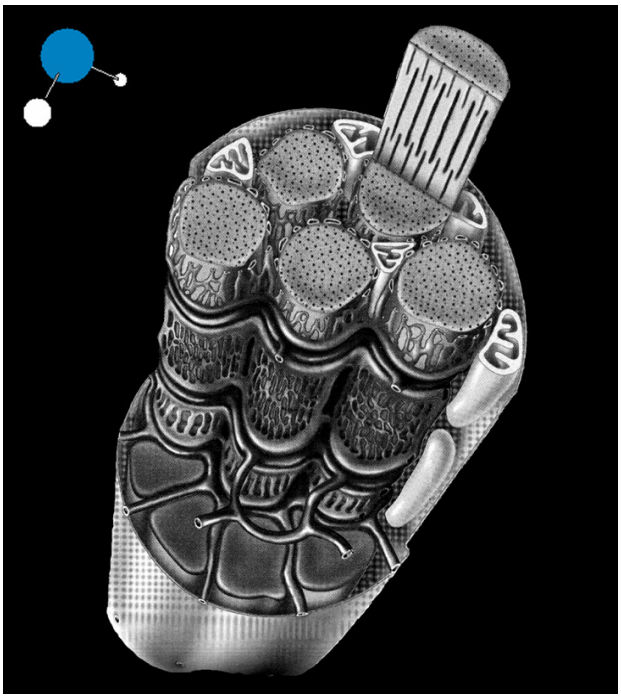

c

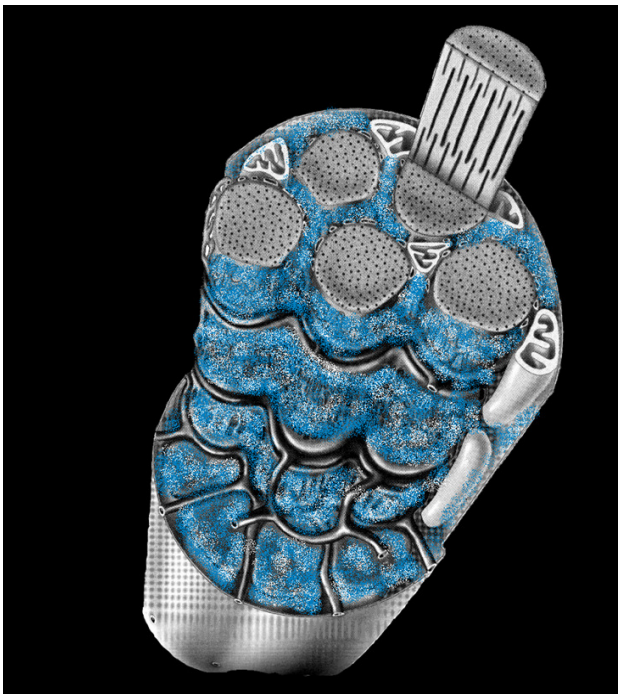

d

Figure 3: The water molecule, cell water and intracellular molecular crowding. a) The water molecule. b-d) Diagrammatic representation of protein crowding in skeletal muscle and the cell water which surrounds the protein surfaces.

5-20 water molecules lined end-to-end. Ordered in layers, water molecules completely surround proteins (**figure 3c-d**) and for a single adsorbed layer, water accounts for as much as 28% of a protein's total weight[11]. Water layers also conform to a protein's molecular structure, which maintains a very high surface area to volume ratio. Consequently, for an average cell 10-15 μm in diameter, a single water layer occupies an area nearly 100 times the cell's outer surface (~80,000 μm^2)[6,12], making the protein-water interface a ubiquitous cell feature.

Water interactions with protein are complex since protein surfaces are highly-charged and irregular in geometry, two qualities which contribute to distinct electrical behavior at the surface. Take first the basic example of a charged conductor with a spherical geometry (**figure 4a**): like-charges electrostatically repel each other throughout the volume of the sphere and cause a distribution of charge at the very surface, commonly referred to as the Gaussian surface of the conductor. In this case, the spherical conductor possesses a constant surface charge density, which in turn is responsible for evenly-spaced, perpendicularly-oriented (with respect to the conductor's surface) electric field lines that are equal in magnitude (**figure 4a**). When the sphere is replaced with a solid cone, charges concentrate at the sharp tip of the cone (**figure 4e**). With a significantly greater electric field strength in comparison to the surface of the original conducting sphere, the tip region is characterized by a high capacity to transfer charge to its surrounding environment. This characteristic is the basis for Benjamin Franklin's lightning rod[13-14], which works in the reverse direction during thunderstorms (**figure 4f**).

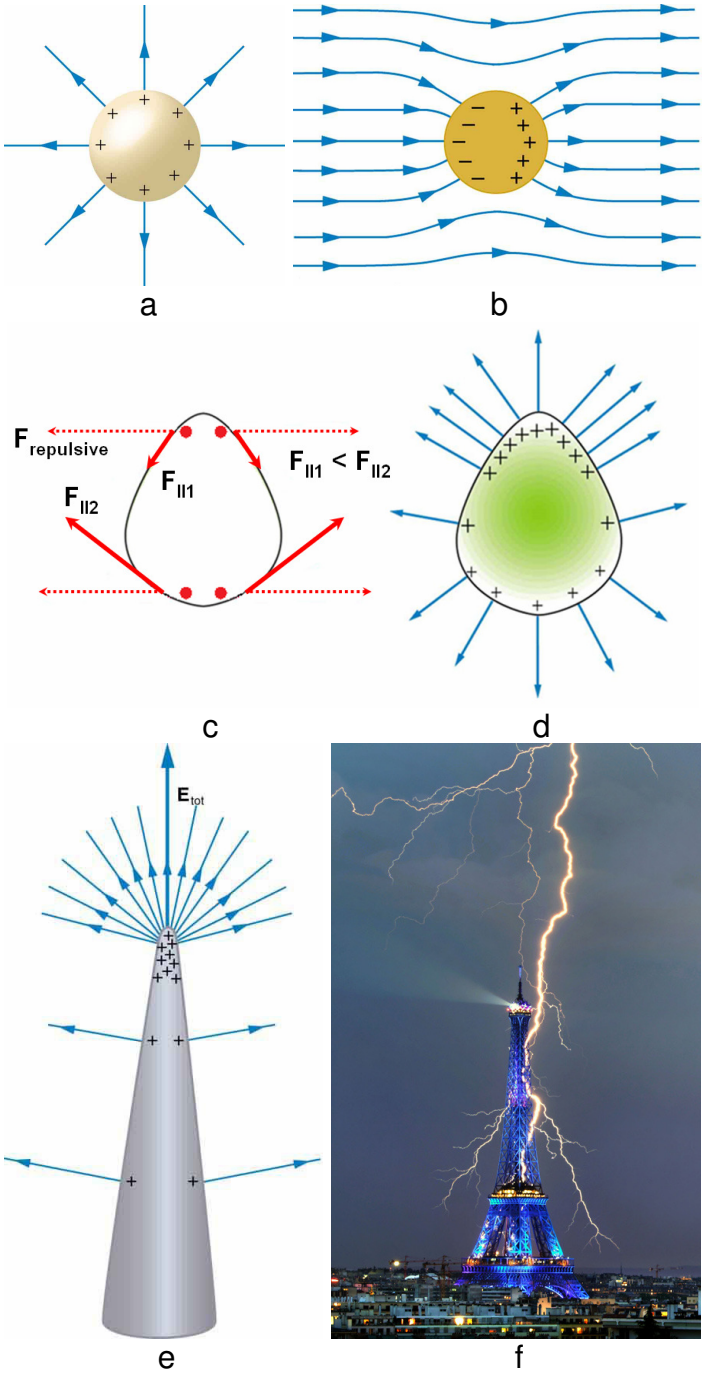

Figure 4: The geometry of charged surfaces and electric field development. a) Excess electric charge on a solid, spherical conductor causes equal electric field lines to develop along the entire outer surface[15]. b) Behavior of a spherical conductor in an externally applied electric field. c) Along a conducting surface, charges repel each other. Repulsion occurs the most within areas of greatest curvature. d) The electric field corresponding to a surface of a given curvature. e) Solid, conducting cones concentrate charges at the tip; thus the magnitude of the electric field is greatest within this region. f) The Eiffel Tower, an example of a large, cone-shaped lightning-rod.

Commonly affixed to the spire of tall buildings, lightning rods prevent harm to people by serving as low impedance conductors, transferring electric charge from lightning strikes to the Earth's ground. If the material of the cone was altered from a conductor to a nonconductor, or a dielectric material, surface charge distribution and electric field development would be unique and difficult to predict.

In nature, most charged surfaces consist of dielectric-like materials that exhibit nonplanar geometries and a share an interface with water. The interface may reside between a water film, or the surface may be immersed altogether in an aqueous environment.

All the same, surface charge and geometry are two critical interfacial components. Their roles at the macroscopic level with water are crucial in many diverse processes including the Gecko's ability to walk up vertical faces to evade predators[16] (**figure 5a-c**), pollen collection between a flower and honey bee[17] (**figure 5d-e**), the harvesting of drinking water out of desert air by the Stenocara beetle[18] (**figure 5f-j**) and the survival of plants at freezing temperatures[19]. These examples not only illustrate the diversity of materials that exist in nature, but they additionally show the multiplicity of charge carriers at the interface and the contrasting physical profiles of surfaces. Both of which reversibly contribute to the distinctiveness of the water environments adjacent to charged surfaces.

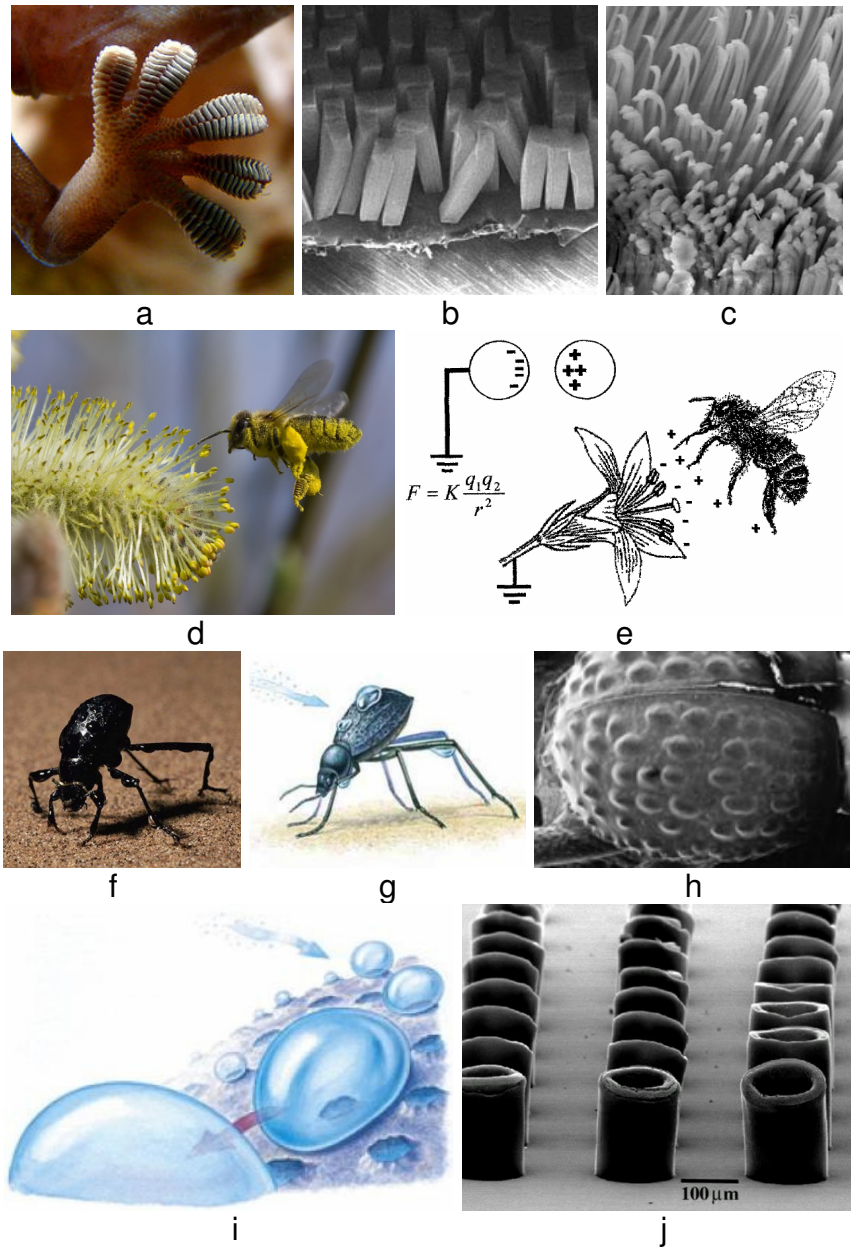

Figure 5: Charged surfaces in nature and the role of water. a) The foot of the Gecko, which can climb up vertical faces to evade predators[20]. b-c) Electron microscopy of the Gecko foot reveals hydrophobic/hydrophilic hairs[16]. d) A honey bee electrostatically attracts pollen from a flower in order to make food and cross-pollinate other plants[21]. e) Significant electrostatic force develops between the flower and honey bee. f) The Stenocara beetle. g, i) Diagrammatically showing how the beetle extracts water from the dry, desert air. h) Electron microscopy of the Stenocara beetle's back illustrates bumps that are highly-charged and hydrophilic[22]. j) An artificially engineered, microfabricated surface to mimic the beetle's water harvesting ability[18].

1.2. Brief history of liquids at charged surfaces and the DLVO theory

The study of liquids adjacent to charged surfaces began in the mid-19th century with the initial work of German physiologist and theoretical physicist Hermann von Helmholtz. Helmholtz believed aqueous solutions at charged metal surfaces were predominantly governed by electrostatic forces and ionic interactions, and modeled a discrete network of molecules based on these principles[23].

In 1860, he postulated that in aqueous solution, ions adsorb in a single charged layer at a metal surface, while an additional, oppositely charged outer layer adsorbs to this initial coating. The two layers thus form a simple capacitor, historically referred to as the "double layer", which over the next 150 years, would be debated, modified and revised by an impressive array of scientists (**figure 6**).

The first major modification of the double layer was based on the work of Scottish botanist Robert Brown, who studied the basis of diffusion (Brownian motion) only 30 years earlier. Diffusion was not formally established until 1905 by Albert Einstein, but Brown's findings were nonetheless incorporated within the initial Helmholtz model as a "diffuse outer layer"[24]. Rather firmly anchored, the outer layer was hypothesized to be governed by both electrostatic and thermal forces, and thus reflected Brown's scientific work on particle motion and thermal activity (**figure 7a**).


Helmholtz
1821-1894


Brown
1773-1858

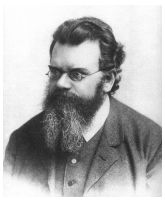
Boltzmann
1844-1906

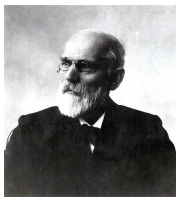
Van der Waals
1837-1923


Derjaguin
1902-1994

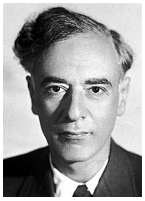
Landau
1908-1968


Verwey
1905-1981


Overbeek
1911-2007

a

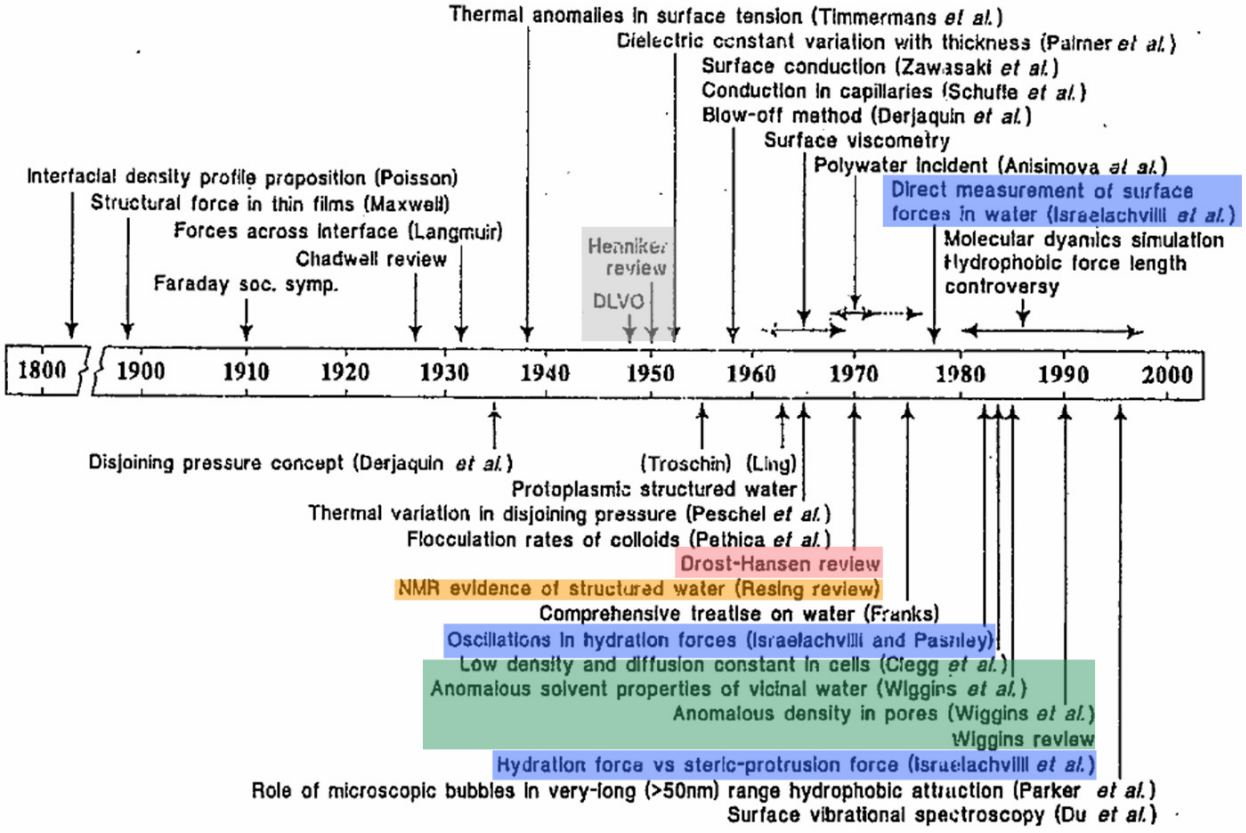

b

Figure 6: History of liquids at charged surfaces. a) Some of the first scientists who set down the fundamentals of the field as well as the authors of the recent DLVO theory. b) Brief timeline of significant points in the conceptual understanding of liquids at charged surfaces. Colored boxes are studies referred to throughout the dissertation[37].

At the time, thermal activity as a whole was also being studied by Austrian physicist Ludwig Eduard Boltzmann. Boltzmann, who was simultaneously working alongside Helmholtz, was attempting to characterize thermal phenomena in his kinetic theory of particles, which had an important additional impact on the double layer model[25].

After the turn of the century, Boltzmann's theories were integrated into the diffuse layer concept by Gouy and Chapman[26-28]. The revised double layer (Gouy-Chapman) model therefore consisted of a single layer of adsorbed charge (called the Helmholtz, or Stern layer) and the diffuse outer layer. The outer layer, governed by the aforementioned forces, was characterized (due to the efforts of Boltzmann) by an electrical potential that decreased with distance from the charged surface (**figure 7a**).

While Gouy and Chapman made further refinements to their model, Johannes Diderik Van der Waals of the Netherlands proved that his theoretical investigations on intermolecular forces were a significant piece in the then current model of aqueous solutions. First presented to the scientific community in 1881, Van der Waals' theoretical work on the interactions of permanent and induced molecular dipoles was recognized as a key development in the behavior of ions and water molecules.

Subsequently, many scientists explored new theoretical techniques to include his findings within the Gouy-Chapman model, but were met with failure due to the complexity of the equations. After several decades, the necessary theoretical and mathematical framework to incorporate Van der Waals forces was established by

Derjaguin and Landau, and Verwey and Overbeek in the mid-20th century. Integrated with Van der Waals forces, the improved model was published in 1948 and renamed the DLVO theory after its authors[29-30] (**figure 7b**).

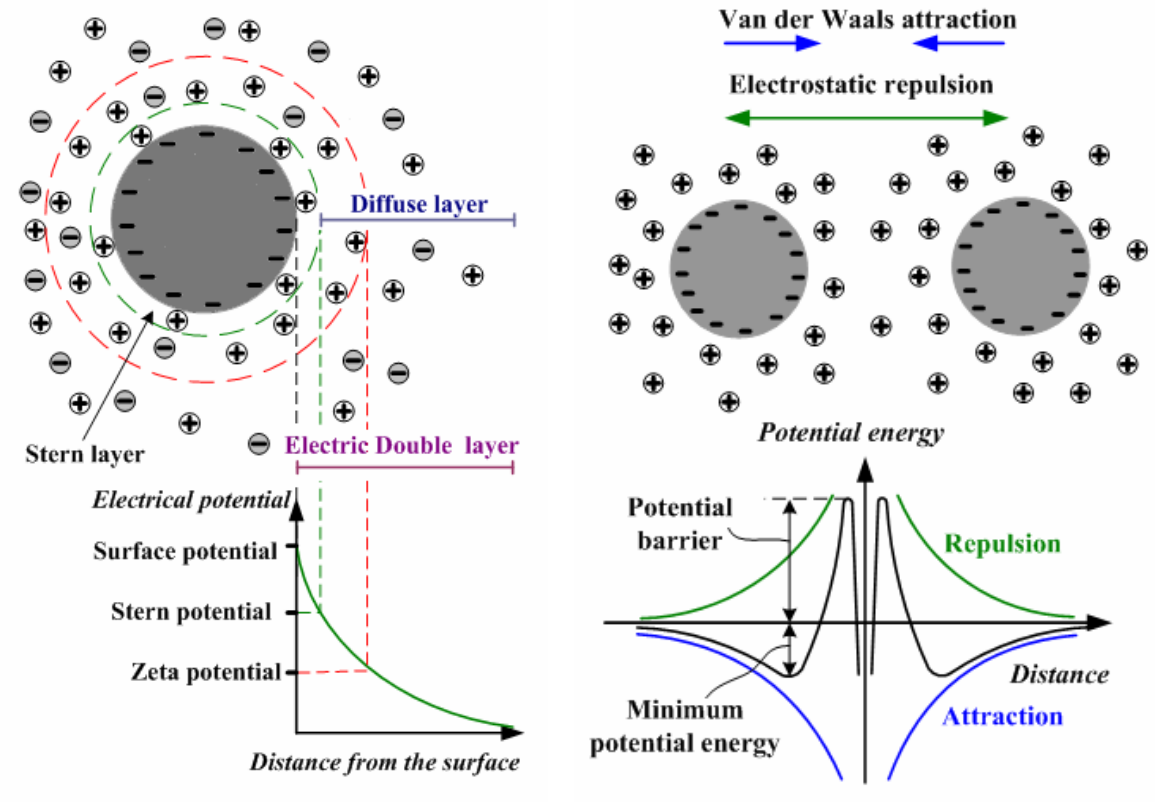

a b

Figure 7: The electric double layer and the DLVO theory. a) The electric double layer with modifications based on the findings of Brown and Boltzmann[31]. b) The DLVO theory is the result of combining Van der Waals attractive forces with the electric double layer model in a.

1.3. DLVO theory, limitations and the basis for organized water

DLVO theory is still used today and is primarily invoked in the electrochemical and colloidal sciences. Broadly speaking, the DLVO theory describes the attractive and repulsive energies between similarly charged bodies (microspheres, nanoparticles, single atoms) in aqueous solutions on the basis of three general principles:

1) *molecular interactions at the interface are governed by repulsive electrostatic and attractive Van der Waals forces*

2) *aqueous solutions contain significant concentrations of ions, which are modeled as spheres of charge*

3) *surfaces possess a constant charge density and display an electrical potential that decrease with distance from the interface*

Decades of experimental evidence confirm the validity of DLVO theory and are reviewed in detail within several textbooks on interfacial phenomena[30,32-33]. However, there remain a variety of exceptions that demonstrate limitations of the theory and furthermore, address questions concerning the aqueous media itself. Two such exceptions are solutions with salt concentrations[34-36] and water environments adjacent to protein, or hydrophilic polymers[12,37-38].

Under the DLVO framework, the salt content of a solution is a fundamental issue for experiments aimed at studying charged surfaces in aqueous media. It is a particular consideration when salt content is in the extremes, i.e. when solutions possess very high, or low salt concentrations. These situations are akin to physiological environments, or in the opposite case, solutions of deionized (ultrapurified) water.

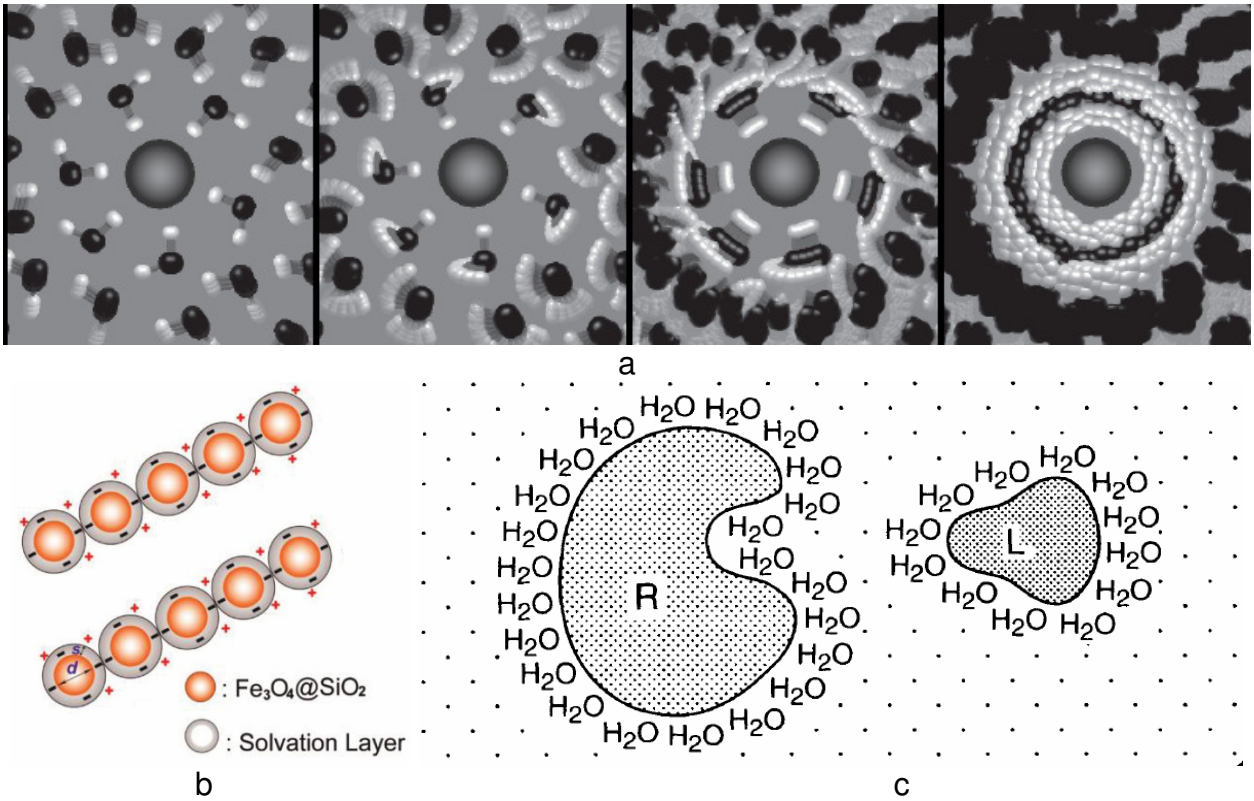

Figure 8: Salt, hydration forces and limitations of DLVO theory. a) An iodide ion (I^-) getting hydrated by water molecules[39]. As the network forms, significant stretching of the hydrogen bonds occurs between water molecules and results in unpredictable electrostatic behavior of the ion. b) A study demonstrating the DLVO theory's inability to account for hydration shells around ions in colloids of high ionic strength[40]. c) Notable paper by Israelachvili discussing the role of hydration in biological structures and how solvation shells are unaccounted for by DLVO theory[42].

In DLVO theory, ions (salts) modeled as point charges are assumed to be present in significant concentrations within a solution. While the idealization of charges as spherical point sources is reasonable, in recent years, experiments have demonstrated that ions are hydrated by clusters of water molecules (**figure 8a-b**) that vary in size depending on the ionic radii[39-40]. As a result, it is unclear how the collective ion-water network and their own interactions impact the surrounding solvent molecules (**figure 8b**), ion adsorption and/or the charge density of a surface. DLVO theory does not account for these so-called "hydration forces"[41-44] (**figure 8c**).

When salt is absent altogether in a solution, DLVO theory-based predictions diverge from the very scale on which the theory operates. Extremely low concentrations of ions (salts) in solution are typically found in ultrapurified water, which can be produced in a variety of ways. Regardless of the method, ultrapurified water can be generated in a controlled fashion and compared between a multitude of experimental setups. This is the very reason why it is employed in studies of water at charged surfaces.

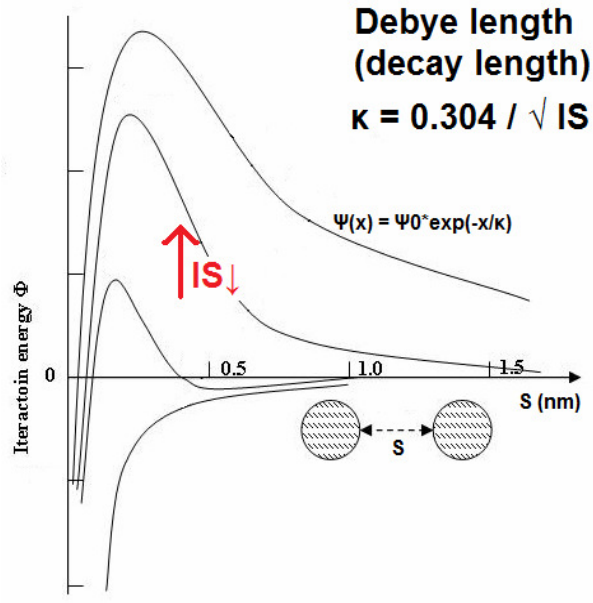

a

Component	Concentration (mol/kg)
H_2O	53.6
Cl^-	0.546
Na^+	0.469
Mg^{2+}	0.0528
SO_4^{2-}	0.0282
Ca^{2+}	0.0103
K^+	0.0102
C_T	0.00206
Br^-	0.000844
B_T	0.000416
Sr^{2+}	0.000091
F^-	0.000068

b

Table 3
Results on ultra-pure water samples

Sample	Na^+ (ng/l)
b	4
c	3
d	4
	K^+ (ng/l)
b	15
c	9
d	<5
	Ca^{2+} (ng/l)
b	<10
c	<10
d	<10
	NH_4^+ (ng/l)
b	105
c	65
d	30

c

Figure 9: DLVO theory and the ionic strength of aqueous solutions. a) The DLVO theory; as ionic strength goes down, the predicted curves for interaction energy climb higher and higher, denoting that electrostatic forces will dominate the experiment[45]. b-c) Salt concentration tables for sea water and ultrapurified water that were used to calculate the Debye length for DLVO theory predictions[46-49]. The lower the ionic strength, the more DLVO theory predictions depart from DLVO length scales.

With similarly charged surfaces, DLVO theory predicts that the electrostatic repulsive energy (Ψ_0) at the interface (x) of one surface decreases exponentially ($e^{-x/\kappa}$) in water at a decay length (κ) known as the Debye length. At standard temperature and pressure in water, the square of the Debye length is inversely proportional to the ionic strength of a solution[30] (**figure 9a**). Hence in the extreme case of sea water, the Debye length is

~0.4 nm because the high salt concentration[46] (**figure 9b**) increases solvent conductivity and attenuates (or "screens") electrostatic interactions. Consequently, Van der Waals attractive forces dominate between charged surfaces.

In contrast, deionized water produced by commercial purifiers[47] contains salt concentrations of less than 1 ppb (≤ 50 nM); it subsequently has a very low ionic strength. Therefore in deionized water, the calculated Debye length is 270 nm, about 1000 times greater than the Debye length in sea water.

In comparison to research-grade ultrapurified water, where salt concentrations measure in the picomolar range[48-49], the computed Debye length is 5-10 µm and surface interactions are governed solely by electrostatic forces. Interestingly, at a 10 µm Debye length, the electrostatic repulsive energy between charged surfaces theoretically decays and reaches zero at a separation distance of nearly 50 µm, a macroscopic distance over and above the predicted length scales within DLVO theory.

The preceding examples also underscore a quandary with the liquid environment itself. Within a solution, if ions (salts) are absent, or present in extremely low concentrations, and only solvent (water) molecules are available, then

1) *Is the double layer hypothesis still valid (or is it considerably reduced) since there are so few ions to adsorb onto a charged surface (**figure 10a-b**)?*

2) *If there are few ions, do water molecules (or other derivatives, i.e. H_3O^+, OH^-, etc.) fill in the corresponding roles of the absent ions (**figure 10c**)?*

3) *If only water molecules are available, do their dipole properties organize water to a greater number of layers than the equivalent single double layer of ions (**figure 10c**)?*

4) *If water layers are present, do hydration forces, such as hydrophilicity and water absorption, modulate the number of water layers formed (**figure 10d**)?*

5) *If there are a significant number of water layers formed at the interface, are molecular interactions purely electrostatic (as is also predicted by DLVO theory)?*

6) *If interactions are purely electrostatic, is the distance (for the previous example, 50 μm) along which the repulsive (or attractive) energy decays an indicator of how far organized water extends from a surface?*

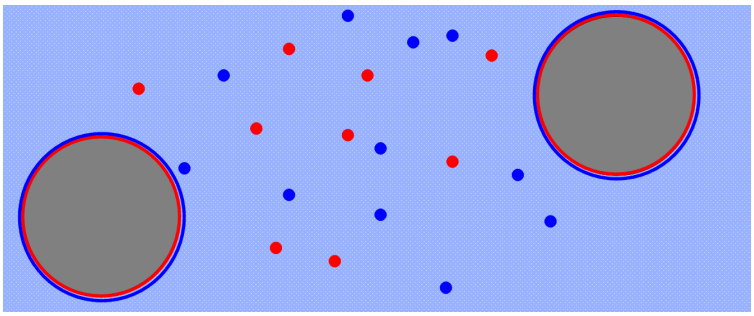

a. Charged surfaces order ions into double layers along their exterior.

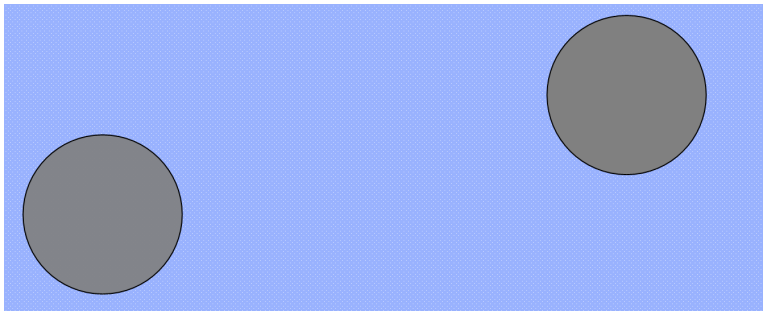

b. Is the double layer hypothesis valid without ions?

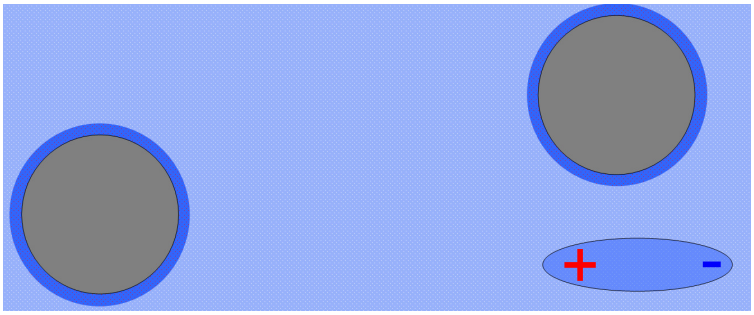

c. Do water molecules replace the role of ions along the surface? Do they organize in a significant number of water layers?

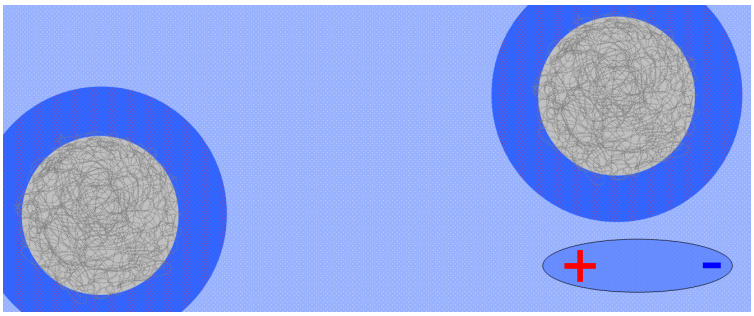

d. Does a hydrophilic surface which also absorbs water, like a gel, cause greater water ordering? Are the water layers extensive?

Figure 10: The basis for organized water at a charged surface.

1.4. The existence and extent of organized water

The concept of organized water, or water ordering, along a hydrophilic surface and its extent into bulk water has a long, controversial history. In traditional chemistry and colloidal science, organized water is hypothesized to consist a maximum of 1-2 layers (~0.5 nm) of adherent water molecules that are oriented in a direction depending on the charge of the adjacent surface. This prediction is based on complicated theoretical calculations involving the potential energy, enthalpy and entropy at the interface as well as the DLVO theory.

However, in recent decades, advanced spectroscopy and innovative instrumentation have directly measured the region next to a hydrophilic surface and provided invaluable data on the properties of the near surface water. These data have shown surface water is not only organized, but that it is quite extensive.

1.4.1. Spectroscopy evidence

Numerous spectroscopy techniques are employed to study near surface water. Primary methods include (in the order of their first applications to water) X-ray, Raman, nuclear magnetic resonance (NMR) and infrared (IR) spectroscopy. Improvements with IR spectroscopy in the late 1960s led to the advent of Fourier-transformed IR (FTIR) spectroscopy[50-51] and sum-frequency generation (SFG)[52-54] spectroscopy, which have been more widely utilized in recent investigations probing thin water films.

In FTIR and SFG experiments, water's IR absorption spectrum is a central feature. While IR absorption profiles for water have been initially mapped[55-56] and refined[57-58], the spectrum is complex to interpret due to the vibration modes of the water molecule, i.e. the molecule's ability to "(symmetrically/asymmetrically) stretch", "scissor", "wag", "twist" and "rock" (**figure 11**).

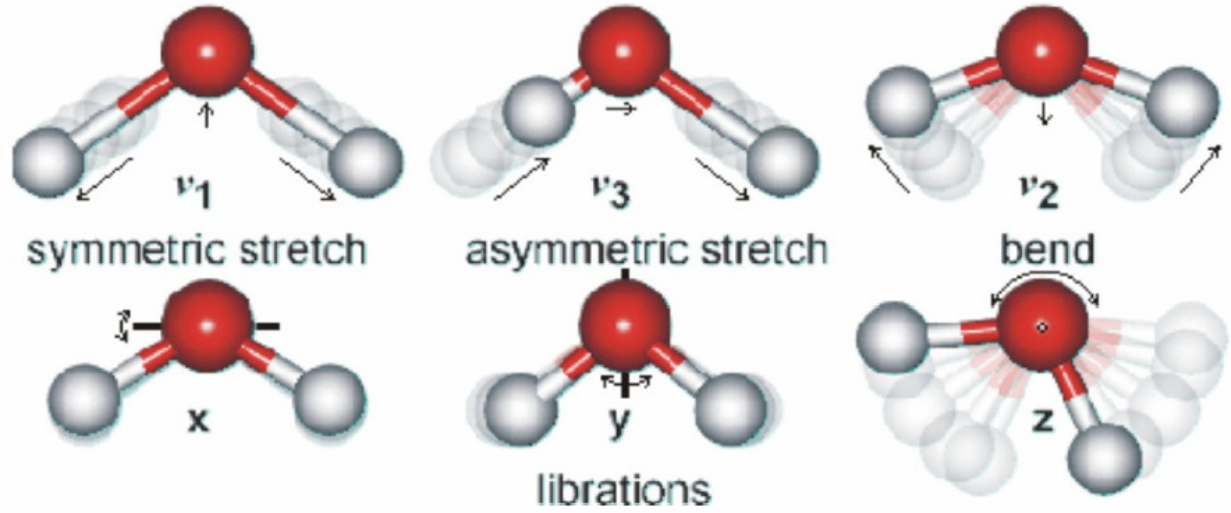

Figure 11: Water vibration modes[59].

Vibration modes are typically correlated to the IR spectrum through the location (wavenumber, wv) of spectral peaks[59]. For example, the single modes for scissoring and asymmetrical stretching correspond to IR peaks centered on wavenumbers 1643.5 and 3490 (λ = 6.08, 2.87 µm), respectively. Usually vibration mode combinations are what are commonly recorded in IR spectra, thus deconvolution of these data generate individual spectral peaks that reflect the individual vibrational modes. The linewidth of a single peak, or the distribution of peaks also contains information on the molecular structure and bonding properties of water at a given surface. Therefore in the FTIR spectroscopy of water, close attention is paid to the 3000-3800 wv (λ_{IR} = 2.6-3.3 µm) region of the IR spectrum because of its association with the O-H stretch in the water

molecule. This narrow range constitutes about 2% of the IR spectrum examined for the general spectroscopy of organic compounds.

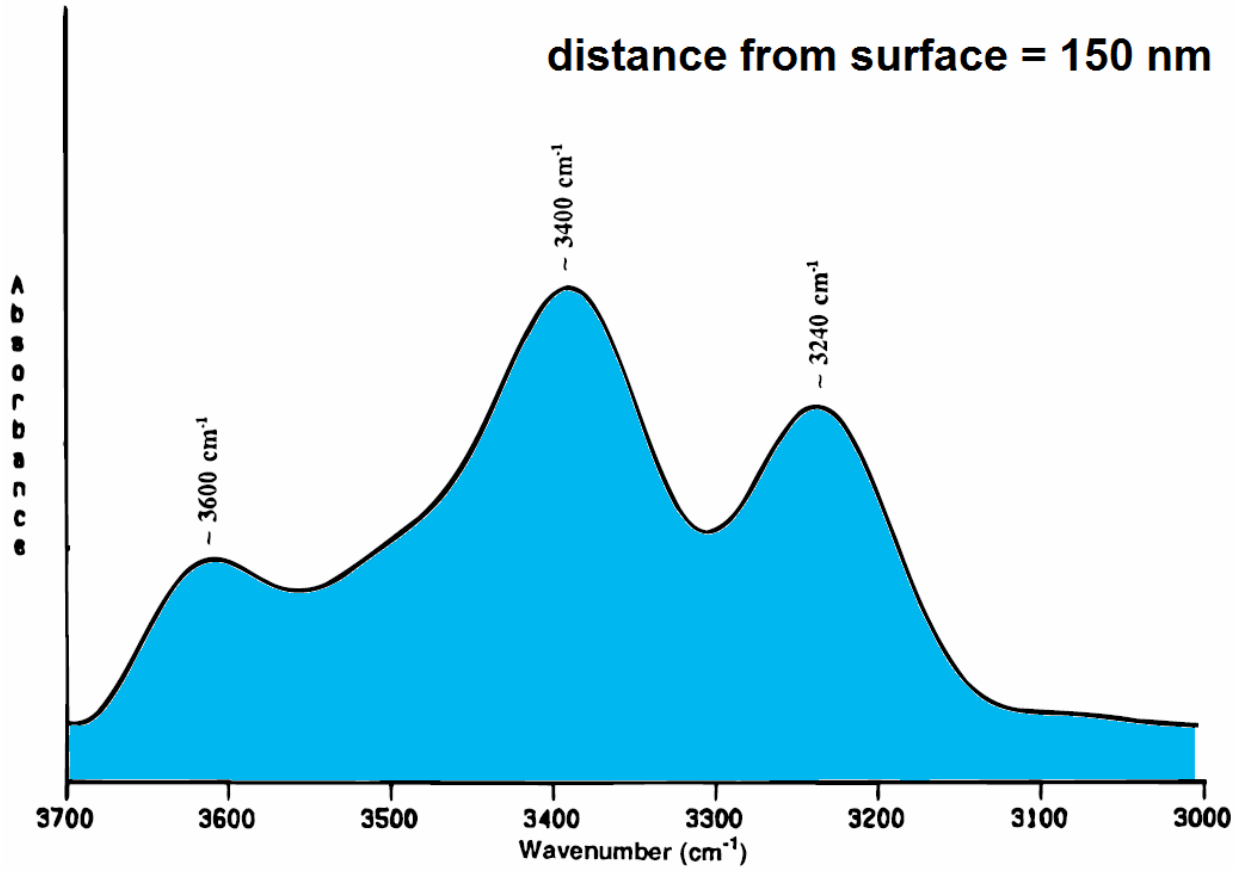

Figure 12: FTIR spectroscopy results of interfacial water at a hydrophilic surface[51]. The 3240 wv peak corresponds to ice-like water within the interfacial water.

Nevertheless, when FTIR spectroscopy was used on water next to a hydrophilic surface, spectral data depicted organized water that was "ice-like"[51]. Specifically, peaks in decreasing absorptivity were centered at 3400, 3240 and 3600 wv. These spectral peaks (**figure 12**) corresponded to the "incomplete tetrahedral coordination", the "complete tetrahedral coordination" and the "free O-H stretching" of water[51]. Free O-H stretching simply emphasized the existence of bulk water in the sample, whereas incomplete tetrahedral coordination (3400 wv) indicated a similar stretching, but within a bonded water configuration. The linewidth of the 3400 wv peak also denoted extensive

hydrogen bonding between the water molecules. Complete tetrahedral coordination, corresponding to the 3240 wv spectral peak, had a very significant ramification because it displayed the presence of "ice-like" water (ice has a sharp absorption peak at 3200 wv). In related work, hydrogen bonded ice-like water was also found independently using FTIR along a similar surface[50]. And in other SFG experiments examining water on quartz surfaces, a comparable spectra was acquired and ice-like water was verified at the interface[52-54]. Therefore on a first-principle level, water at the hydrophilic interface may be characterized as ordered and ice-like.

While FTIR and SFG spectroscopy have confirmed that water at the hydrophilic surface is organized in an ice-like fashion, the question addressing the extent of organized water has not totally been resolved. Even though spectroscopy has provided data on water near hydrophilic surfaces, the exact penetration depth of the individual spectroscopy method is a point of concern. Far from the hydrophilic surface, FTIR spectral features cannot be resolved due to the saturation and/or dispersion effects of the refractive index[60]. For regions 50-100 nm from the surface, spectral data is severely attenuated due to water's high absorptivity. As a consequence, the presence and extent of organized water could only be shown for a remote area beginning at 100 nm and up to 300 nm from the surface[50]. This limitation is similarly shared in some form, or another, by other kinds of spectroscopy, so as a solution, other mechanical techniques have been explored and developed to fill in the missing data of the water region at the very surface of a hydrophilic material.

1.4.2. Mechanical evidence

The most compelling evidence of the immediate extent of organized water from a hydrophilic surface comes from the research and mechanical measurements completed by American physicist Jacob Israelachvili in the 1980s (**figure 6i**, in blue). In a series of pivotal experiments, Israelachvili and others compressed thin films of liquid between two surfaces within what is now called the surface force apparatus and the interfacial force microscope[41,43-44,61-65] (**figure 13**).

Experiments measured forces from a confined water film as it was sandwiched between two hydrophilic surfaces. Confirmed as hydration forces[41-44], the measurements had a distinguishing feature in that the recorded force oscillated and harmonically increased as the distance between the surfaces approached zero (**figure 13b**). The measured spatial wavelength of these oscillations equaled the molecular diameter of water. Therefore both the spatial wavelength and increasing magnitude provided evidence that "force arose from surface-induced water structuring", which extended at least 5 nm (**figure 13b**) from the hydrophilic surface and was "sensitive to the chemical nature of the surfaces, and very sensitive to the presence of water"[42-44].

Opponents have argued that DLVO theory modifications could account for these forces, but Israelachvili asserted that "no theory, based on water, or solvent structure has been proposed that is predictive, theoretically sound and that accounts qualitatively for the observed effects"[42].

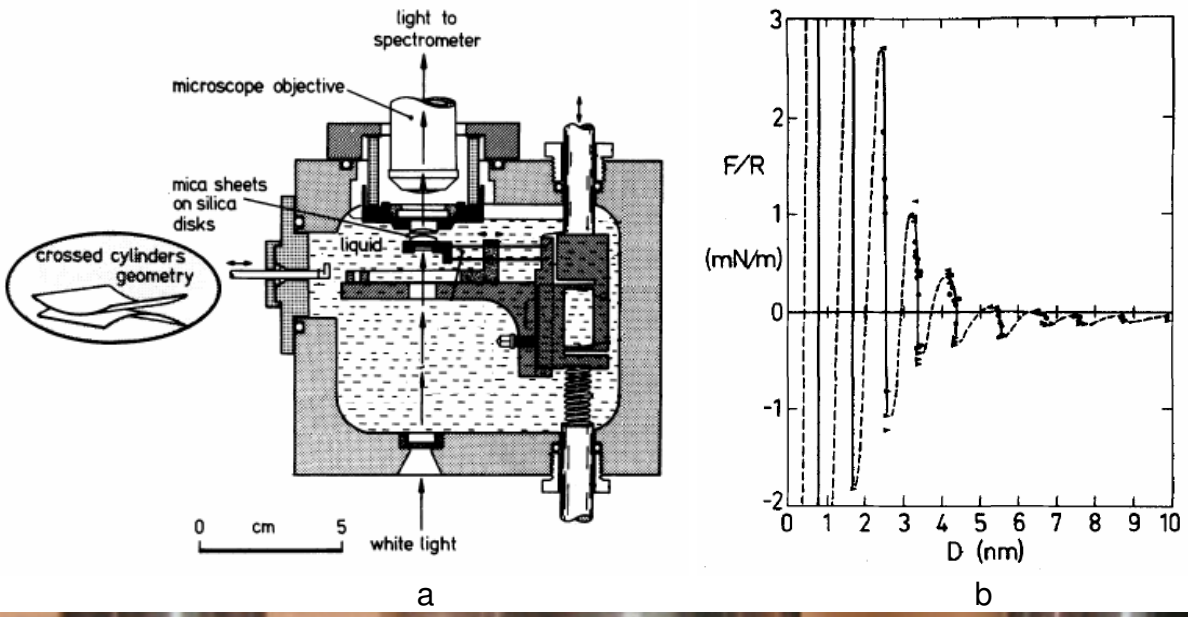

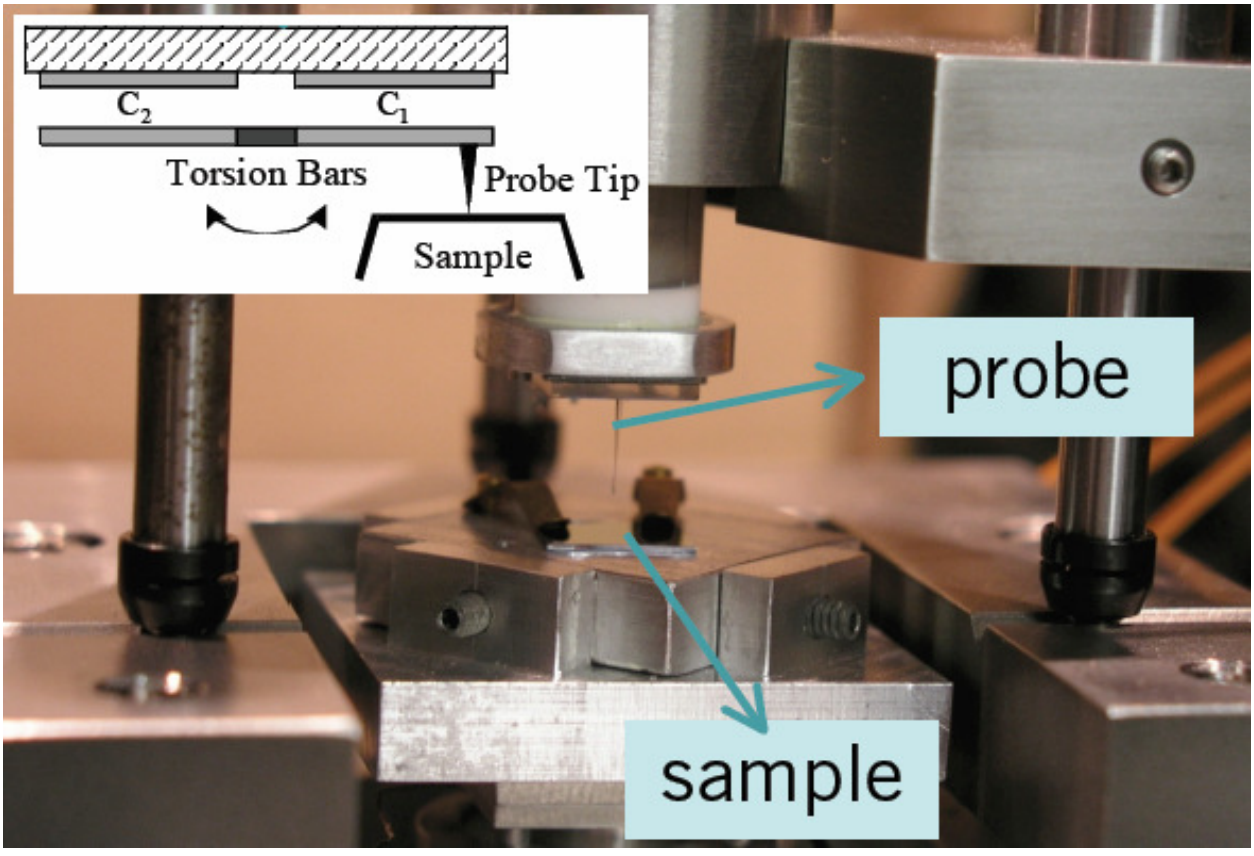

Figure 13: The surface force apparatus and the interfacial force microscope. a-b) The surface force apparatus compressed thin water films between two hydrophilic surfaces and recorded harmonically increasing oscillation forces starting at a separation distance of nearly 10 nm[41-44]. c) The interfacial force microscope compresses a drop of water between the probe tip and a hydrophilic surface[66]. The system allows the measurement of interfacial water viscosity at any surface of interest.

1.5. "Long-range water ordering"

Israelachvili's state-of-the-art research and the previous advanced spectroscopy methods were not without precedence as there is an equal, if not greater number of scientific investigations[6,12,37-38,68-72] emphasizing "long-range water ordering" dating back to a thorough review by Henniker in 1949[67]. Published a year following the publication of DLVO theory (**figure 6i**, in gray), Henniker's work systematically dissected and reviewed many types of data from experiments on water, including X-ray and electron diffraction experiments as well as direct measurements of the mechanical and electrical properties of near surface water (i.e., adhesion, density, viscosity, electrical potential, conductance and permittivity).

In his review, at least 10 types of experiments by independent groups provided data of long-range water ordering above and beyond the 1-2 nm limit, similar to Israelachvili's findings. At least three investigations measured the extent of organized water on the 100-200 nm scale, comparable to the FTIR/SFG spectroscopy results discussed earlier; one study concluded that water ordering occurred on the micron level.

Since Henniker and before Israelachvili, long-range water ordering has been confirmed on hydrophilic surfaces as diverse as mica[67,70], quartz[67-72], clay[67,70,72], sand[70,72] and glass[72] using a variety of spectroscopy methods and novel instrumentation. Several of these studies have also shown organized water extending into the bulk at least 50-100

nm (~200-500 water layers) with further long-range ordering depending on the size and geometry of the nucleating surface[71-72].

Considering the initial evidence, whether it be from the experiments reviewed by Henniker, the mechanical measurements of Israelachvili and others, or the aforementioned spectroscopy methods, the extent of organized water, or interfacial water, at a solid hydrophilic surface may be at least 100 times that of traditional estimates and hundreds of nanometers in thickness, or more. Highly dependent on the hydrophilicity, geometry and charge of a surface, the extensiveness of interfacial water may be even larger with polymers since they are, to a much greater degree, highly-charged, rough, hydrophilic and irregular in molecular structure.

1.6. Interfacial water and polymers

Interfacial water has an inherently complex relationship with charged polymeric surfaces. First, charges on polymer surfaces are directly accountable for the dynamic activity at the interface since they are not delocalized as they are in metals (**figure 14a**). The dense, porous network of polymers contributes to this activity so that the two properties cause significant inhomogeneity with respect to charge density. Inconsistent surface charge density in turn is responsible for the unpredictable electric fields and developed electrical potentials that vary greatly in magnitude and direction along the entire polymeric surface (**figure 14a-b**), which significantly influence the adjacent interfacial water.

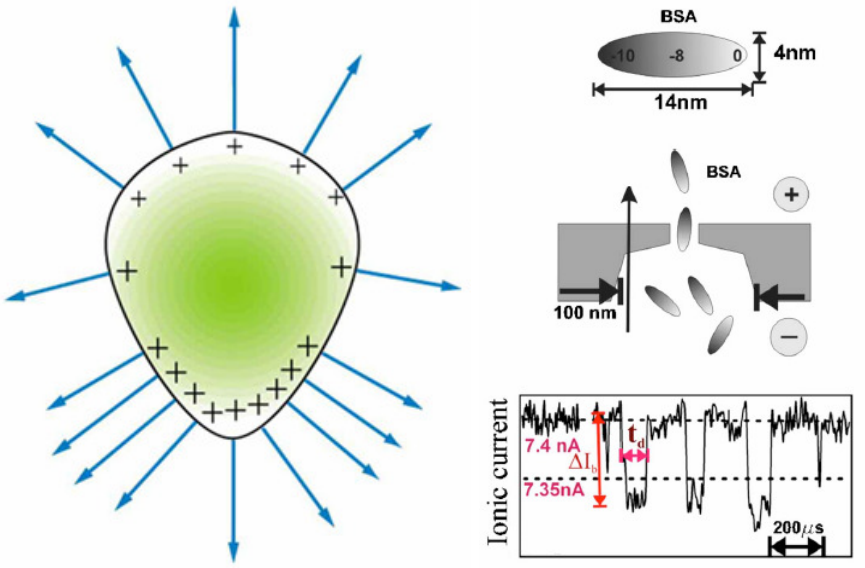

a b

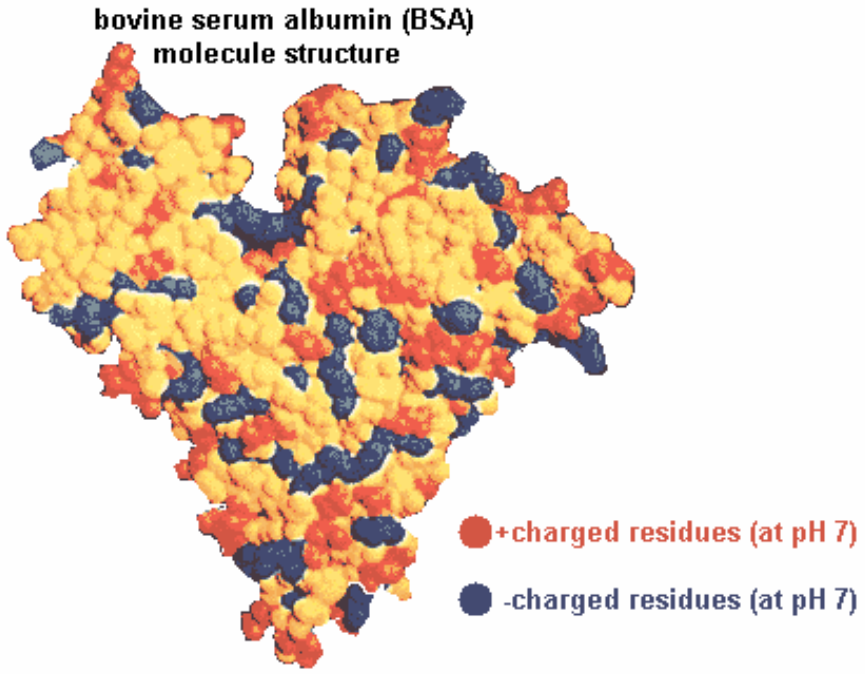

c

Figure 14: Charged, hydrophilic polymer surfaces. a) The non-spherical conductor as discussed earlier has an inhomogeneous surface charge distribution due to geometry[16]. The overall shape is similar to the protein bovine serum albumin in c. b) In characterization studies, however, the protein is assumed to be a symmetric ellipsoid with a disproportionate charge distribution[73]. c) In reality, while the shape is similar to what is shown in a, the charges are unevenly distributed everywhere, resulting in electric field development at the surface that is highly variable and unpredictable[74-75]. Surface potentials here are many orders greater than similar surface potentials in a.

Secondly, charge carriers are not limited to electrons. Similar to how a protein's charge is determined by pH and the associated isoelectric points of its constituent amino acid residues (**figure 14c**), polymer-water interfaces are subject to protonic and ionic currents that are dependent on the pH conditions of the surrounding water bath. As a consequence, corresponding current flow in the polymer and water is impacted by the multiplicity of carriers and their separate mobilities within the polymer network and water itself. The current flow therefore has an impact on the nature of the structure of interfacial water and thus is an important consideration.

Third, polymer surface roughness and irregular molecular geometry (**figure 14a, c**) are intimately involved with hydration forces (**figure 6i**, in blue). Aside from water adsorption, polymers hydrate, or absorb a significant proportion of water, a singular property not shared by other solid, hydrophilic materials like quartz. Hence water absorption is dependent on the polymer's molecular roughness and its surface area to volume ratio, both of which are commonly very high in dense networks (**figure 14c**). How hydration affects additional water ordering is complex, but most investigators believe it is an essential aspect of interfacial water.

Altogether, the multiple qualities seen in charged, hydrophilic polymers cannot be sufficiently accommodated for by current iterations of the DLVO theory. They may be in fact responsible for a higher degree of interfacial water ordering, which may extend into the bulk water on a much greater length scale than what is achieved by solid surfaces.

Ordering and extent of interfacial water with polymer surfaces may be best visualized in the macroscopic properties of hydrophilic polymers called hydrogels. In hydrogels, like agarose[38], or polyacrylamide-based gels[76], polymer networks can consist of as much as 99.999% water and (as a lower estimate) a 3000:1 water to polymer weight ratio[6,76-77] (**figure 15**). To understand this ratio, imagine taking a standard shoestring from a tennis shoe and cutting it down to a piece 2 cm long. If this piece retained all the properties of a single strand within the polymer network and was now the central axis of a cylinder of bound water, then the diameter of this water cylinder would be approximately 25 cm and remain suspended in space. Gels consisting of a high water content like **figure 15** can easily be picked up by hand without having the internal water content leak out.

Within charged, hydrophilic polymers, interfacial water is bound and resides within the interstitial spaces of the porous polymer network. For the previous gels, the average diameter of these pores ranges from 100-250 nm in a 5% agarose gel[78] to 15-40 nm in a similar, polyacrylamide-based gel[79-80]. Subsequently, one may ask if the entire water within the pore is organized, or if all the water is interfacial water (**figure 6i**, in green). For this question, the answer may be obtained within the context of biology, where intracellular environments are comprised of a substantial proportion of water and contain numerous charged, polymer networks that have intricate pore shapes and a distribution of sizes.

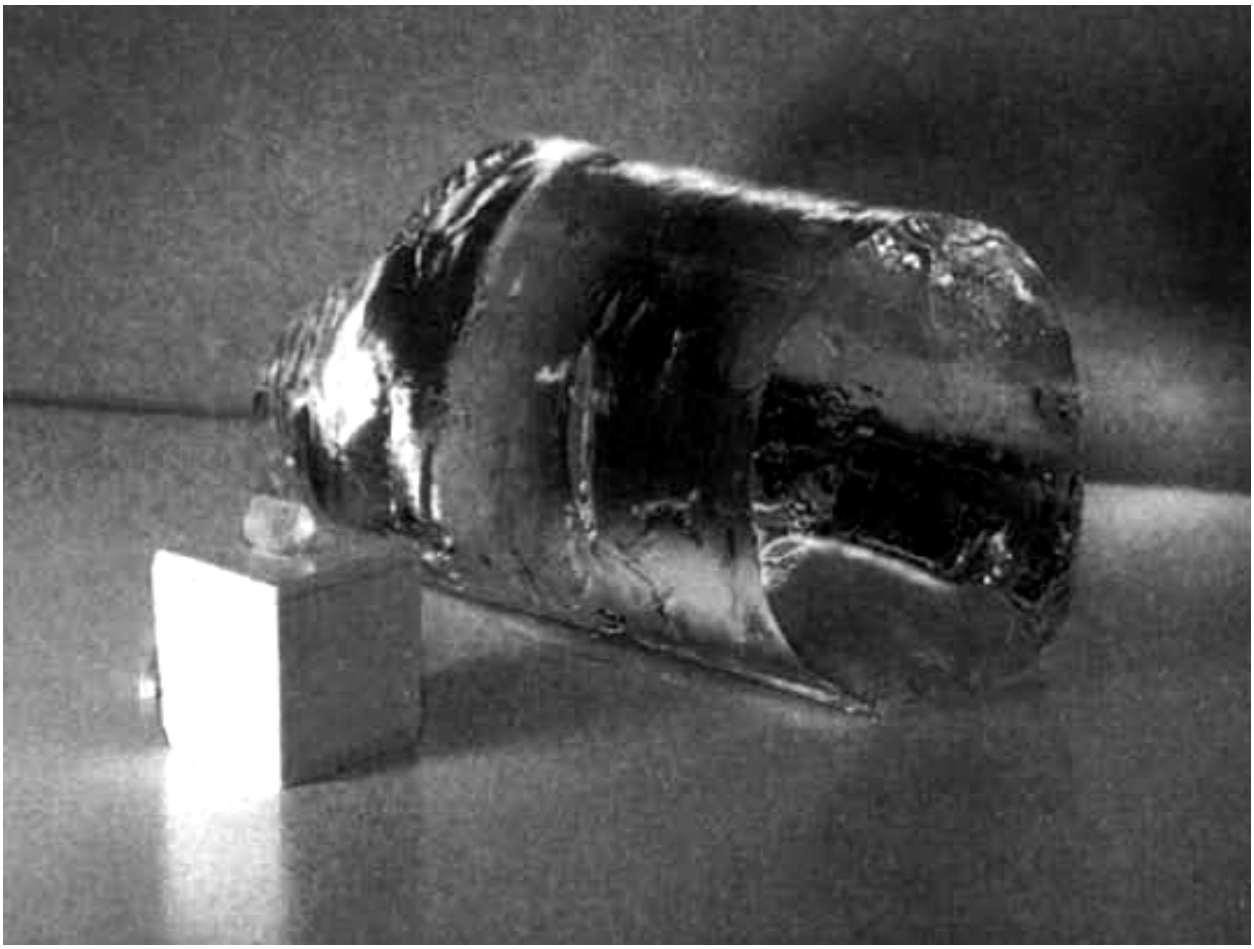

Figure 15: Water absorption properties of the highly-charged, poly(2-acrylamido-2-methylpropanesulfonic acid (PAMPS) hydrogel[76].

1.7. Biological surfaces, interfacial water and unstirred layers

Some of the earliest biological evidence for the existence and extent of interfacial water is based on an array of spectroscopy and microscopy experiments. In the 1949 Henniker review, water layers 78 Å thick were measured between the molecules of a crystalline virus using X-ray diffraction[67,81]. The authors of the study stated "the force of attraction holding them together must be acting over relatively large distances" and that ordered water layers "give the structure considerably rigidity".

1.7.1. Spectroscopy experiments

As spectroscopy improved and microscopy methods were refined, greater instrument accuracy helped determine water layer thicknesses around many kinds of polymeric biological structures. In a related study, free spaces 10-20 nm were measured between microtubules[12,82] through electron microscopy. Although image resolution ruled out any confounding structures between the rope-like polymeric microtubules, the water-filled cytosolic fluid within the in between region was the only possible source of the spacing. In comparison, water layer thicknesses of 20-100 nm were confirmed at the surface of agarose gels[38,42] and within the interphase regions of hydrated protein[37] when fluorescence microscopy and FTIR were used, respectively.

While these spectroscopy and imaging modalities were sufficient for studying interfacial water in biological samples, it was only until the development of NMR (**figure 6i**, in orange), specifically proton NMR (^{1}H NMR), that the existence and extent of this water in biological samples was better measured and quantified. Proton NMR has proven to be an invaluable tool towards understanding interfacial water in biological systems since water is two-thirds hydrogen and abundant in organic samples.

In a crucial 1965 study, NMR spectroscopy provided results on the existence of an "ordered phase of water" in skeletal muscle[83] (**figure 16**). Spectral data correlated to interfacial water were clearly visible as the spectral peaks exhibited a significantly broader distribution in comparison to the spectral peaks of bulk water[83]. Based upon

the acquired data, the authors concluded that the ordered (interfacial) water consisted as much as 10% of the total cell water content and that the proportional volume could be greater in other cell-types[83-86]. The interfacial water within these samples was additionally characterized by a "loss of considerable motional freedom relative to free water"[83]. In later studies, this "reduced mobility" finding would find support in the examinations of the mechanical properties of cytosolic water.

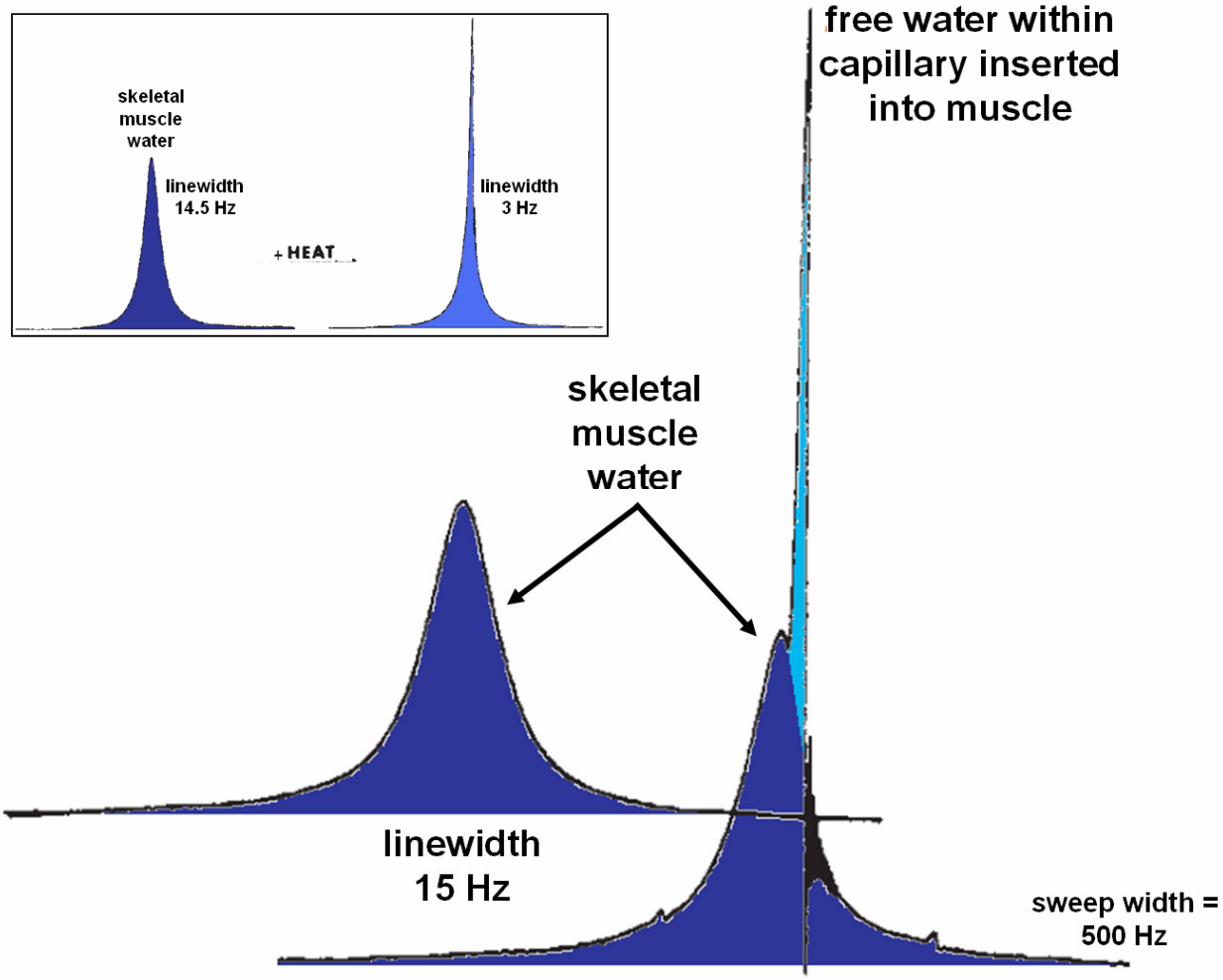

Figure 16: NMR of the water in skeletal muscle[83].

1.7.2. Mechanical experiments

On a macroscopic level, cell water, or cytosolic water, may be regarded as interfacial water since its mechanical properties are distinct from bulk. Discussed early on, water consists a significant proportion of the cell. With confined spaces between protein surfaces and protein crowding, one would expect that most of the cell water is interfacial water, even though earlier NMR data quantified this proportion as 10%[83].

In the last decade, several groups have developed instrumentation to measure interfacial water properties in cells. Specifically, microrheological characterization of the cytoplasm in microphages was achieved in one investigation by using "magnetic tweezers", which composed of magnetic microspheres and the application of static magnetic field pulses (**figure 17**). Recorded displacement data at several locations in the cell yielded viscosities at least 100,000 times that of bulk water[87]. With a slightly modified method and using epithelial cells, viscosities five times greater than these initial results (half a million times bulk water viscosity) were also similarly measured[88]. While it could be argued that viscosity magnitude was a result of dissolved solute and protein concentrations, other studies have ruled this possibility out.

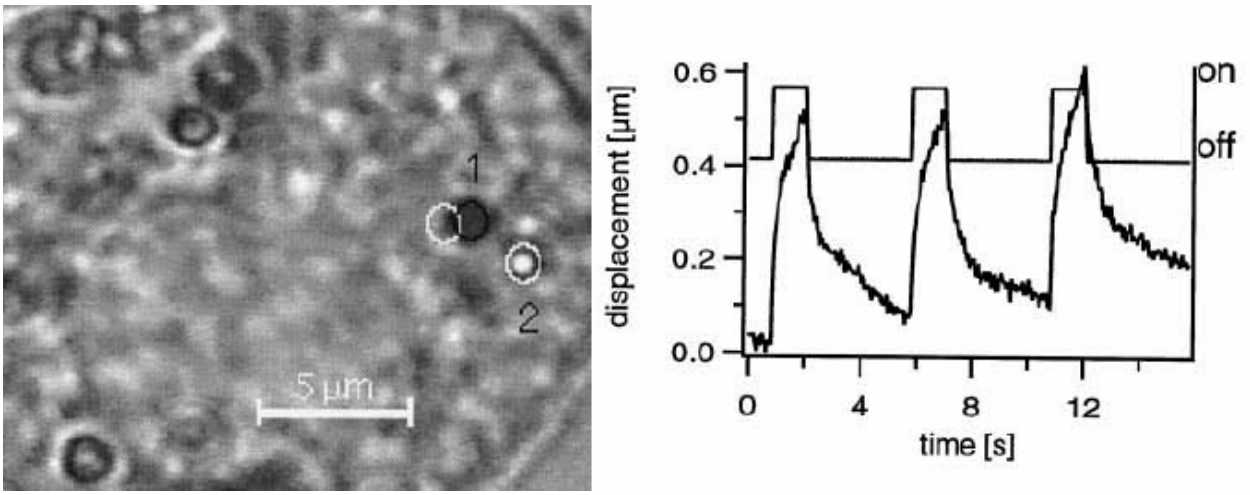

a b

Figure 17: Viscosity measurements of the cytosol[87].

In water films on clay[67] and in ultrathin pure water films on a hydrophilic substrate[61,63], viscosities have been measured to be on the order of at least 30,000 to > 1 million times that of bulk water viscosity (**figure 18**), respectively. In the latter study, interfacial water viscosity was positively correlated with the hydrophilicity of a substrate, i.e. the greater the hydrophilicity, the greater the viscosity of interfacial water. Along with the large viscosities found for interfacial water, other mechanical properties such as diffusion and permeability have also shown significant differences in comparison to bulk water. These properties are best illustrated within the well-established phenomenon known as unstirred layers.

1.8. Unstirred layers

Previous methods have provided important understanding on interfacial water at solid (hydrophilic) surfaces, hydrogels and biological polymers, but some of the most clearly

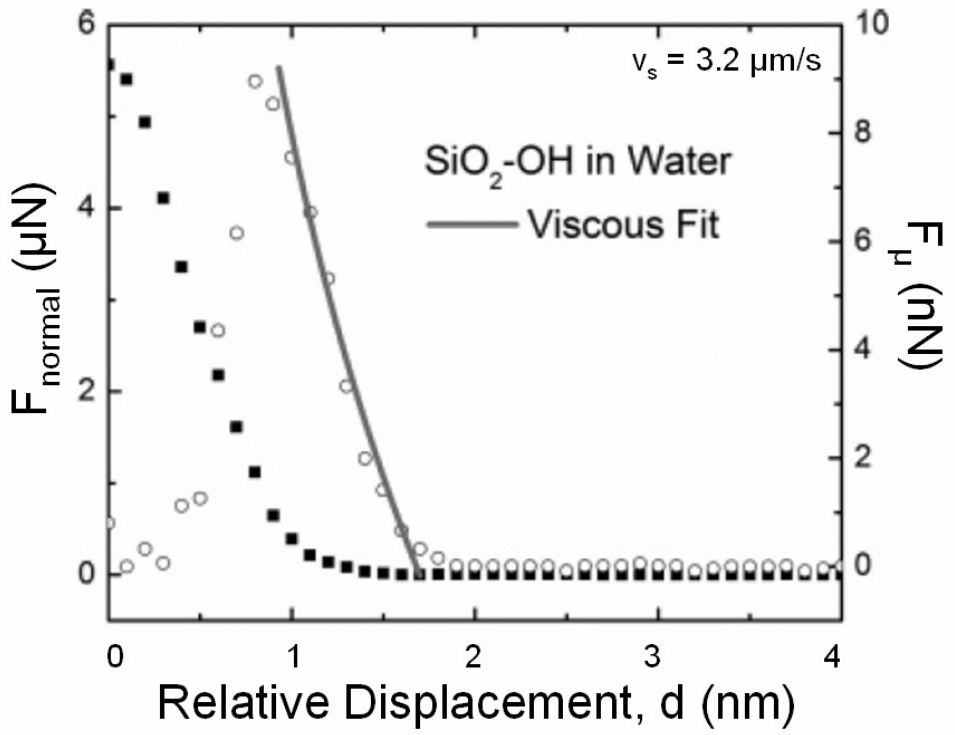

$$\eta_{\text{eff}} = \frac{\text{shear stress}}{\text{shear rate}} = \frac{(F_\mu / A_{\text{m}})}{(v_{\text{s}}/d)} = 1.6 \times 10^3 \text{ Pa s}$$

Figure 18: Viscosity of interfacial water at a hydrophilic surface[61].

defined examples of long-range interfacial water ordering can be found in zones known as unstirred layers[12,89-92]. Since the early 1900s and up until today (**figure 6i**, in green), light microscopy has been used to observe unstirred layers in aqueous solution as boundary layers adjacent to biological materials. Ranging from hundreds of microns to several millimeters in thickness and, in some investigations, lasting for hours[12,92,93] (**figure 19**), unstirred layers are regions of interfacial water where diffusion[94-96], solute permeability[97-98] and transport[99-102] are significantly reduced near, or at cell surfaces[12,92].

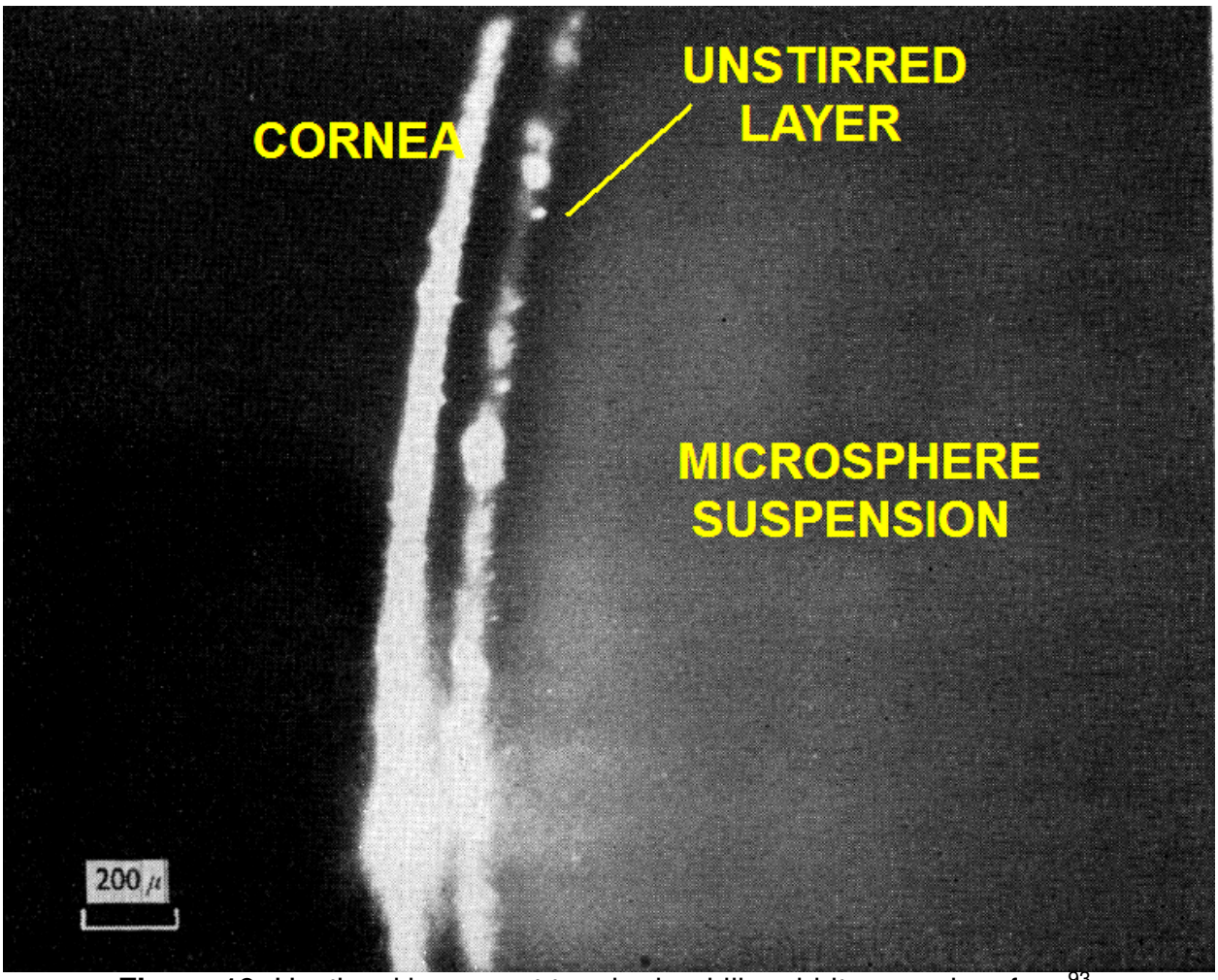

Figure 19: Unstirred layer next to a hydrophilic rabbit corneal surface[93].

Unstirred layers are also quite general and encompass a wide spectrum of biological surfaces such as aquatic plant cells[96], rabbit cornea[93], human red blood cells[97], rat intestine epithelial cells (in vitro and in vivo)[99-100], salamander gall bladder tissue[103] and more. In a simple demonstration to directly observe unstirred layers, one needs only a suspension of microspheres[93]. After depositing the suspension in a chamber with a sample material, microspheres are excluded from water layers immediately adjacent to the material's surface. The name "unstirred layer" stems from the fact that even with

vigorous stirring, these micropshere-free ("unstirrable") boundary layers persist at thicknesses as great as 10 µm[12,92] (~50,000 water layers). At a minimum, this distance is at least 100 times greater than the thickness of water layers measured by spectroscopic and mechanical techniques covered earlier (100-500 nm), and at least 10,000 times greater than traditional estimates (1-2 nm).

1.9. A brief summary

While unstirred layers have been well-characterized by many investigators, the mechanism behind the phenomenon is generally thought to be related to the extensive organization of water, despite the controversial nature of long-range water ordering (**figure 6i**). However to recap, past NMR[83] (**figure 6i**, in green, **16**), recent FTIR[51-52] (**figure 12**) and ongoing mechanical experiments[42-44,67] (**figure 6i**, in blue, **13**, **17-18**) have shown that "ice-like"[51-54] (**figure 12**) interfacial water can organize on the hundreds of nanometers[51,67,71] to hundreds of microns[92-93] scale (**figure 19**) for non-biological[67,71] (**figure 15**) and biological[82-83] (**figure 19**) hydrophilic surfaces. This is hundreds to thousands of times greater than traditional estimates for water (**figure 6-7**).

Organized (interfacial) water has also been shown to maintain order for several hours (in the case along a rabbit cornea[93], **figure 19**) to days (along a quartz surface[71]), hinting at mechanical properties which are unique from bulk (**figure 17-18**). For the most part, mechanical property differences have been characterized predominantly through viscosity, such as the key experiments conducted over the

last three decades by Drost-Hansen (along clay surfaces, 1969)[70] (**figure 6i**, in red), Sackmann (within the cytosol, 1999)[87-88] (**figure 17**) and Zhu (at a hydrophilic-coated substrate, 2007)[61-65] (**figure 18**).

However, recent work by Pollack and colleagues[6,92,104,106,108] have found exclusion zones next to various hydrophilic surfaces, exhibiting properties similar to what is seen with unstirred layers[92]. Initially discovered adjacent to many different types of hydrogels[104,106], exclusion zones are hundreds of microns in thickness and are an example of long-range water ordering, which is spectroscopically[107], electrically[105-106] and mechanically[108] distinct from bulk water. Therefore, it has been suggested that the exclusion zone is a possible driver for behind long-term water organization and a possible mechanism behind long-range water ordering.

Chapter 2: The Exclusion Zone

Unless otherwise specified, or referenced, all methods, experiments and data presented here on were conducted by the author of this dissertation.

2.1. The exclusion zone and microsphere-free regions

Exclusion zones, are exactly what their name implies: they are thick zones of water layers which exclude colloids, microparticles, low molecular weight dyes and even microorganisms[92,104-111]. To observe an exclusion zone, small microspheres, or microparticles were used as an indicator. Typically, carboxylate-functionalized polystyrene microspheres (Polysciences, Inc., Catalog #08226-15, d = 1 μm) were suspended (1:500 v/v) within ultrapurified water (Barnstead, Inc., D3750 NANOpure Diamond Water, ρ ≥ 18 MΩ*cm). The suspension was then washed into a chamber containing a hydrophilic surface, such as a standing Nafion tube (**figure 20b**). Imaging was done through a simple digital camera system (Scion Corporation, Inc., Color Digital Camera, Model #CFW-1312C) at moderate zoom (**figure 20c-e**) and acquisition rate (1-5 fps).

For microscopic observations and experimentation, an inverted microscope (Zeiss, Axiovert 135 TV) with low (2.5-5x) and high power objectives (10-40x) was used (**figure 22**). When chambers were alternatively observed through the microscope (**figure 21**), a

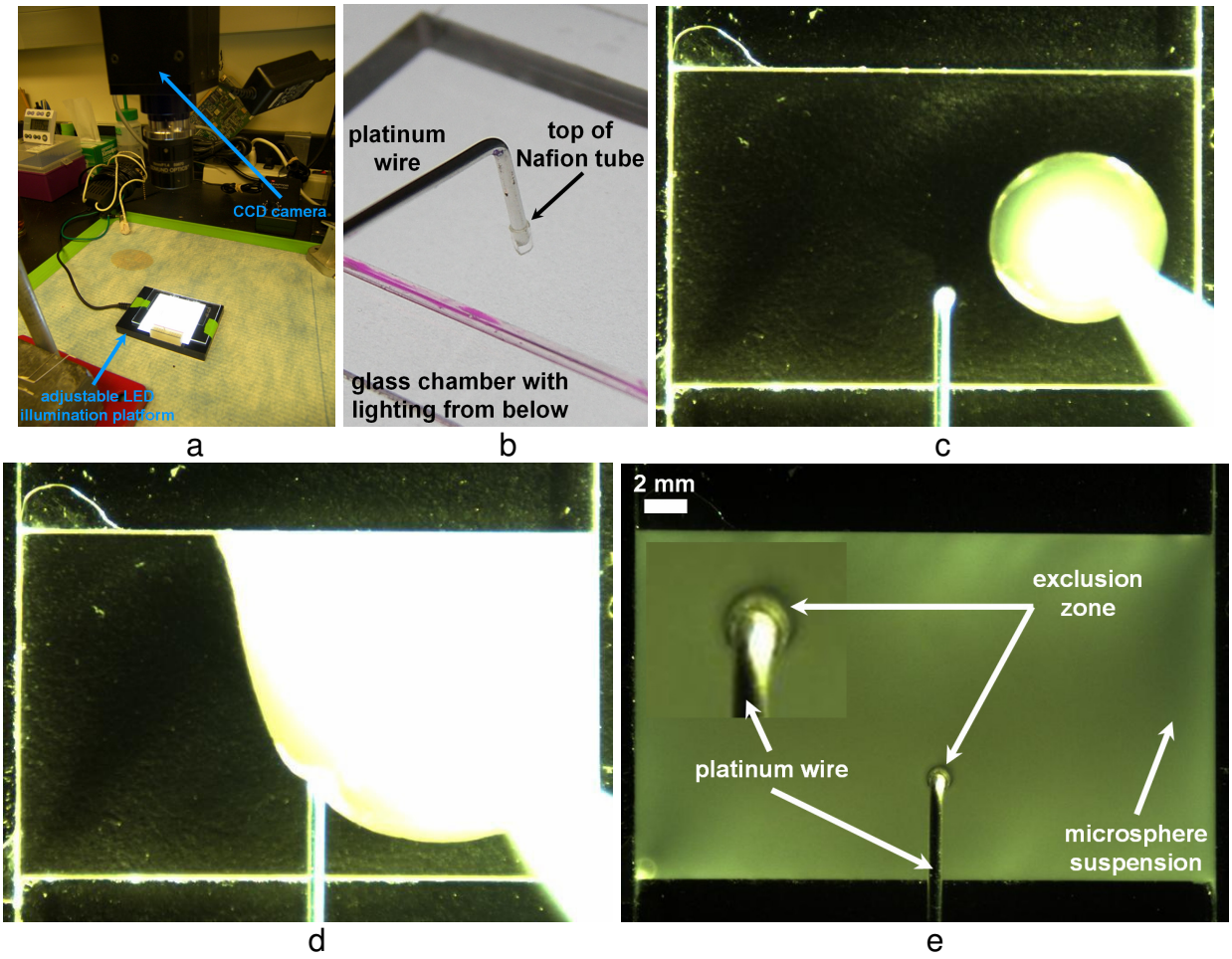

Figure 20: Visualization of the exclusion zone. a) Macroscopic setup consisting of a simple digital camera system that recorded observations of a glass chamber (25 x 15 x 1-2 mm) sitting on top of an illumination platform. b) Close-up perspective of the chamber. A Nafion tube was held upright in the center of the chamber with an "L"-bent platinum wire that acted as a mechanical scaffold. c-e) An 850 µL volume of a carboxylate microsphere suspension (1:100 v/v) was washed into the chamber. Within seconds, a clear, microsphere-free exclusion zone (black band, matching the original background of the chamber) formed at the surface of the Nafion tube.

clear band void of the microsphere suspension was visualized along the Nafion tube surface (**figure 21c-d**) after a microsphere suspension was washed into the chamber. Exclusion zones formed almost immediately and grew at a rate of 1-5 µm/s as previously quantified[104,108]. At 5-10 min, exclusion zone formation was stable and approximately 300 µm in thickness (**figure 21d**).

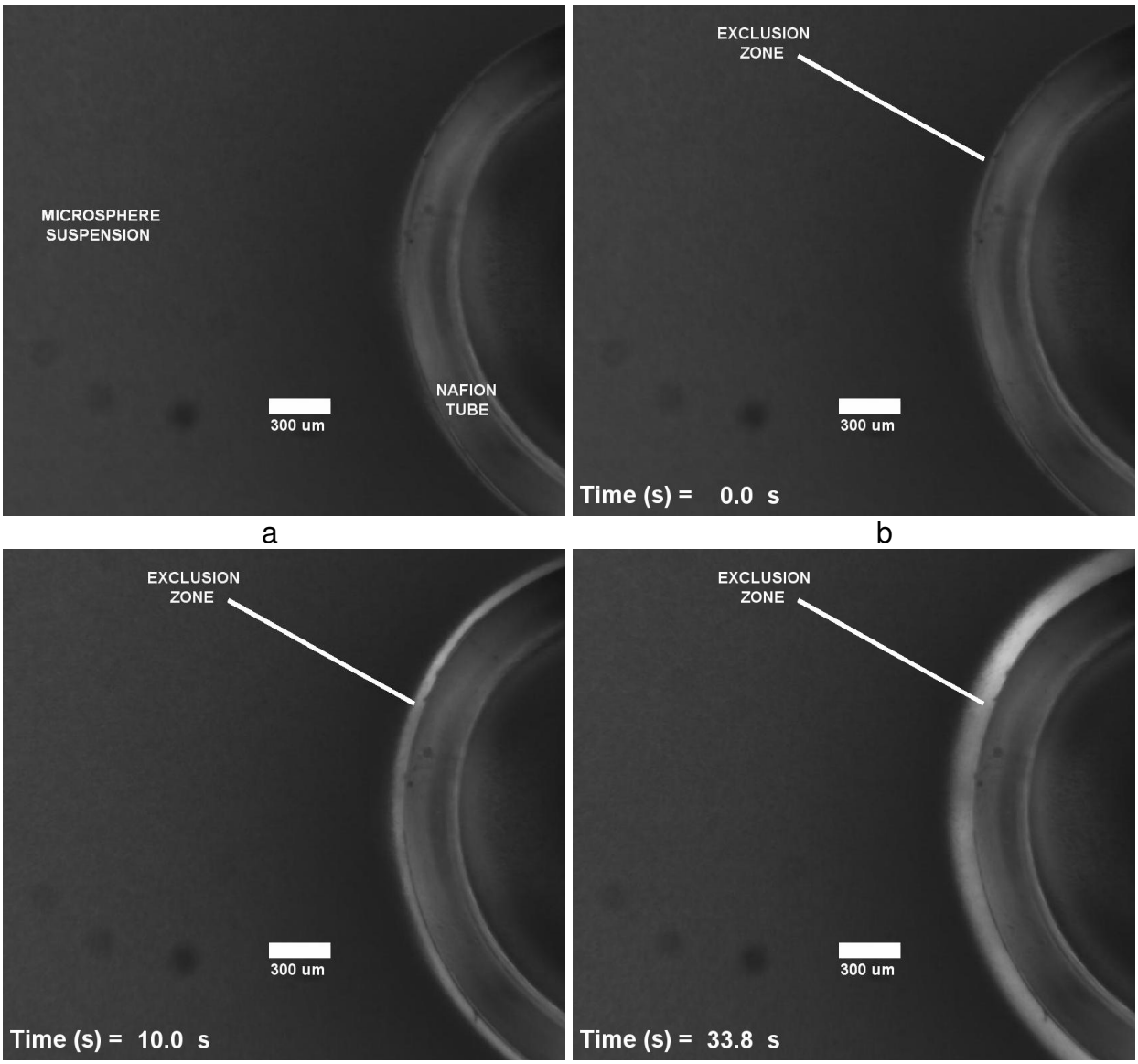

Figure 21: Exclusion zone formation along a Nafion tube through light microscopy. a-d) With a Nafion tube standing upright in the chamber, an exclusion zone (clear, white region free of the microsphere suspension) was seen alongside the surface of the tube through a 2.5x objective. The microsphere suspension is darker because a more concentrated (1:50 v/v) microsphere suspension was used.

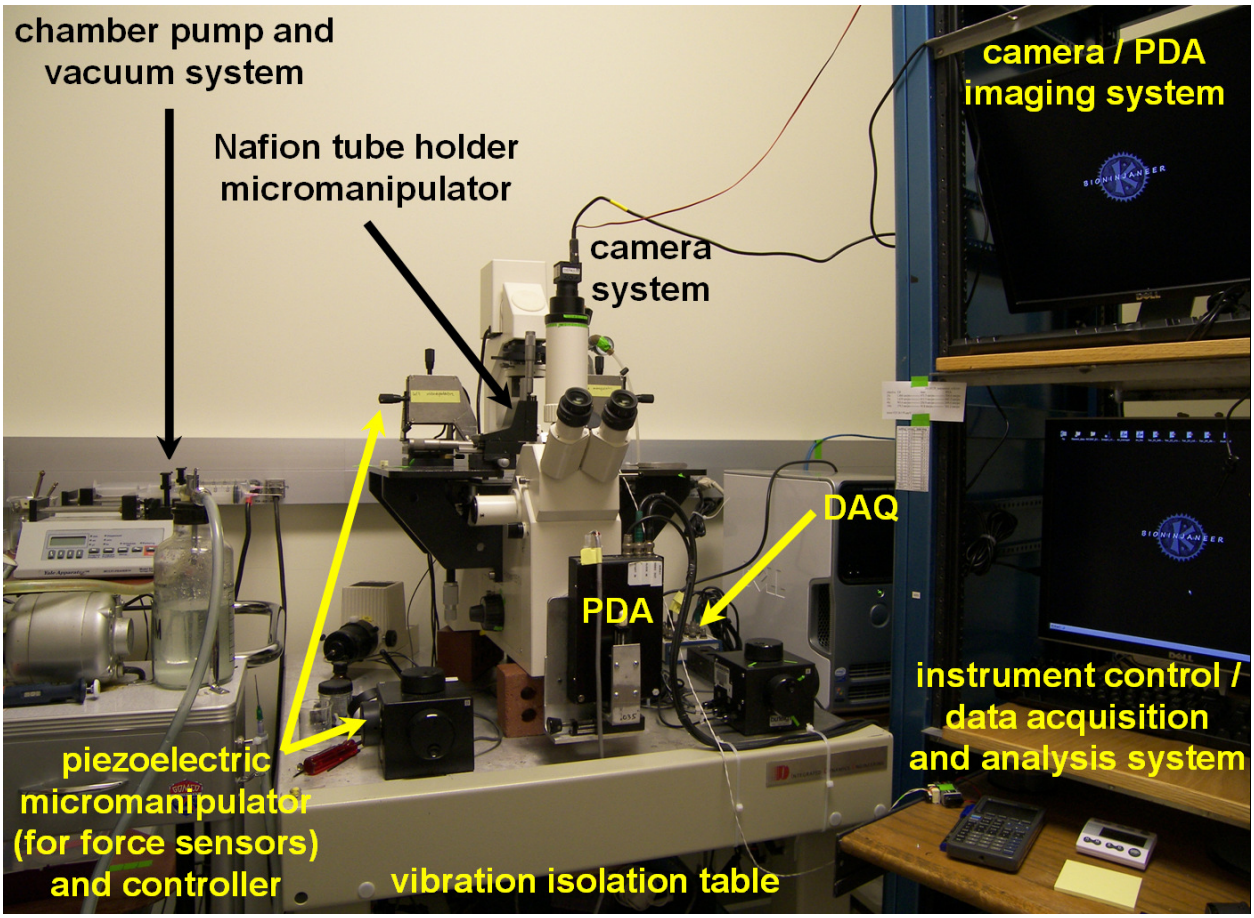

Figure 22: The general apparatus.

Positioning. Vertically-oriented Nafion tubes were positioned within glass chambers using a manual micromanipulator that has a 1-5 µm translation resolution (Newport, XYZ-Micropositioner, Model #9066-XYZ-R-V). For measurements involving ultrafine micropositioning and motorized translation, two piezoelectric motor-driven micromanipulators (Burleigh, Piezoelectric Micromanipulators, Model #TS-5000-150) along both sides of the chamber and affixed onto a modified stage were used. Motorized translations and translation velocities were limited to 150 µm excursion distances at 5, 10, 25 and 50 µm/s for various experiments and measurements.

Water bath. Pumps (Yale Apparatus, Syringe Pump System, Model #YA-12) and vacuums adjacent to the microscope fed solution lines of water, or microsphere suspensions into the chamber. These devices were employed in experiments when manual micropipetting was not used.

Optics. Chambers were observed with a digital camera (Edmund Optics, 1/2" CMOS Color USB Camera, Model #EO-3112C) and adjustable zoom lens. When coupled to low/high power objectives, and calibrated with diffraction gratings, the system recorded video at 3.2 µm/px to 42.9 nm/px (field of view = 6500 x 5000 µm to 90 x 65 µm). Camera frame rate was set at 1-5 fps for most studies and 1000-2000 fps for sensor characterizations. Alternatively, a custom-designed 1024 pixel photodiode array (PDA)

system was used to record intensity profiles of the workspace at 300 fps to determine sensor positions for force measurement experiments using previously developed nanolever force sensors[112].

Control, acquisition and analysis. Two networked computers combined with a data acquisition system (National Instruments, Inc., Model #PCI-6221) controlled motorized translations and acquired movies through LabVIEW 8.5 (National Instruments, Inc.) and ImageJ. All control programs and analyses were custom-written in LabVIEW 8.5, MATLAB10 (Mathworks, Inc.) and ImageJ.

2.2. Observations with universal pH-sensitive dye

Exclusion zones were also visualized within the macroscopic setup in **figure 20a-b** by using universal pH-sensitive dye (Science Lab, Universal Indicator Solution, Catalog #SLU1051)[110]. pH-sensitive dye is a solution consisted of a composite of pH indicators (**figure 23**) that denote low (alkaline) and high (acidic) pH through a color change of the solution (blue to green = highly to medium alkaline, yellow = neutral pH, orange to red = medium to highly acidic). When a Nafion tube was placed in the same chamber and a pH-dye solution (1:50 v/v) was washed in, dye was excluded from the tube surface at distances similar to when microsphere suspensions were used. In the bulk water beyond, the pH-dye changed to a red color, denoting a low pH, or high concentration of protons (**figure 24**). The initial dye-free region formed within seconds and the exclusion zone stabilized in thickness after 5-10 min, similar to observations using microspheres.

Bulk water regions further from the exclusion zone also continued to turn red in color. Additionally, the red colored region seemed to grow in thickness from 10-20 min and for even greater time periods when chambers of pH-dye and the Nafion tube were left overnight on the benchtop.

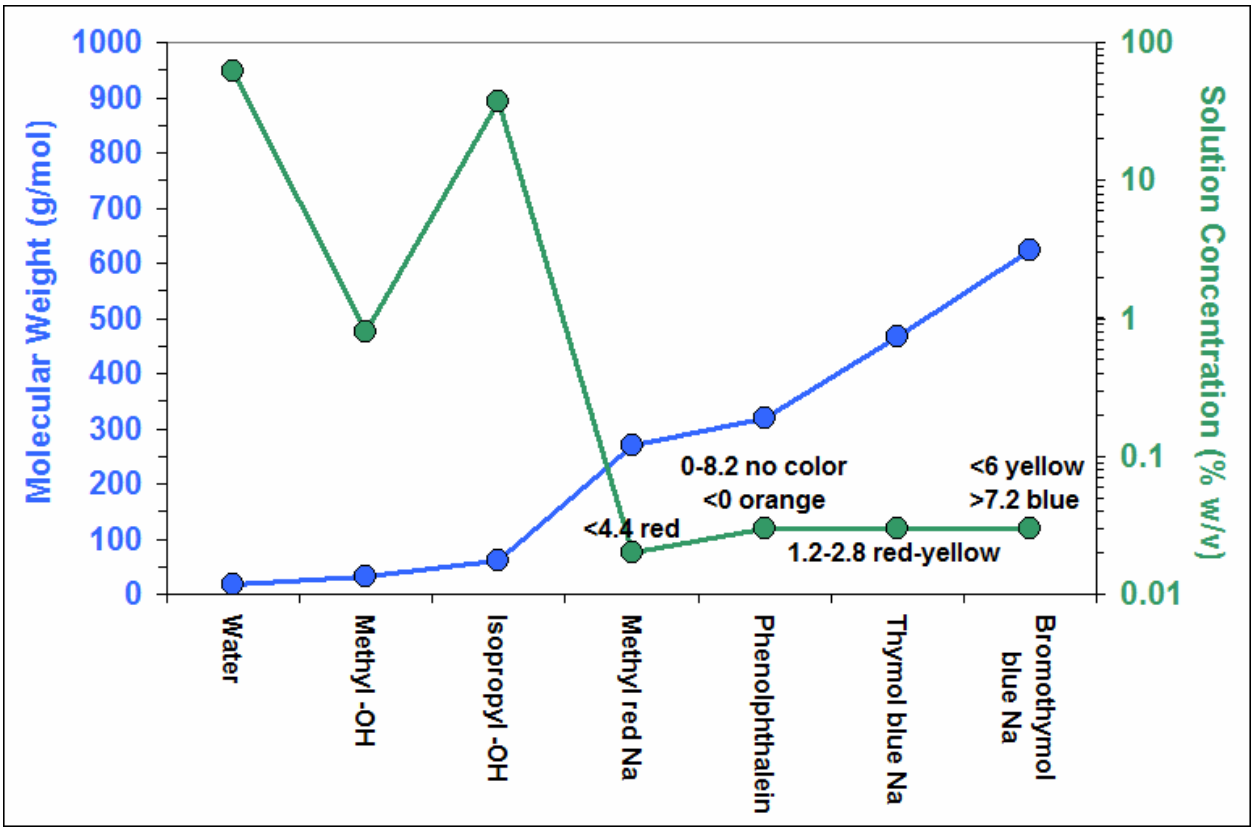

Figure 23: Indicators comprising the universal pH-sensitive dye. While pH-dye is nearly 95% water, the remaining 5% consists of alcohols (to stabilize the pH indicators) and high molecular weight indicator dyes that change color at various pH ranges. The black text for each indicator denotes the corresponding color change for a given pH range of a solution containing the particular indicator.

2.2.1. pH-dye calibration and quantification

Because color change is a subjective quality with respect to direct visual observation, steps were taken to characterize and quantify the pH-dye through a series of pH calibrations. Simply, low pH 0 (100 mM HCl) and high pH 14 (100 mM NaOH) solutions were made up and serially diluted in test tubes. The pH of each test tube was calculated based upon the dilution factor. A pH meter (Corning Pinnacle, pH Meter, Model #503) was then used to measure solution pH three times for each

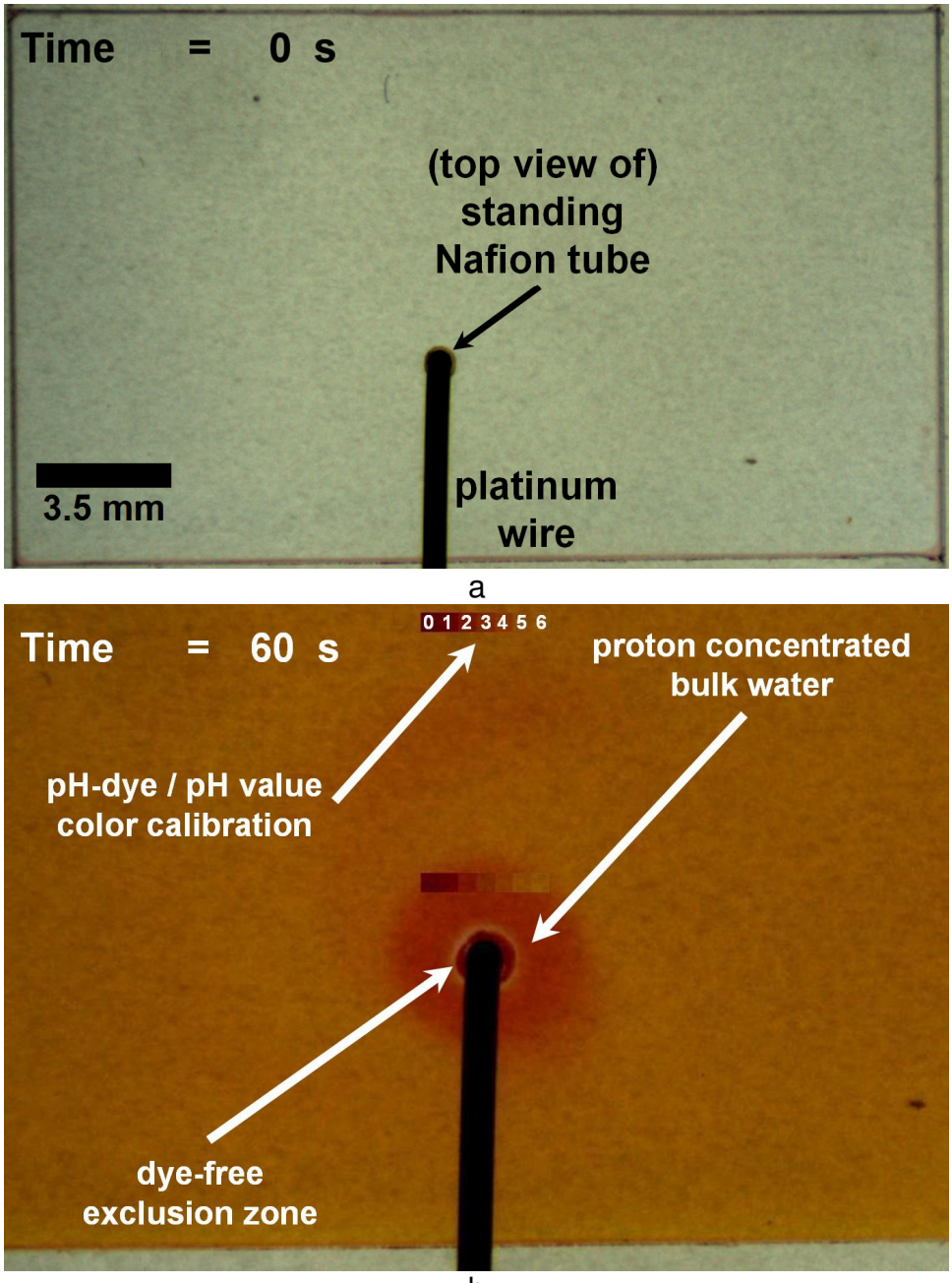

Figure 24: Dye-free exclusion zone formation at the Nafion tube surface. a) Top view of the setup shown in figure 20b. b) When a pH-dye solution was washed into a chamber containing a standing Nafion tube, dye was immediately excluded (~50-100 µm) from the Nafion surface and a high concentration of protons (denoted by the red color) was found within the bulk water solution beyond the exclusion zone. A calibration color bar of the pH-dye is also shown here to quantify the pH range.

corresponding tube after the meter was calibrated. Direct, averaged measurements did not vary by more than 5% from pH values calculated by the dilution factor.

Each pH solution was then washed into the experimental chamber. After setting the camera system to a high color contrast mode, images of corresponding chambers were taken (**figure 25a**). Because exclusion zone/pH-dye experiments corresponded to a pH range spanning neutral to low pH, chambers containing solutions of pH 0-7 were analyzed.

One particular difficulty of quantification resided within the inherent nature of color. While a primary color, such as red, has various shades and may be quantified in gray scale from 0-255, yellow, for example, is a mixture of primary colors (red and green) and is thus quantified by two separate gray scales. Therefore, how can one differentiate between red and yellow colors in a movie, and thus quantify the intensity of red color within a yellow colored background. The solution to the problem was found within the RGB spectral response curve of the camera system and its optical specifications. Details are elaborated upon in **figure 25**.

Simply, the green layer (gray scale) of a RGB movie recording was required to quantify red color distributions within the yellow colored pH-dye/water bath. After inverting the gray scale (0-255) of the green layer, intense red color was denoted by lighter gray shades (values $\rightarrow$ 255), while regions void of red color (and filled with yellow color) were denoted by darker gray shades (values $\rightarrow$ 0).

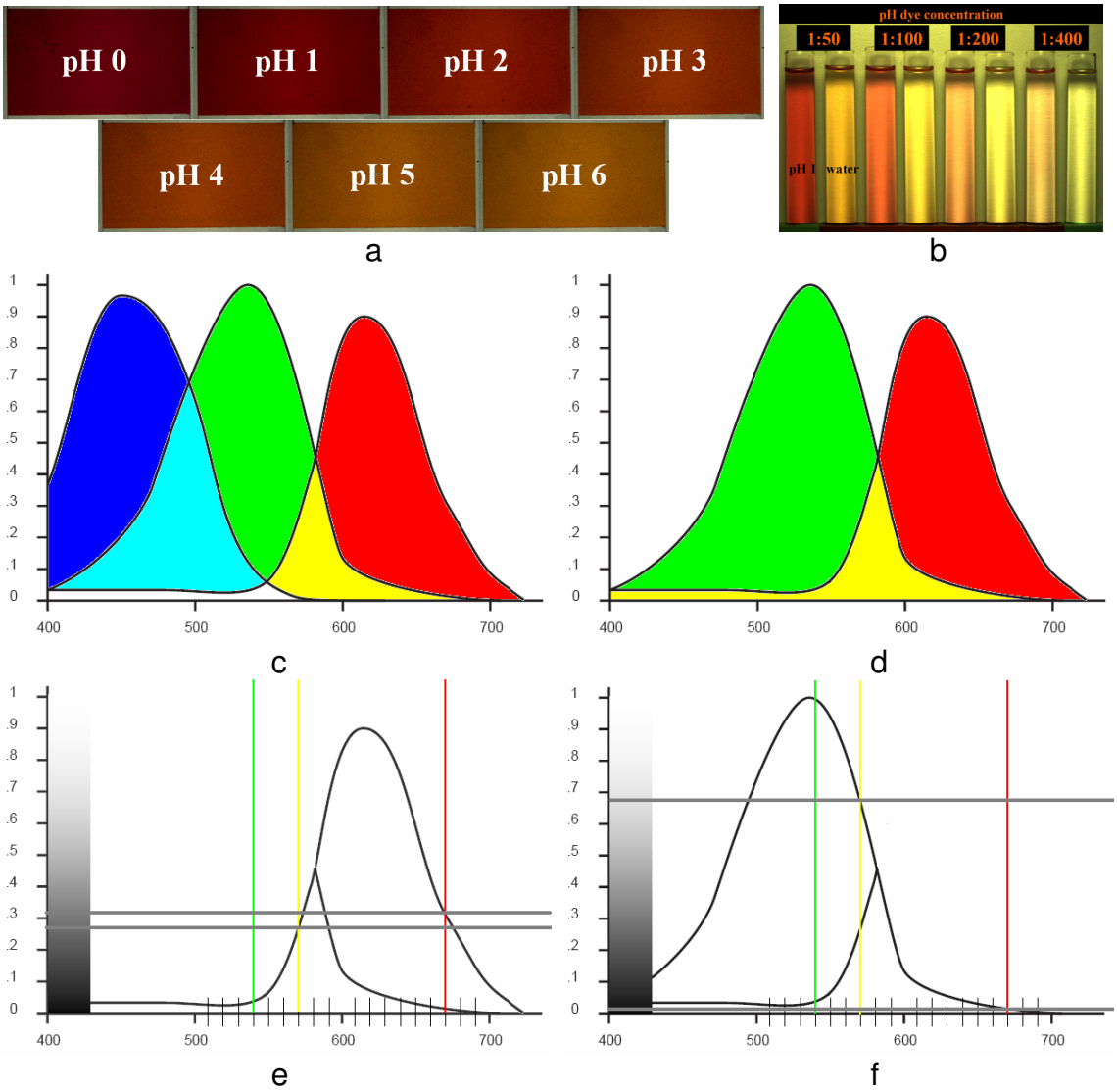

Figure 25: pH-dye calibration and quantification. a) Titrations of HCl concentrations and corresponding solution color change using pH-dye. b) Decreasing concentrations (in v/v) of pH-dye with a pair of solutions: HCl (of pH 1) and water (dispensed from the purification system). c) RGB spectral response of the camera system. d) Green and red spectral responses of the camera system. e) Red spectral response of the camera system with a gray scale color bar. Green, yellow and red lines denote the wavelengths of light for pure (green, yellow and red) colors as determined by eye. Gray line pairs denote the intersection of the pure yellow and red color wavelengths with the red spectral response curve of the camera. Since the yellow itself contains some red, the difference (contrast) between pure yellow and red colors (denoted by the vertical distance between the gray line pairs) is less than the distance between the gray line pairs in f. f) Green spectral response of the camera system with a gray scale color bar. The difference (contrast) between pure yellow and red colors is greatest. Therefore, when observing a pH-dye experiment in gray scale, differentiation between yellow (gray scale → white, or 255) and red (gray scale → black, or 0) colors was best achieved when the green layer of a RGB movie recording was used.

This relationship allowed the correlation of gray scale intensity (reflecting red color) to the pH value of a given proton concentration (**figure 25a**). Hence, 25 units of gray scale intensity change corresponded to a single pH unit; because pH is a logarithm of proton (charge) concentration, the number of charges present at a given location with a gray scale intensity was characterized by an exponential function, such that

$$\text{region charge (C)} = e^{(\text{average gray scale intensity}-147)\,/\,10}$$

Therefore, when the analysis was applied to standard pH-dye experiments (1:50 v/v), bulk water regions beyond the exclusion zone corresponded to a pH value ~2.3.

However, another consideration was the overall concentration of pH-dye. Red color had an overall less intensity in the bulk water region when pH-dye at 1:400 v/v instead of 1:50 v/v was used. Subsequently, several concentrations (1:100, 1:200 and 1:400 v/v) of pH-dye (**figure 25b**) were employed for solutions of HCl (fixed at pH 1.0) and ultrapure water (directly dispensed from the purification system). Imaging the solution pairs for each pH-dye concentration allowed the determination of the lowest concentration of pH-dye that could produce a perceptible red color by the camera. Consequently, the results of these experiments combined with the previous calibration yielded a first order, lower bound estimate for the number of protons in the bulk water region. As a result, a 1-2 mm thick red colored region around the exclusion zone corresponded to at least 8×10^{13} (80 trillion) protons.

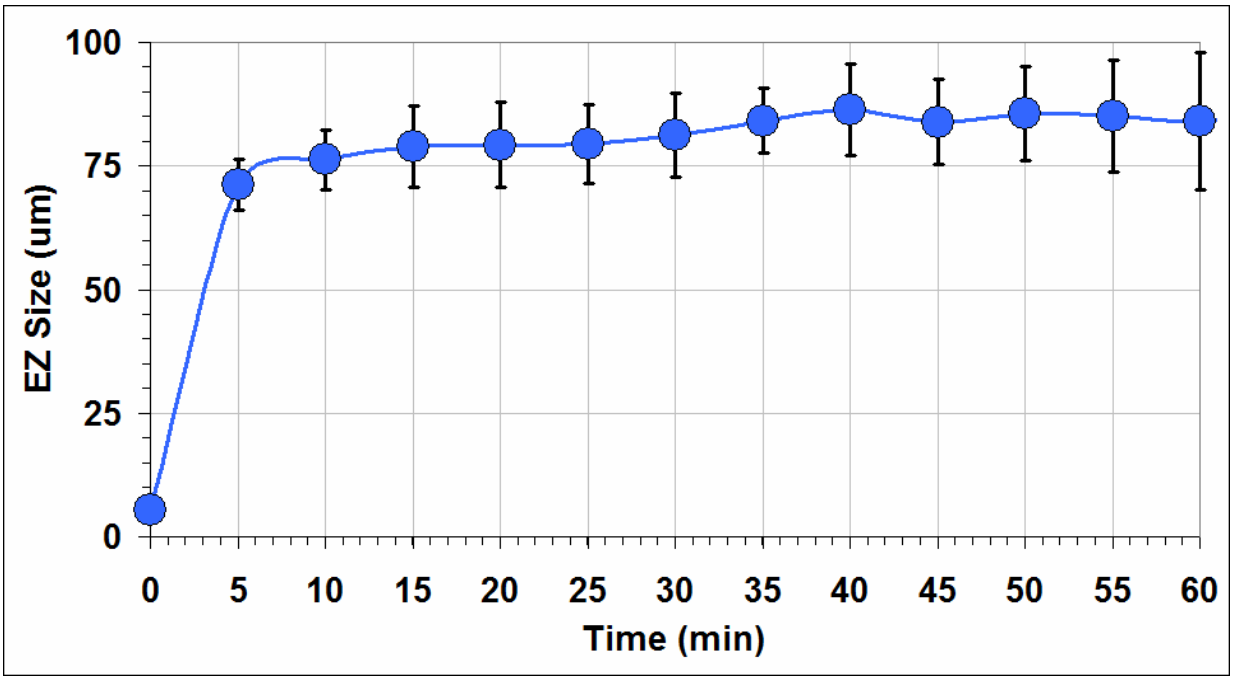

Figure 26: Measurement of the exclusion zone's thickness over time. Using a 1 µm carboxylate microsphere suspension (1:500 v/v), five measurements around a Nafion tube (n = 3 tubes) were averaged every 5 min for a period of 60 min.

2.3. Exclusion zone thickness and projections

While pH-dye experiments are good indicators for measuring the exclusion zone thickness, microsphere suspensions were more readily utilized due to their homogeneous milky-white color. By changing the background color of the platform the experimental chamber sat on to a high contrast (black) color, exclusion zone thickness measurements were easily made. Microsphere-free regions were therefore see-through (and hence black), while bulk solutions containing microspheres were white (**figure 20e**). Using a microsphere suspension, five measurements were made around a standing Nafion tube for an experiment spanning 60 min; exclusion zone thickness and stability were thus quantified (**figure 26**) for several experimental runs and averaged.

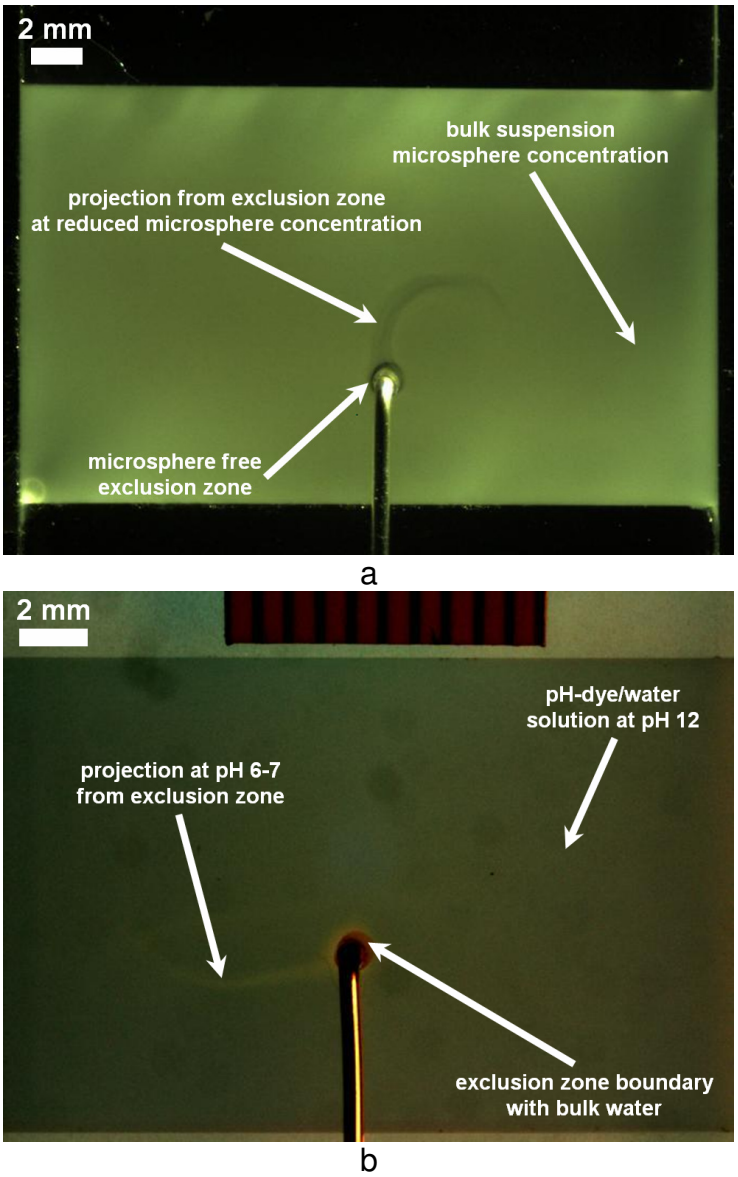

Figure 27: Projections of the exclusion zone into the bulk solution. a) After an initial exclusion zone formation, in several experiments, a projection of the exclusion zone extended at least 2 mm into the bulk microsphere suspension and continued to grow for nearly 30 min, regardless if the microsphere suspension was consisted of positively charged (amino, amidine), or negatively charged (carboxylate) microspheres. b) A similar experiment using pH-dye. Although projections of the exclusion zone using pH-dye were shown previously[110], zone projections within the current setup were difficult to visualize due to the contrast between the red and yellow colors (discussed in an earlier section on pH-dye calibration). Therefore a high pH 12 (NaOH) solution with added pH-dye was washed into the chamber containing a Nafion tube. Since the exclusion zone has a corresponding concentration of protons in the bulk water beyond, it was expected that proton/hydronium and hydroxide neutralization would produce a neutral pH (yellow color) at the very boundary of the exclusion zone. This was confirmed and as a result, yellow trails were seen extending into the bulk pH-dye solution, allowing visualization of projections, similar to those observed when using microsphere suspensions in a.

Results demonstrated that an exclusion zone 80 µm thick persisted for as long as 1 hr. While many measurements of exclusion zones within the first 5-10 min may vary between 100-300 µm, an 80 µm thick measurement represents an average thickness around the entire Nafion tube. This is an important consideration since exclusion zone formation and growth is not always homogeneous. For example, low concentration regions of microspheres, or pH-dye, were found in projections stemming from the exclusion zone. These projections were observed over vast distances and in some cases, extended nearly 5 mm into the bulk microsphere suspension, or pH-dye solution (**figure 27**). These distances are 50-60 times greater than the average thickness of exclusion zones observed around Nafion tubes. In some experiments, projections broke-off entirely from the exclusion zone at the Nafion surface and floated free within the bulk solution, void of microspheres, or pH-dye. One possible explanation for this phenomenon is based on charge separation and the long-range ordering of water within the exclusion zone and is discussed further in a later section.

While Nafion tubes and microsphere suspensions are predominantly used to visualize the exclusion zone phenomenon, many other hydrophilic surfaces have displayed exclusion zones tens to hundreds of microns in thickness. Originally observed with microsphere suspensions next to a polyvinyl alcohol (PVA) hydrogel (**figure 28a**), exclusion zones have been found with other hydrogels (**figure 28a-e**), biological gels (**figure 28f**), ion-exchange beads (**figure 28i-j**) and hydrophilic polymer surfaces (**figure 28k-q**).

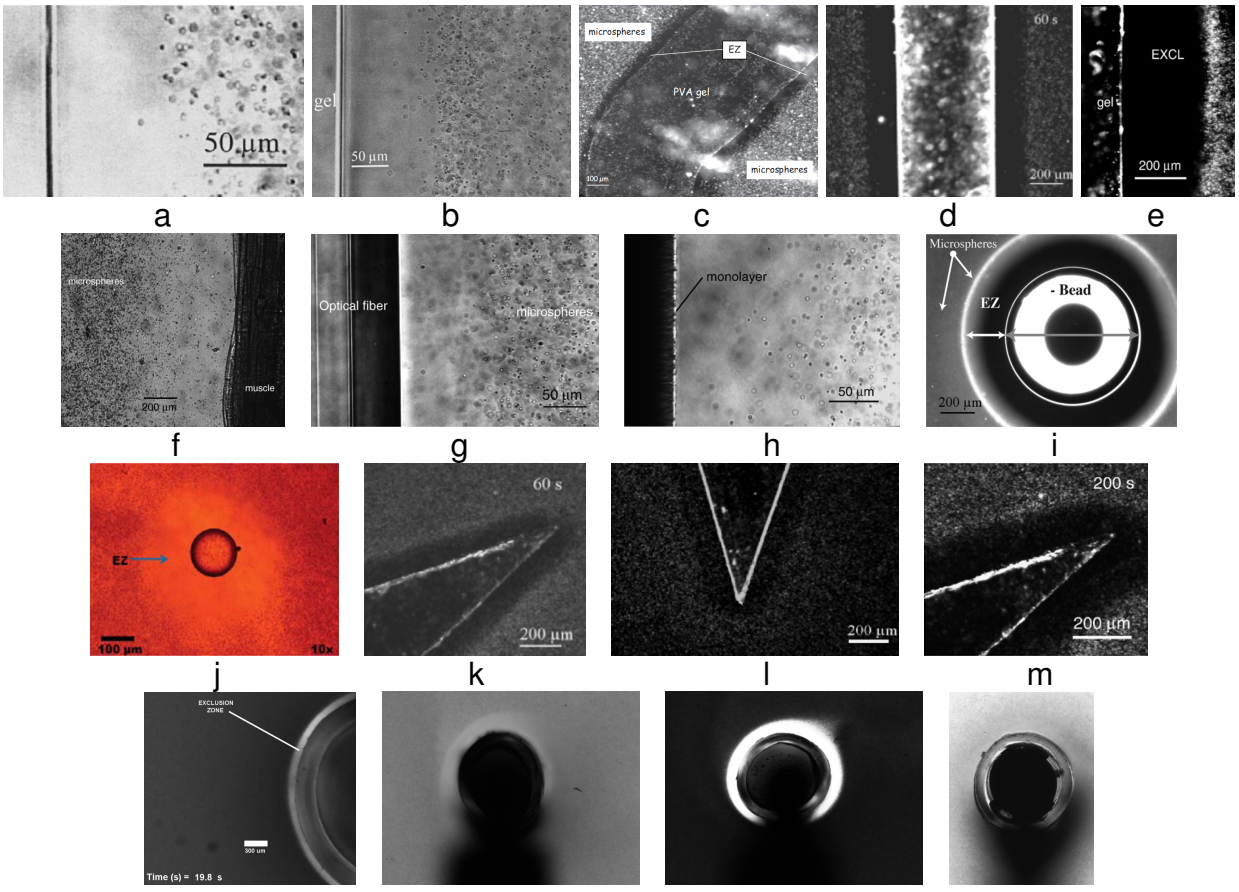

Material Type	Surface	Fig Image	Conc (v/v)	Size (µm)	Type	EZ Size (µm)	Ref
Hydrogels	polyvinyl alcohol (PVA)	a	1:500	2	carboxylate (c)	50-75	104
		b	1:500	1.5	aldehyde/amidine (aa)	~100	104
		c			latex (l)	50-90	1055
	polyacrylic acid (PAAc)			2	c	150	104
				1.5	amidine (a)	120	104
		d	1:100-250	1	sulfonate (s)	150-200	105
		e		1	c	220-250	105,106
	polyacrylamide			2	c	100	104
Biological Gels	200 µm wide rabbit psoas muscle in physiological buffer			1	c	80	104
	rabbit psoas muscle in physiological buffer	f	1:400	1	c	360 ± 50 (n = 8)	106
	agarose at pH 4.0			1.5	a	60	104
Instruments	optical fiber with acrylate coating	g		2	c	75-100	106
	contact lens, polyhydroxyethyl methacrylate (polyHEMA)			2	a	120	104
Monolayer	gold with carboxylate (COOH) groups	h	1:500	2	c	200-275	106
Ion Exchange Resin (Bead)	sulfonate form	i		0.1	s	200-250	109
	chloride form	j	1:500	1	s	100-200	111
Polymer	Nafion-117 sheet	k	1:200-400	1	s	150-175	105
		l		1	a	175-200	105
		m	1:300-400	2	c	~200	106
	Nafion TT-060 tube	n	1:100	1	c	200-300	Das
	Nafion TT-030 tube	o	1:300	1	amino (am)	180 ± 10 (n = 10)	
		p	1:50	1	am	160 ± 20 (n = 10)	
		q	1:400	1	c	175-200	
			1:50-1:500	1, 2, 4.5	c	100-150	
			1:50-1:200	10, 20	c	50-75	Das
			1:50-1:500	1, 2, 4.5	am	200-225	
			1:50-1:500	1, 2	a	50-75	
			1:50-1:500	1	zwitter (z)	50-250	
			1:50-1:500	1, 2, 4.5	polystyrene (p)	100-125	
AVERAGE ± STD ($x_{avg} \pm \sigma$)						145 ± 50	

Figure 28: The existence and size of exclusion zones at various surfaces using microsphere suspensions. The section shaded green are unpublished experiments conducted by the author.

2.4. Evidence of exclusion zones at diverse, hydrophilic surfaces

As discussed earlier, ordering and the extent of interfacial water is highly dependent on a surface's charge, roughness, hydrophilicity and overall geometry. Therefore, a summary of exclusion zone observations under various experimental conditions exploring these very aspects is shown in **figure 28**.

Skinned muscle bundles in physiological saline solution (**figure 28f**), PVA (**figure 28b**) and Nafion (**figure 28n**) are materials with increasing surface charge. All have demonstrated an exclusion zone on the order of 100-200 µm in thickness. A similar sized exclusion zone was also observed for both smooth (**figure 28a**, **g**, **n**) as well as rough surfaces (**figure 28f**, **m**).

Zones seemed unaffected by a nucleating surface's size, or overall geometry, since many observations of exclusion zones have been made next to 1) free-standing sheets and cylindrical surfaces (**figure 28a**, **b**, **e**, **n-q**), 2) hollow/solid cylinders laid flat on the chamber floor (**figure 28c-d**, **g**), 3) spherical geometries (**figure 28i-j**), 4) flat sheets, or edges of flat sheets (**figure 28k-m**) and 5) hydrophilic monolayers (**figure 28h**).

Aside from negatively charged carboxylate microspheres, other suspensions of negatively and positively charged microspheres have also been used as indicators, including sulfonate, amino and amidine coated microspheres (**figure 28**). Dual-charge coated zwitter, uncoated latex and polystyrene, and silica microspheres have similarly

been used to indicate exclusion zones adjacent to hydrophilic surfaces. Irregularly-shaped microparticles, such as top soil, clay, silt, bacteria and viruses have also been excluded from surfaces[108].

2.5. Is it mechanically, or electrically distinct?

It is tempting to assume that if exclusion zones are observed regardless of microsphere charge, then the water within the exclusion zone is just mechanically different. A later discussion will make the argument that it is both mechanically and electrically distinct, but for now, **figure 29** demonstrates a critical feature of the exclusion zone with microsphere suspensions, namely, its unique mechanical properties.

Earlier, projections of the exclusion zone were shown to extend into the bulk region and persisted for long time periods (**figure 27**). When sealed capillary tubes, or tiny needles were used to probe these regions, entrance of the probe tip into the water bath and the surface tension of the microsphere suspension caused disruptions in the continuous structure of the projection. As a result, it was very difficult to observe the projection region. Therefore, the experiment was modified so two standing Nafion tubes were placed next to one another using the same setup as in **figure 20b**, but on a microscope stage. A microsphere suspension was then washed into the chamber. The goal was to

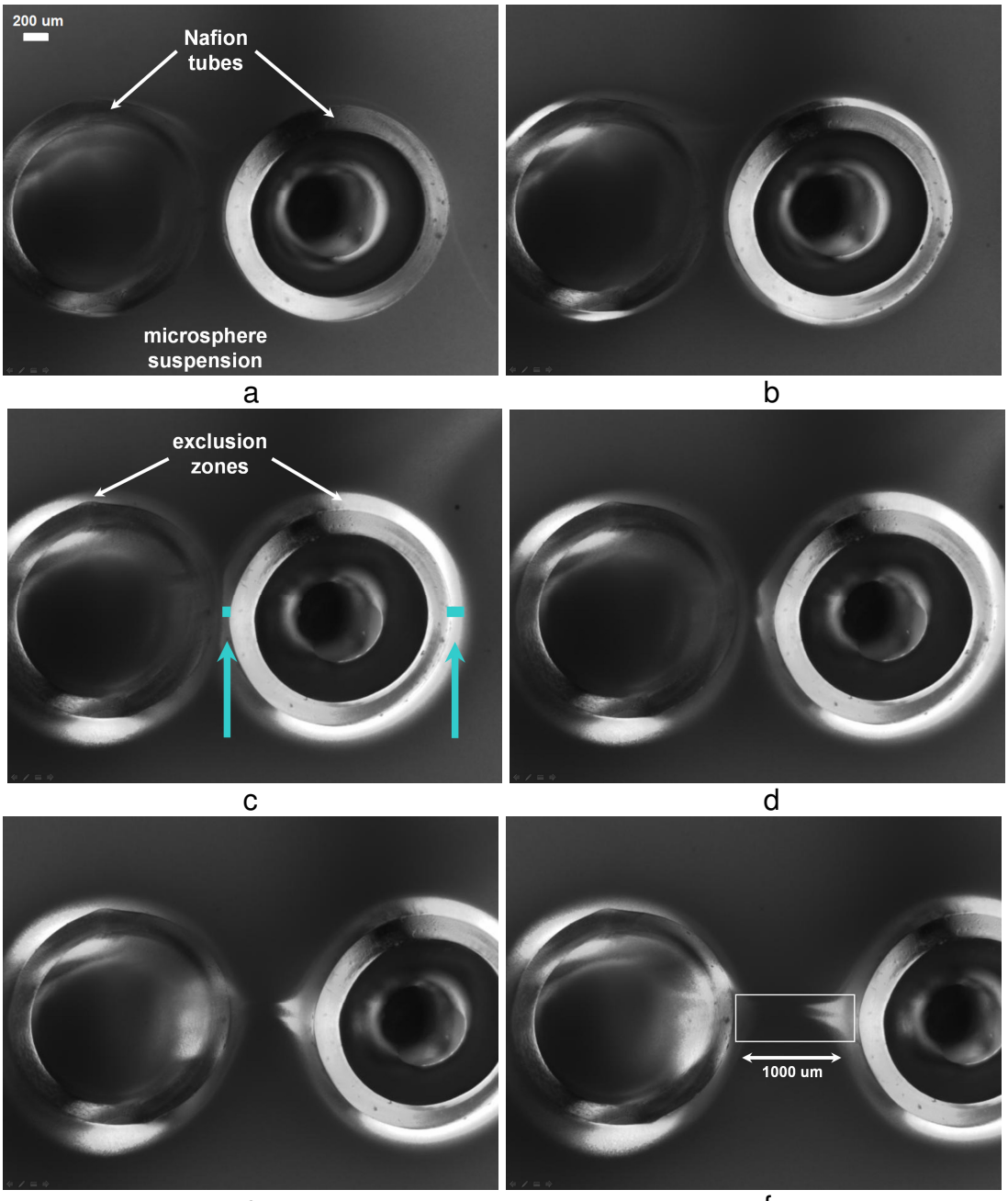

Figure 29: An example of the mechanical distinctiveness of the exclusion zone. a-c) After two Nafion tubes were pushed together, a microsphere suspension was washed into the chamber. Two corresponding exclusion zones ~200 µm thick formed adjacent to one another. c) It seemed as though the two zones mechanically impeded each other, since a "flattened" interzone region was observed, similar to when two balls of jelly are pressed together. The exclusion zone thickness within the in between region was also less than the outer region (see length of blue rectangles). d-f) When one tube was pulled away, a bridge from one exclusion zone to another was maintained and in the video exhibited viscous, gel-like flows. This was similar to observations of exclusion zone projections in figure 27 and is elaborated upon in a later section of the document.

observe adjacent exclusion zone formation and/or projections, and see if zones simply excluded microspheres and grew into each other like two mixing dyes, or if corresponding exclusion zones would sterically interact.

When one Nafion tube was suddenly pulled away, a similar exclusion zone projection (**figure 27**) was produced, except in this case, the projection was a bridge between the two corresponding zones. Interestingly, the flow of this region was visually gel-like and moved more slowly with respect to the translating Nafion tube (implying viscous-like behavior). In video, this bridge was maintained between the corresponding exclusion zones for nearly 15 min and over a distance of 1-2 mm. A similar effect was also observed when very dilute microsphere suspension concentrations were used. Therefore, one question that naturally arose was if the exclusion was a homogeneous, mechanically distinct structure, or if the zone simply exhibited a viscosity greater than bulk water.

To explore this question, an even simpler experiment was conducted using falling microspheres in a vertical chamber with a Nafion floor. After pipetting a volume of water into a chamber, 4.5 μm carboxylate microspheres were "sprinkled" into the bath and allowed to fall onto the chamber floor that was covered with a Nafion sheet (**figure 30**). As microspheres descended within the deep chamber, their vertical velocities began to decrease as they approached the exclusion zone. With some microspheres, particles stopped completely at the exclusion zone boundary, while

other microspheres stopped their vertical translations and instead, began to translate laterally (**figure 30**, green arrow).

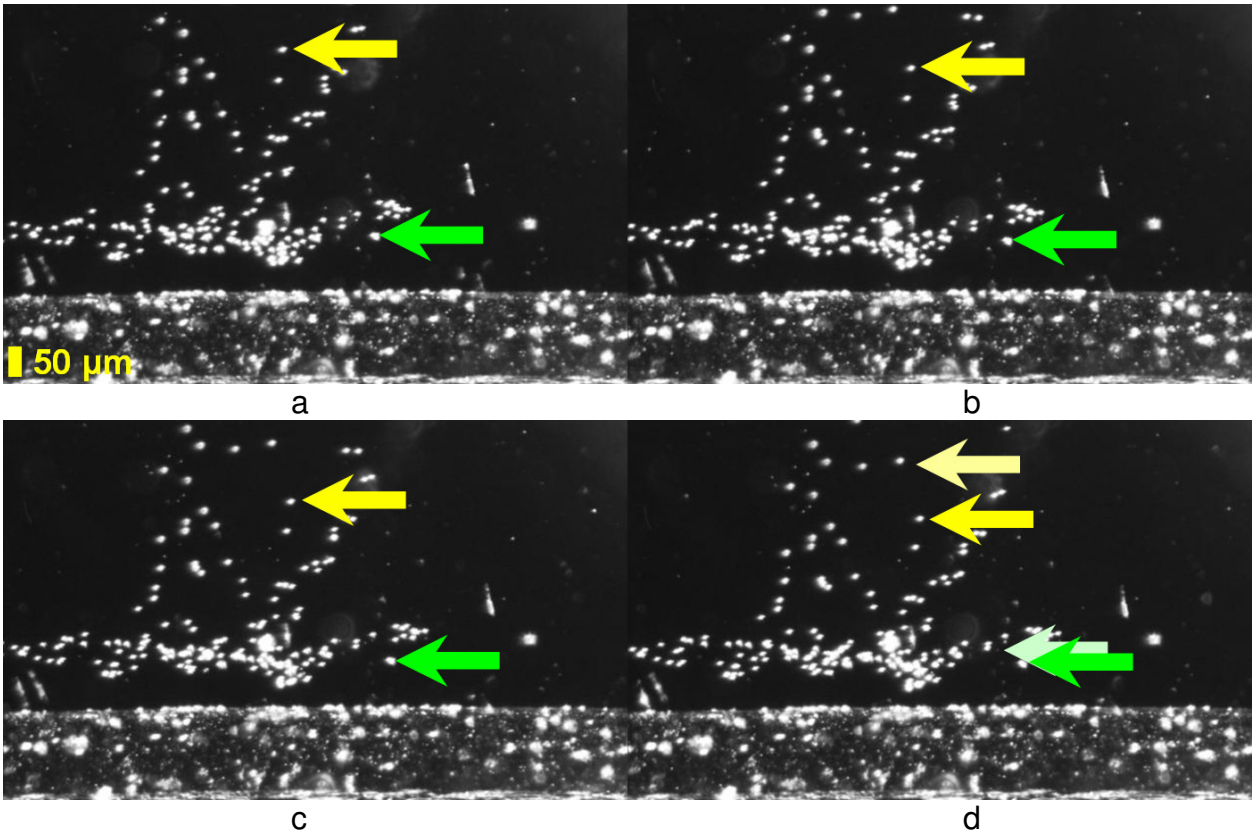

Figure 30: Falling ball experiments using microspheres dropped into a water-filled chamber that had a floor consisted of a Nafion sheet (Yoo, unpublished). a-d) If we keep track of the yellow arrow pointed at the 4.5 µm diameter microsphere, one can see that the microsphere was slowly falling towards the Nafion floor. As it approached the interface, distance measurements revealed that the microsphere slowed down. The light yellow arrow in d denotes the initial microsphere position in a. The green arrow indicates a microsphere that reached the exclusion zone boundary and began translating laterally, albeit more slowly than the vertical translation rates. The light green arrow denotes its initial position in a. The exclusion zone at the Nafion surface in this experiment was 50-80 µm in thickness.

Is the force preventing microsphere penetration of the exclusion zone mechanical, or electrical? From a mechanical point of view, how much weight is the exclusion zone taking on? Microspheres consist of a density that is approximately 1.3 g/cm^3. Therefore, a lower estimate for the amount of force the exclusion zone had to maintain

to uphold 100 microspheres was calculated to be ~200 pN. In experiments where a greater concentrated microsphere suspension (1:50 v/v) was used (**figure 21**), the total theoretical force required to exclude 1 µm carboxylate microspheres from a region 300 µm thick and 1 mm deep is about 5 nN. This force is on the same order of magnitude as the weight of an average mammalian cell.

While it is easy to assume that the exclusion zone could be a band of material that is more dense than water, it should be noted that microspheres did not abruptly stop at the interface. Particles gradually slowed down and stopped, or stopped and translated horizontally, which implies that either density, or viscosity is increasing within the exclusion zone regions as microspheres approached the Nafion surface. Horizontal translations were also much slower than vertical translations, but not constant, implying anisotropy of the region. Because of these arguments, three questions of logic come to mind:

1) *Based upon vertical translations towards the surface, is each layer of the zone progressively more ordered?*

2) *Based upon horizontal translations, are ordered layers continuous along the length of a nucleating surface?*

3) *Could electrical phenomena (i.e., electric fields) be responsible for the slowing and eventual halting of the microsphere?*

2.6. Measurement of force at the exclusion zone

To directly measure force experienced by microparticles at the exclusion zone, individual microspheres were directly attached to a sensor (**figure 31a**) previously developed to measure force in skeletal muscle protein[112]. Force sensors were then translated by a motor towards an exclusion zone to determine if a significant force was exerted on the microsphere and could be measured.

Subsequently, 20 µm carboxylate microspheres were attached to the tips of microfabricated nanolever force sensors using a sticky nitrocellulose glue. Nanolevers were manually isolated from batch-fabricated silicon wafers (**figure 31a-d**) and attached to a sensor holder (**figure 31e**). The sensor holder was manipulated within the workspace of the chamber using the piezoelectric motor-controlled micromanipulator described earlier (**figure 31f**). A vertically positioned Nafion tube was held in place in a similar fashion to **figure 20b** (**figure 31f**) and served as the exclusion zone-generating surface.

Manipulators then translated sensors towards a 1 µL drop of nitrocellulose placed on a coverslip in the chamber. Through a custom technique, only the tip of the nanolever was coated with a sticky nitrocellulose solution (**figure 31g-i**). After removing the coverslip, the chamber was filled with a bath containing 5-10 microspheres 20 µm in diameter. Through an additional custom technique, one microsphere was attached

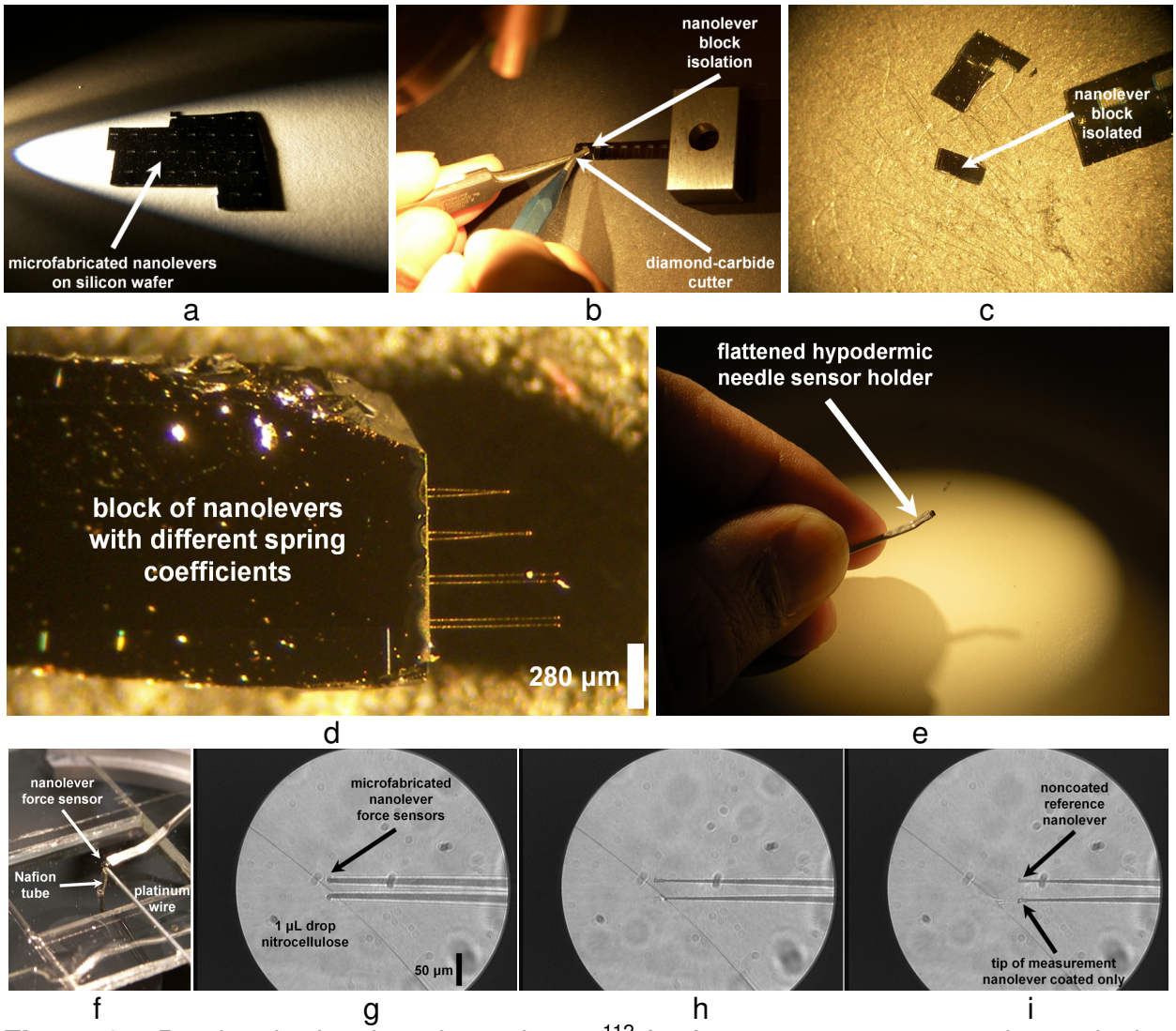

Figure 31: Previously developed nanolevers[112] for force measurement at the exclusion zone. a-f) The most compliant (longest) nanolevers were manually isolated and attached to a holder for micromanipulation. g-i) After coating one nanolever tip with a sticky glue, a single microsphere was attached to the sensor. See text for more details.

to the tip of the measurement nanolever (**figure 32e**). The most compliant (or longest) nanolevers were used for experiments, thus with a 40x objective which could visualize minute deflections, forces on the piconewton level were measured.

A new Nafion tube holder (**figure 32a-d**) in later experiments was attached to a manual micromanipulator and translated tubes (with a section of their outer edges removed,

figure 32b) into the water bath (**figure 32c**). This modification (**figure 32c-e**) permitted the entire tube to be brought as close as possible to the nanolever, but positioned the exclusion zone-generating surface at a distant location. This setup served as a control. The tube was then rotated and brought the exclusion zone-generating surface near the sensor assembly (**figure 32d-e**). This setup served as the actual experiment.

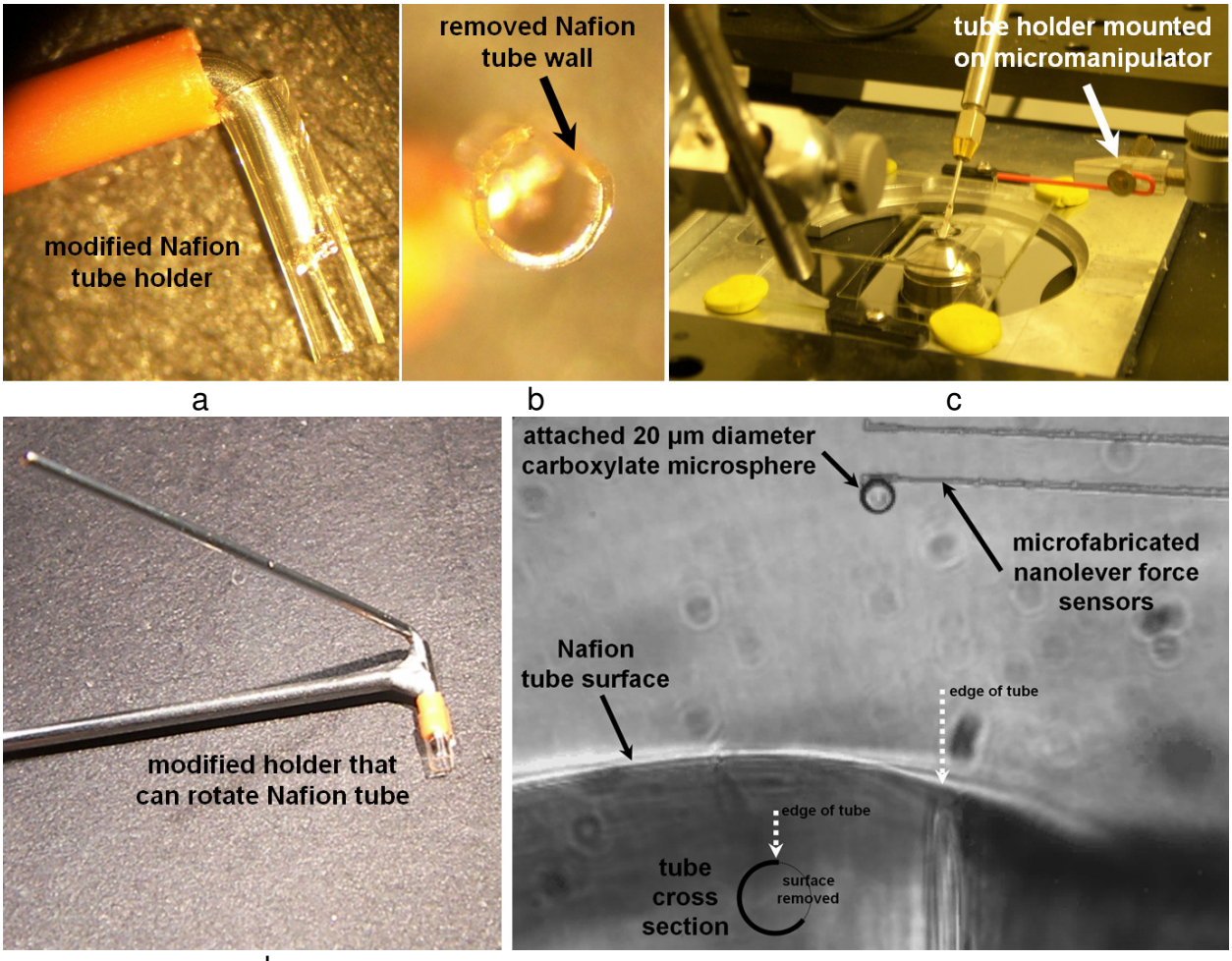

Figure 32: Nanolever[112] force measurement of the exclusion zone and the experimental setup. a-e) A Nafion tube was held by a modified holder which could rotate the tube sample. Tubes were positioned within 150 µm of the nanolever system in water and the tube was then rotated to bring the exclusion zone-generating surface into the field of view for experimentation. The assembly was then translated through the exclusion zone towards the Nafion surface to determine if a repulsive force could be measured by the nanolevers. See text for more details.

At velocities 1-25 µm/s, the assembly was translated towards the Nafion surface (**figure 33b-c**). Nanolever positions were recorded via video and the PDA system (**figure 22**); the difference between the nanolever positions was measured and plotted (**figure 33a, d**). In this fashion, nanolever deflections yielded a force as the assembly was translated from the bulk water, through the exclusion zone and towards the Nafion surface.

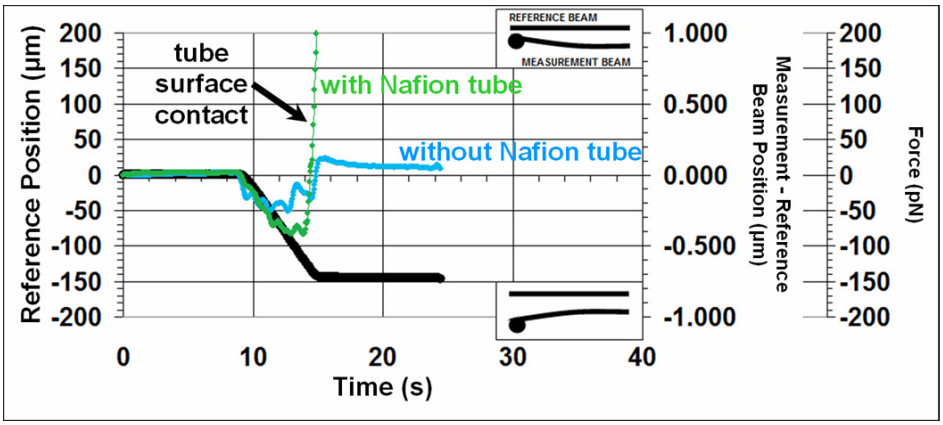

a

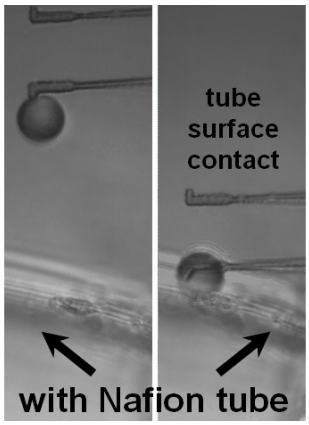

b c

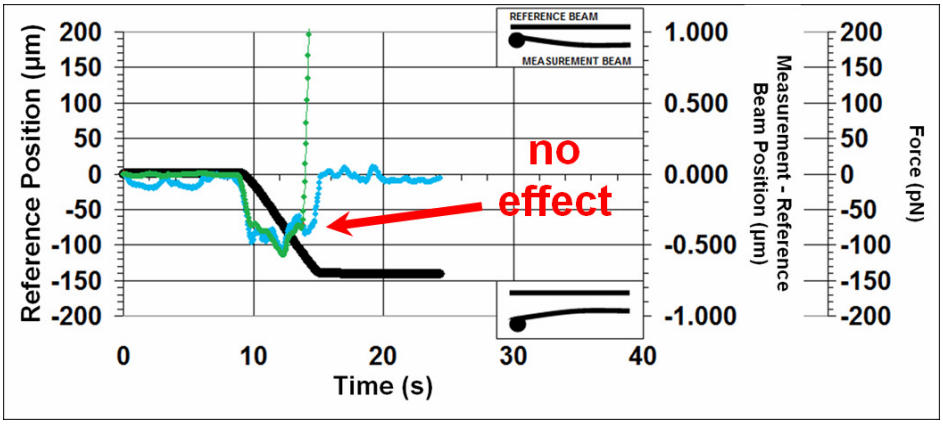

d

Figure 33: Results of force measurements using a microsphere-attached nanolever. The sensor was translated through the exclusion zone at 25 µm/s. a) Black record indicates the position of the reference nanolever as the assembly was translated towards the Nafion surface. Colored records are averages of five experimental runs of the differences measured between the nanolevers as the sensor was translated when a Nafion surface was present (green), or absent (blue). Negative-going deflections denote an attractive force (illustrated by the cartoon of the separating nanolevers). A rapid upward deflection in the green record indicates when the microsphere made contact with the Nafion tube (shown in c). While initial experiments measured an attractive force on the order of 50-100 pN (~300 nm nanolever deflection), noise level and variability were too high within corresponding records and between experimental runs. d) A typical example demonstrating no effect of the exclusion zone.

It was hypothesized that a repulsive force would be measured by the sensor. Therefore, as a positive control, the assembly was translated in a fashion so that the microsphere made contact with the Nafion surface at the end of the experimental run (**figure 33c**). This was denoted quantitatively as a rapid and sudden deflection of the recorded data (**figure 33a**, in green). Attention was thus paid to what occurred between the start of translation and the contact made by the microsphere. **Figure 33a**, **d** are results of the experiment. In **figure 33a**, an attractive force was recorded relative to control before the assembly made contact with the tube surface. This is visualized as a more downward deflection of the green record during translation in comparison to the blue record. The blue record were data measured when no tube was present. While initial experiments demonstrated an attraction between the attached microsphere and exclusion zone, records were too noisy to ascertain a consistent effect. This is seen in the spurious deviations of the records during translation of the sensor. Variations between experiments was also very high and in some cases, the green and blue records were coincident with each other (**figure 33d**), demonstrating no effect of the exclusion zone on the microsphere. Therefore, within the timeframe and obtained data, these experiments were considered inconclusive.

2.7. Microsphere suspensions

A large number of experiments within this dissertation employed 1 µm carboxylate microsphere suspensions to visualize the exclusion zone. Similarly sized, positively charged microspheres were also used to display equal exclusion zones with minor

variations. A summary of the microsphere types used in previous experiments was covered in an earlier summary (**figure 28**).

However, while suspension concentration (1:500 v/v) was standardized based on previous investigations[104,106,110], further justification will be given why the use of highly concentrated, or highly dilute suspensions was avoided in experimental measurements. The first, most obvious reason was visualization. When microsphere suspensions were too dilute (≤ 1:800 v/v), exclusion zone boundaries were difficult to resolve optically. This effect was more pronounced when large microspheres were used, since stock concentrations of these microspheres were already very dilute.

An additional reason why the use of large microspheres was avoided is sedimentation. Microspheres with diameters greater than 4.5 µm settled much faster to the bottom of a chamber. This was due to microsphere density, which varies from 1.1-1.4 g/cm^3 for microspheres 1-20 µm in diameter. Therefore, while the direction of force for all microspheres is downwards (i.e., sedimentation), the magnitude of the force varies greatly between microspheres. For example, the magnitude of the downward force for a 1 and 20 µm diameter microsphere, accounting for buoyancy, is 0.08 and 45 pN, respectively. Although the larger microsphere is 20 times the size of the smaller one, it experiences a downward force nearly 600 times greater in comparison. As a result, 20 µm microspheres suspended in a water bath 1-2 mm deep settled to the bottom of the chamber within 5 min.

On the other hand, highly concentrated microsphere suspensions had two effects. First, concentrated microsphere suspensions scattered light to a much greater degree than standard concentrations. Consequently, light from the microscope condenser had to be increased in order to visualize exclusion zones. At high magnification, the increase in light caused significant heating (convection) in the chamber, which was responsible for measurement errors. Secondly, highly concentrated microsphere suspensions were found to dramatically alter the pH of the bulk microsphere suspension (**figure 34**). When pH-dye was added to concentrated microsphere suspensions, solutions changed color depending on the charge of the microsphere used. For carboxylate microspheres, concentrated suspensions produced a deep red color. For amino, a deep blue color was visualized.

Explanations for the shift in pH are explained by the association/dissociation reactions of the functional groups along the outer surface of the microspheres. For carboxylate functionalized microspheres, the reaction is pushed towards dissociation, such that

$$MS\text{-}COOH_x \rightarrow MS\text{-}COO_x^- + xH^+ \rightarrow xH^+ + xH_2O \rightarrow xH_3O^+$$

The carboxylate groups along a single microsphere release a proportion of protons that produce greater hydronium concentrations. While the microspheres in this case are negatively charged, they are suspended in a bulk microsphere suspension which has an overall lower pH, or is more acidic.

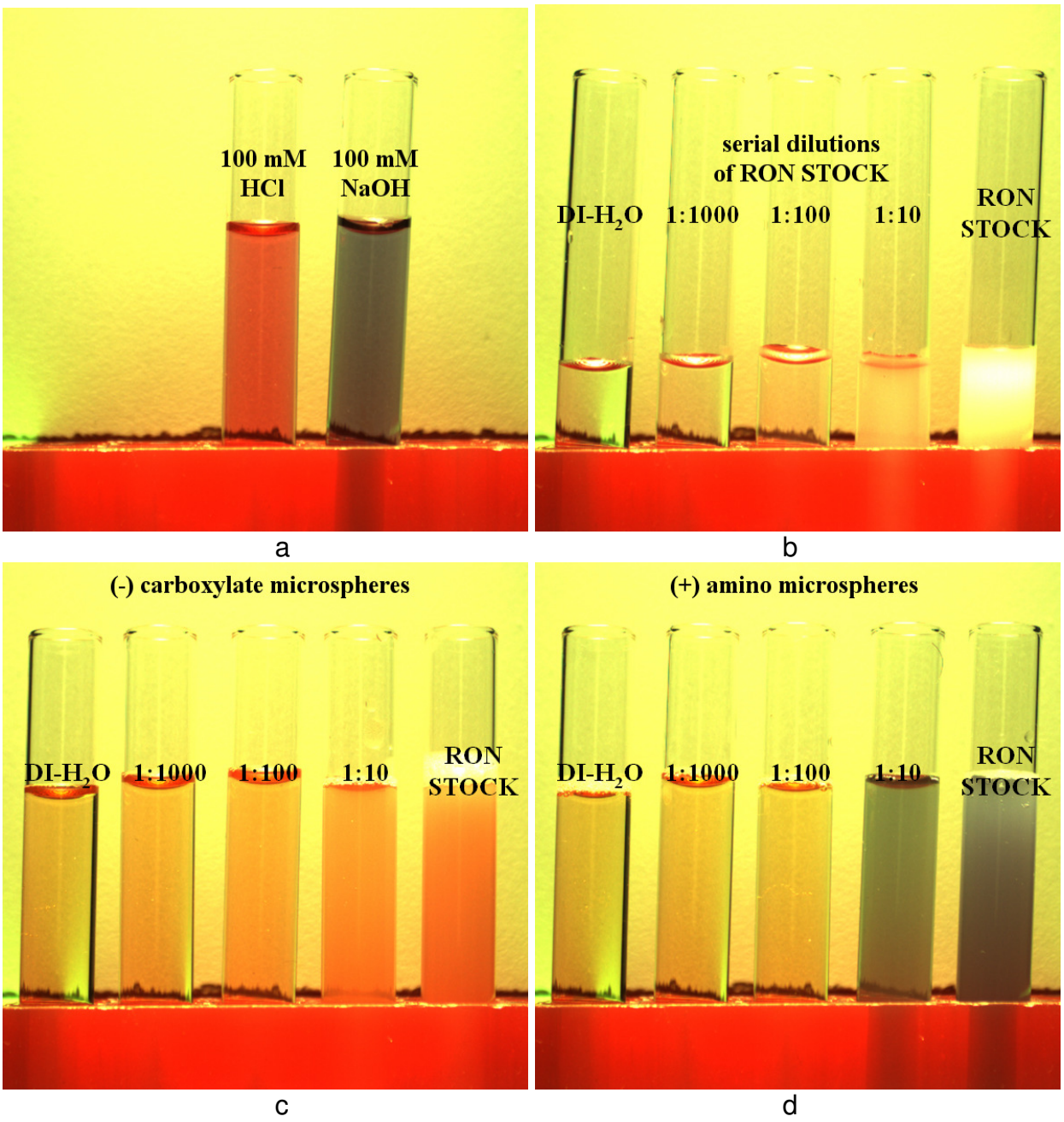

Figure 34: Applications of pH-dye to highly concentrated microsphere suspensions. a) pH-dye was added to a pH 0 (100 mM HCl) and pH 14 (100 mM NaOH) solution. b) Carboxylate microsphere suspension concentrations decreasing from right to left through serial dilution. RON STOCK corresponds to a suspension concentration of 1:40 v/v. The test tube on the very left contained water directly dispensed from the purification system. c) pH-dye was added to test tubes containing carboxylate microsphere suspensions. Colors from right to left: red, light red, reddish-orange, orange and light orange. d) pH-dye was then added to test tubes containing amino microsphere suspensions. Colors from right to left: blue, green, medium to light orange, medium to light orange and light orange.

In comparison to amino microspheres, the reaction with water is pushed more towards association where

$$MS\text{-}(NH_2)_x + H_2O \quad \rightarrow \quad MS\text{-}(NH_3)_x^+ + xOH^-$$

which leaves positively charged microspheres in a bulk suspension of water that is more alkaline. The transition of the colors from blue to green for amino microspheres (**figure 34d**) demonstrated that the suspension transitioned more quickly to more neutral pH values in comparison to the carboxylate microsphere suspension. This was in agreement with what is known about amino microspheres in that the density of amino groups along the surface is much less than similarly produced carboxylate microspheres ($\sigma_{carboxylate}$ = 11.4 μC/cm^2 → 2.2x10^6 electrons/carboxyl groups per 1 μm carboxylate microspheres[104-106]). When other microsphere types (i.e., amidine, carboxyl, polystyrene, sulfonate) were used, similar trends were displayed depending on the charge of the microsphere. Consequently, to avoid adverse pH effects, exclusion zone observations were accomplished with suspensions that were concentrated between 1:50-1:500 v/v.

Nevertheless, in suspensions, it was unknown if the number of protons, or hydroxide ions released by microspheres were electrostatically balanced by the oppositely charged particles. Therefore, at standard concentrations, microsphere charge was additionally checked through a system that applied voltage directly to a microsphere suspension in the chamber (**figure 35**).

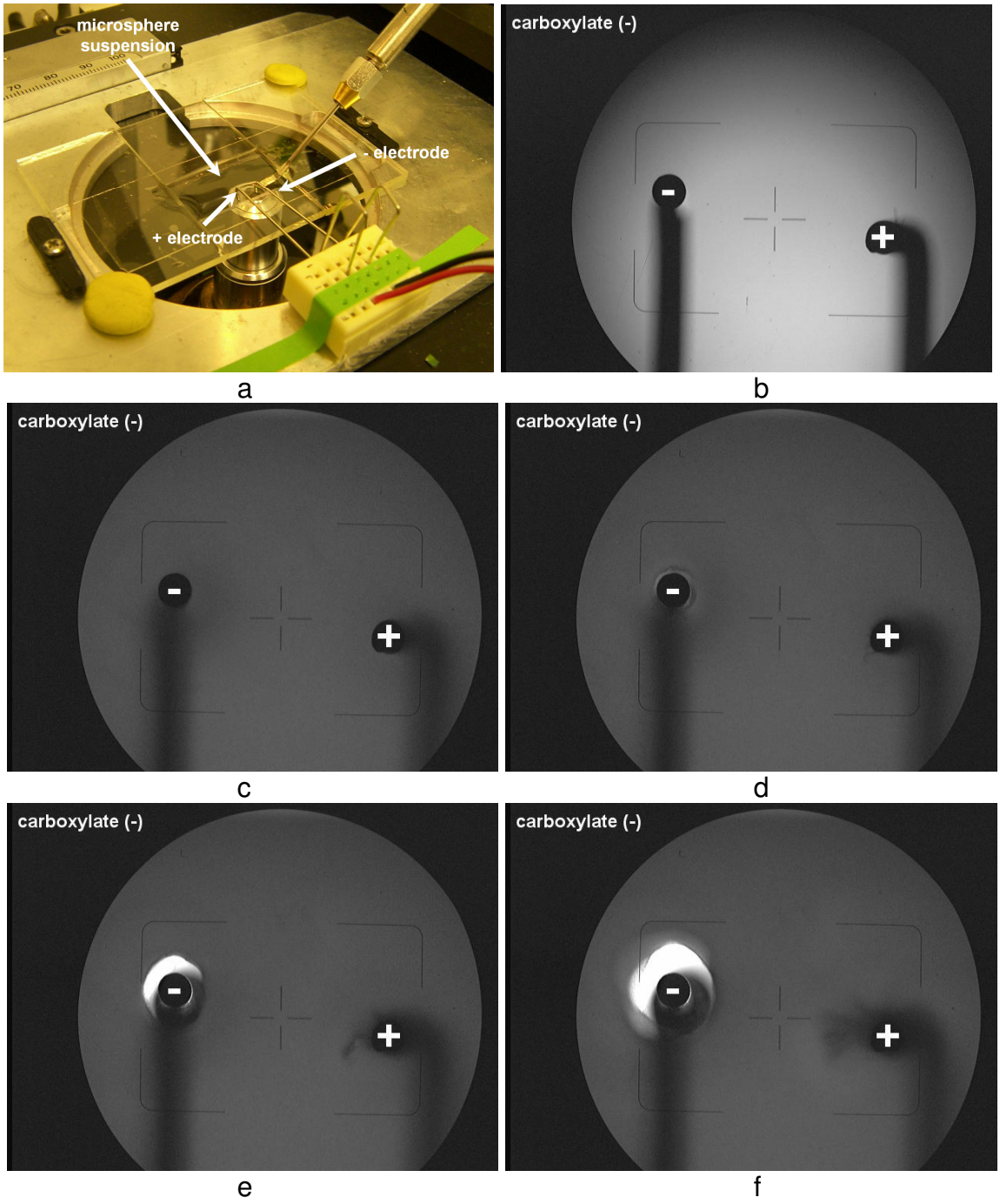

Figure 35: Microsphere charge checking system. Within the same chamber that was used for all the experiments presented in this dissertation (a), a second platinum wire was added alongside the original platinum wire mechanical scaffold. With the Nafion tube absent, both wires were connected to a constant voltage source such that within the chamber (b), the wires acted as a cathode and anode. When a carboxylate microsphere suspension was washed in (c) and the voltage was turned on (d), the negatively charged carboxylate microspheres were electrostatically repelled from the negative electrode, which confirmed the charge of the microsphere suspension.

2.8. Modulating exclusion zones

2.8.1. Applications of voltage

Earlier, a question was raised that aside from mechanical property differences, could exclusion zones be electrically distinct (**figure 30**). Specifically, could electric fields at the exclusion zone play a role when microspheres were excluded (**figure 21**), or when falling microspheres were brought to a halt at the periphery (**figure 30**). Therefore, the system used in the previous section to check microsphere charge was employed so that the positive anode was covered with an exclusion zone-generating Nafion tube. If the zone is simply a mechanical structure, then with a carboxylate microsphere suspension, the negatively charged particles should simply accumulate at the periphery of the exclusion zone when the voltage is turned on.

Figure 36 demonstrates an interesting finding in that when the voltage was turned on (**figure 36c-f**), the exclusion zone size began to decrease in thickness. Microspheres at the outer exclusion zone boundary invaded the interior region and eventually made contact with the Nafion tube surface. One initial interpretation is that if the exclusion zone is charged, such that it has a negative electrical potential, then removal of negative charge via the positive electrode, should decrease the exclusion zone size at the Nafion surface. This would allow the microspheres to become attracted to the anode through simple electrostatic interactions. In a later section it is confirmed that

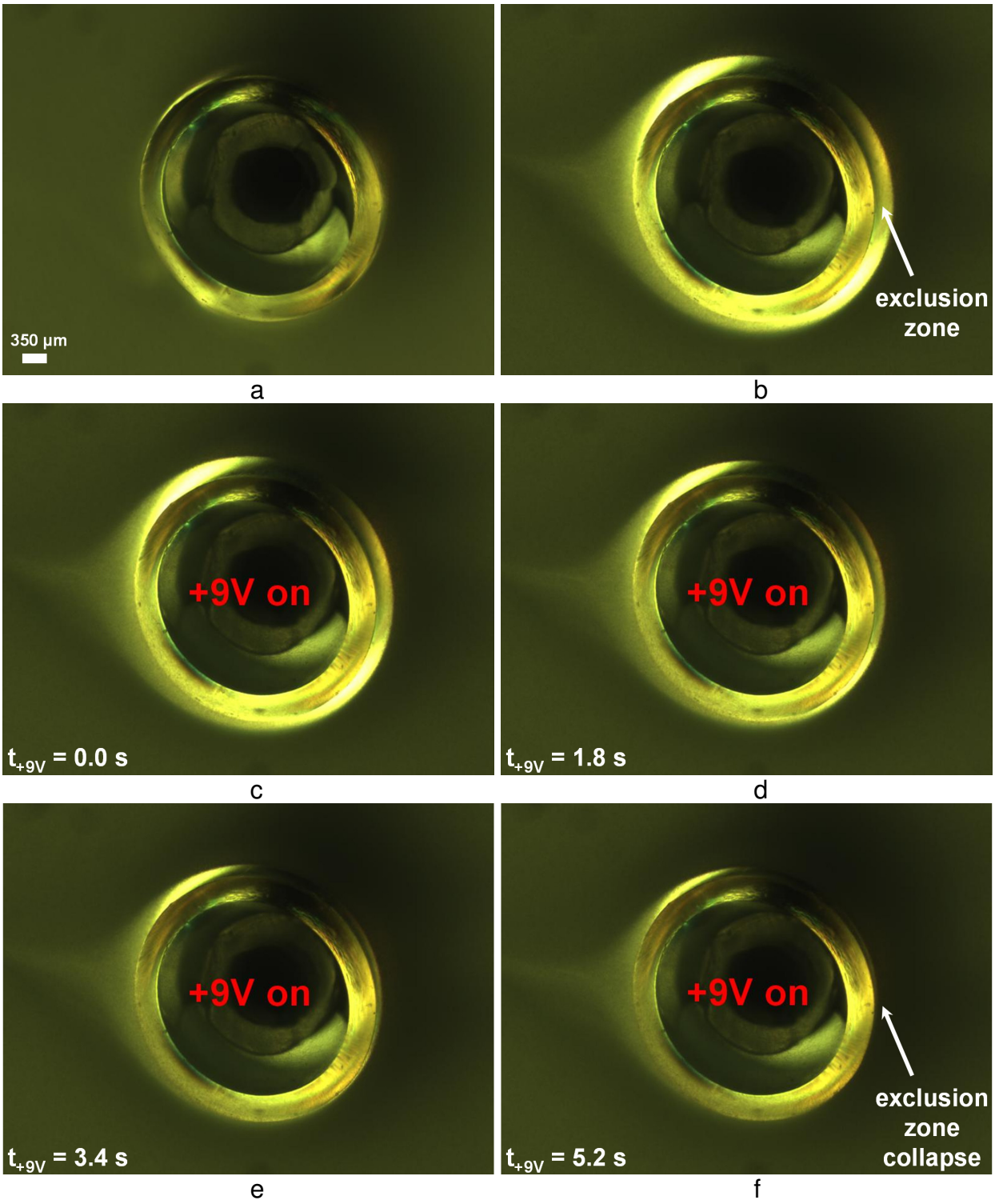

Figure 36: Applications of voltage to a pair of electrodes; only the anode is covered with a Nafion tube. a-b) A microsphere suspension in the chamber indicated the presence of the exclusion zone on the order of 300-350 µm. c-f) When the voltage was turned on, the exclusion zone shrunk in thickness and the boundary of the microsphere suspension approached the surface of the Nafion tube. Within 10 s, the exclusion zone was completely absent.

the exclusion zone is indeed negatively charged, thus voltage applications here demonstrate that the exclusion zone mechanism may be based on both mechanical and electrical properties.

When positively charged amino microspheres were used, results were highly variable and inconsistent. In some cases, the microsphere-free region at the Nafion tube-covered cathode (not anode) would shrink in size, in others, regions would grow. As a result, it was difficult to discern if the exclusion zone was changing in size, or if the microspheres were simply being electrostatically attracted, or repelled by the electrode itself; if the former case was indeed true, then particle invasion into the exclusion zone region rule outs the possibility that the exclusion zone phenomenon is a purely mechanical structure.

Originally, we hoped that at the cathode, the exclusion zone would be maintained and prevent positively charged microsphere migration towards the electrode surface. Variability may have been due to the fact that amino microsphere surface charge is less dense and (by manufacturer confirmation) chemically less stable in comparison to carboxylate microspheres (see section on microsphere suspensions). Therefore, the observed effects may likely have been influenced by a dual-charge property of the amino microspheres: particles incompletely covered by amino groups may have had exposed patches of their inner, negatively charged polystyrene cores on the microsphere surface. These patches could have thus electrostatically interacted with the surrounding environment and caused the inconsistent results.

2.8.2. Salt concentrated solutions

If exclusion zones are charged, then aside from voltage applications, microsphere suspensions with salt may modulate zone size since ions carry charge and reduce any inhomogeneous electrical potential developments in aqueous solution by dissipating charge separation. In previous work[104], microsphere-salt concentrations were used for experiments, but suspensions were pH buffered, therefore in the following experiments only salt was added to microsphere suspensions (**figure 37**).

2.8.3. Exposure to UV light

It has been shown previously that exclusion zones are regulated by incident light from the environment, specifically light within the IR spectrum[110]. While water absorbs IR radiation quite readily and is reflected in the macroscopic thermal properties of bulk water, ultraviolet (UV) light is roughly 100-1000 times more strongly absorbed than IR (**figure 38**).

Therefore, two simple setups were employed to study the exclusion zone size with exposure to UV light. The first setup used microsphere suspensions on a microscope and the second, pH-dye within the macroscopic setup used early on (**figure 39**). A UV light source with a peak wavelength at 362 ± 30 nm (λ_{violet} = 390 nm) was used and corresponded to the minimum most region of the water absorption spectrum.

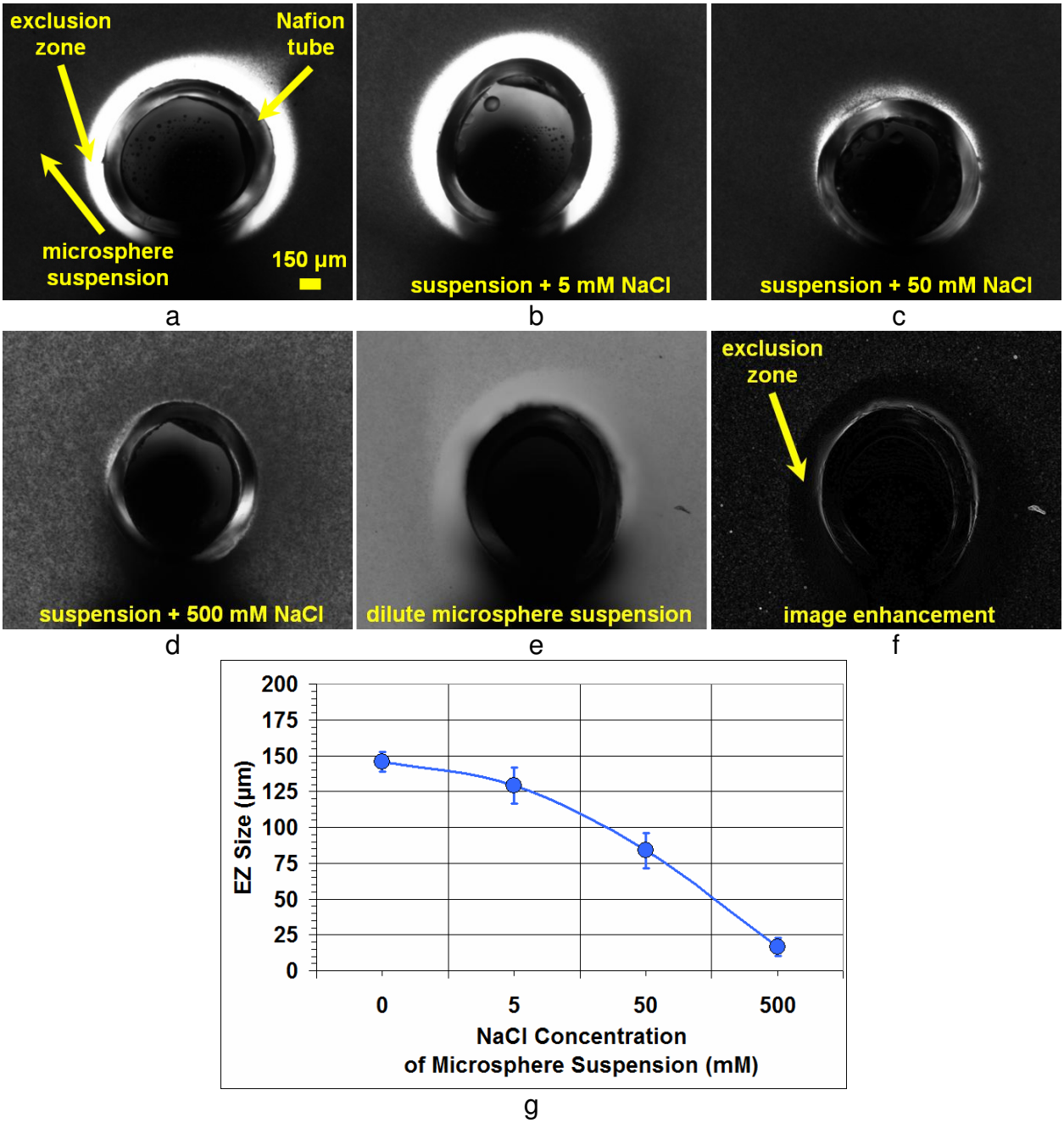

Figure 37: Observations and measurements of exclusion zones using microsphere suspensions with added NaCl. a-d) Exclusion zones around Nafion tubes with increasing salt concentrations. Differences in suspension color, or graininess, were simply due to lighting. At 500 mM NaCl, comparable to physiological solutions, there was still an exclusion zone in the upper left quadrant of the Nafion tube. e-f) Ultradilute suspensions with salt were also used. In order to visualize the exclusion zone, image enhancement via edge detection was performed on corresponding images. g) Three measurements of zone thickness around a Nafion tube (n = 5 tubes) were averaged and plotted for each salt concentration. Standard and ultradilute suspensions, and negatively and positively charged microspheres demonstrated similar results and agreed with past work[104].

To first characterize the proton-enriched zone in the bulk water, Nafion tubes lengths (0.1, 0.5, 1, and 2 mm) were used in chambers. Five thickness measurements of the proton concentrated region were made about the Nafion tube (n = 3 tubes for each length). Measurements were averaged every 10 s for 5 min experiments and are displayed in **figure 40a**.

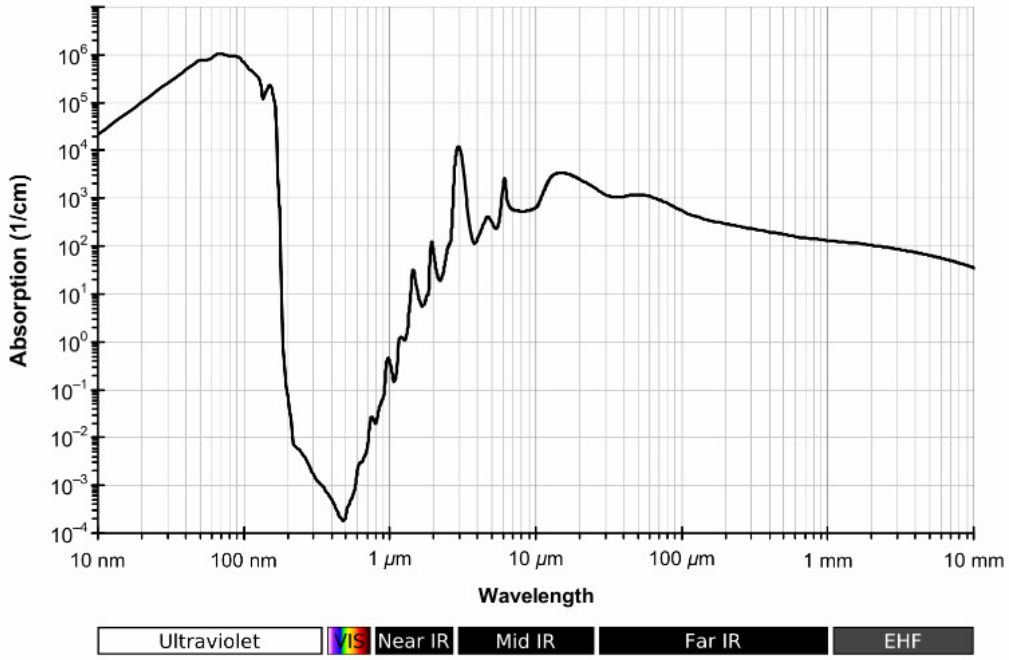

Figure 38: Water absorption spectrum of electromagnetic radiation[113]. UV light is strongly absorbed by water. While broadband IR is also readily absorbed by water, there exist several wavelengths (peaks) in the near- and mid-IR spectrum where water absorption is particularly high (i.e. λ = 2.0 and 3.1 μm) in comparison to UV.

In UV experiments, thickness of the proton-rich bulk water region was measured in three directions around a 1 mm long Nafion tube (n = 5 tubes) at 5 and 15 min. The thickness was measured at the set time points by switching on the illumination platform at the given time and recording an image. For all other times, the lighting was off, thus heating and other lighting effects from the platform were minimized. Results in

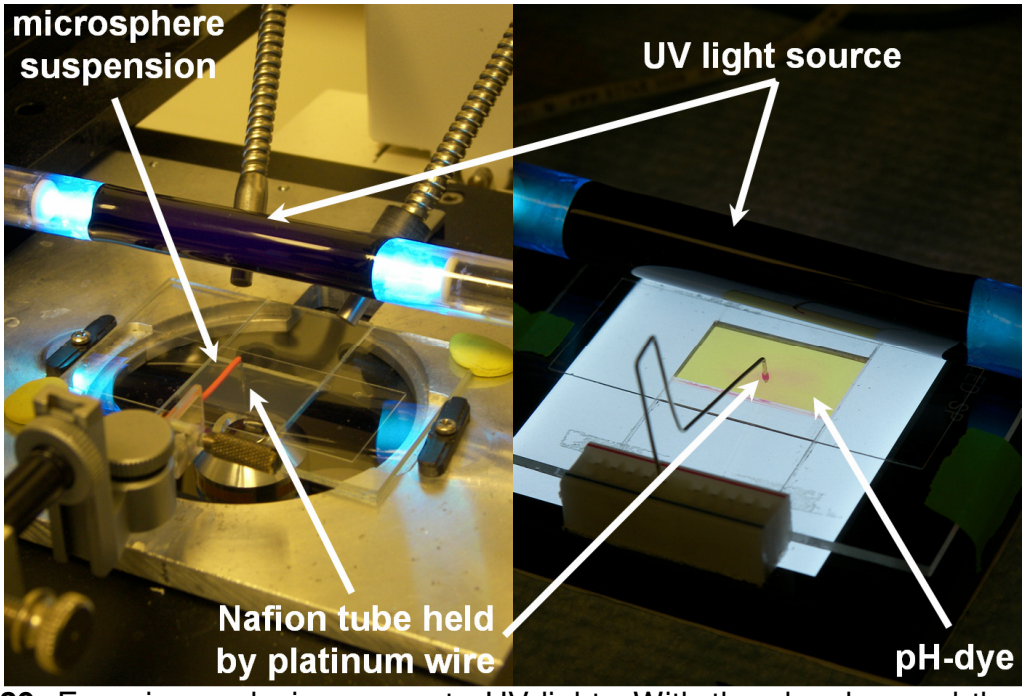

Figure 39: Exposing exclusion zones to UV light. With the chamber and the upright-held Nafion tube in place, observations were made of exclusion zones with both microsphere suspensions in the microscopic setup (left) and with pH-dye in the macroscopic setup (right).

figure 40b-top demonstrate that after 10 min of UV exposure (following 5 min of initial exclusion zone formation and stabilization), the thickness of the proton concentrated region increased by nearly 95%.

Interestingly, when a concentration of carboxylate microspheres was used instead of pH-dye, exposure to UV light caused an overall decrease in the exclusion zone size (**figure 41**). When five measurements around three samples of Nafion tubes were averaged, data demonstrated that UV exposure decreased the size of the exclusion zone by nearly 40% (**figure 41b**, middle and right bars), whether the UV application began once the exclusion zone stabilized at the 5 min set point (**figure 41a**, middle bars), or throughout the initial 5 min formation (**figure 41a**, right bars).

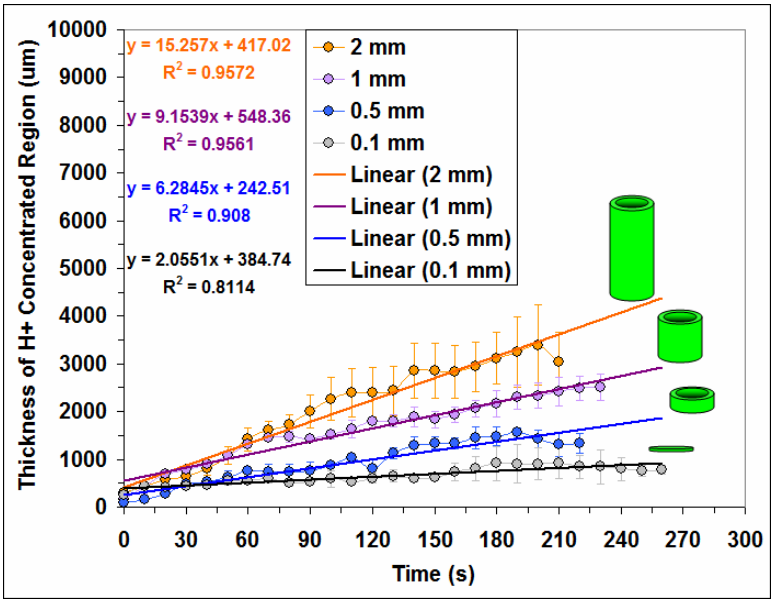

a

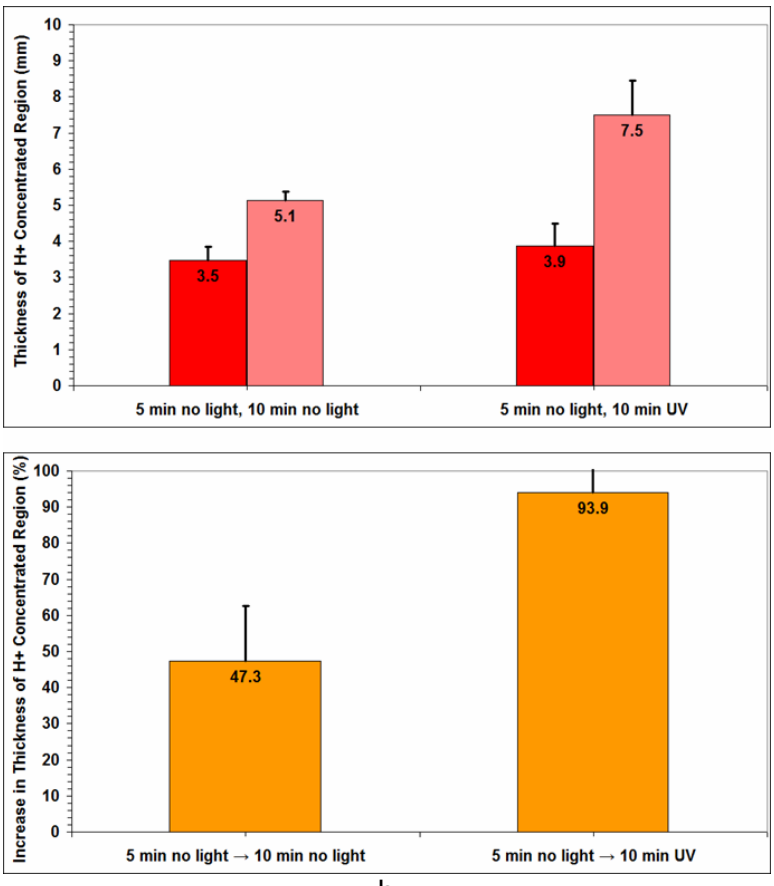

b

Figure 40: Thickness measurements of proton concentrated regions in the bulk water beyond using pH-dye. a) Measurements for different length Nafion tubes over 5 min experimental runs. b) Comparison of the growth of the proton concentrated region with and without exposure to the UV light source.

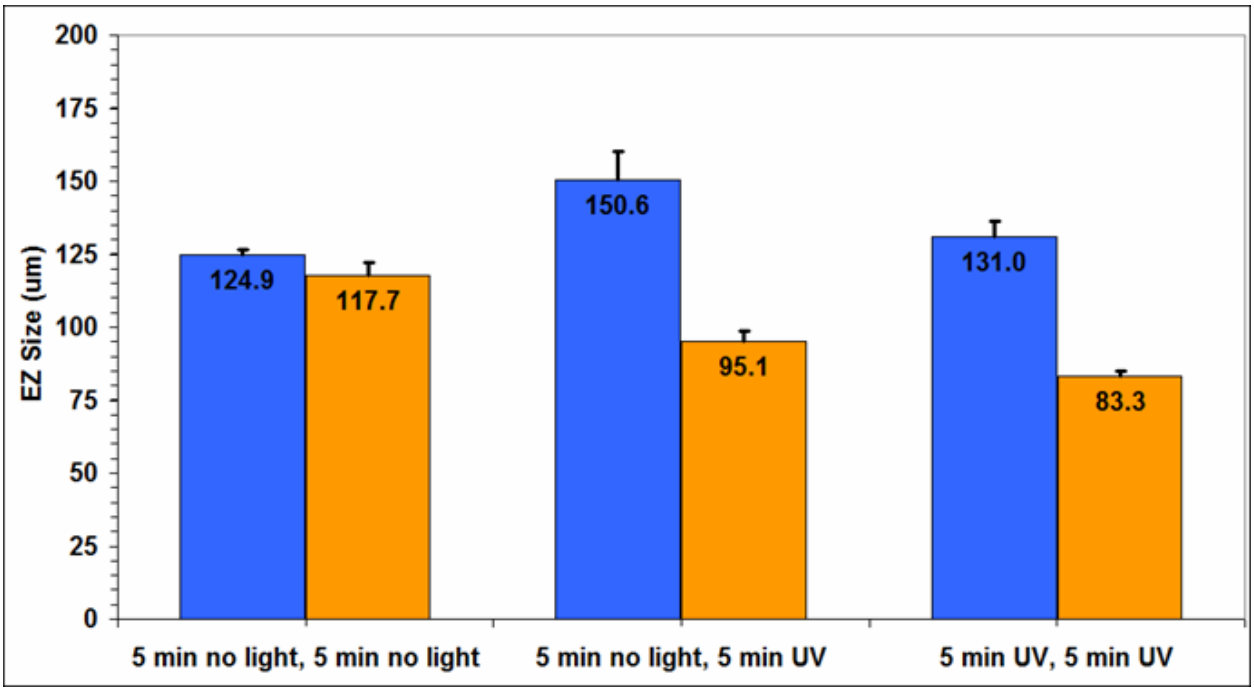

a

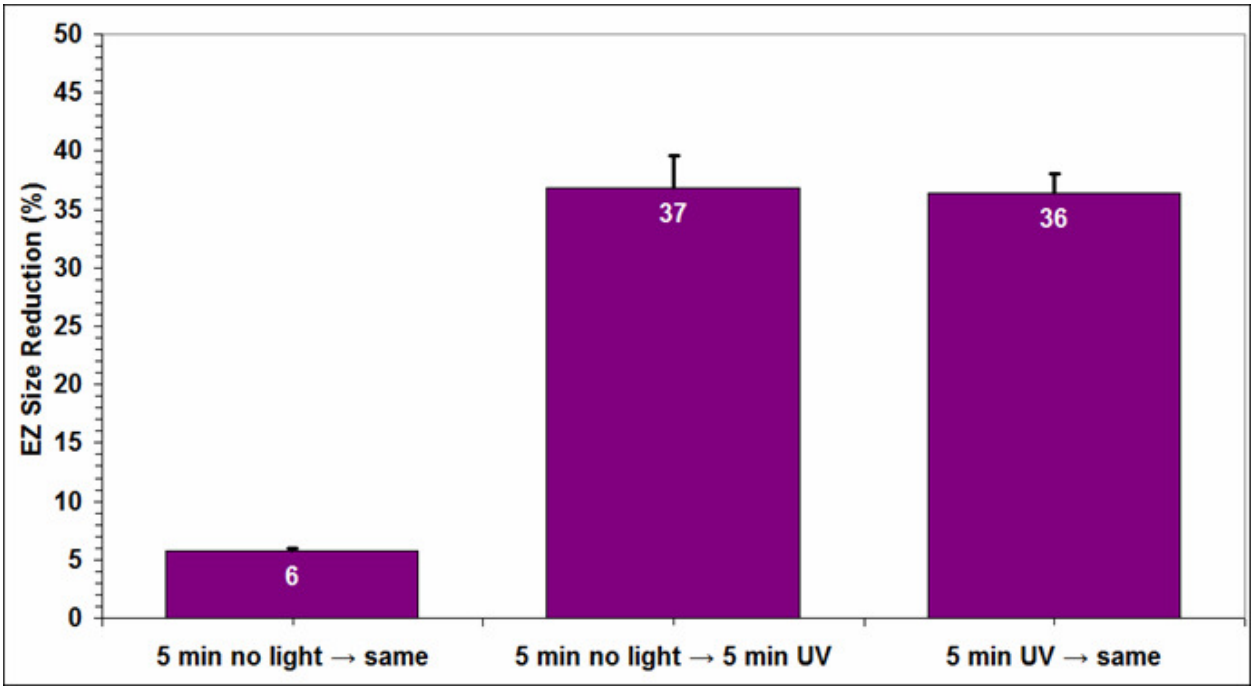

b

Figure 41: Decrease of exclusion zone size with the application of UV light. a) Blue bars are exclusion zone sizes at 5 min, orange bars are sizes at 10 min under the following conditions: no light for 5 min, UV light for 5 min and UV light throughout the entire 10 min experiment. b) Percent decrease of the exclusion zone for each of the three conditions.

Although the total effects of UV light on the exclusion zone and its mechanism are beyond the scope of this thesis, initial results demonstrated that exclusion zone sizes decreased with UV exposure, while corresponding proton-rich regions in bulk water increased in thickness. Considering exclusion zone observations, one would expect that the proton-rich region would decrease in thickness along with the reduction in the exclusion zone size, but the reverse was seen. This was a surprising finding, since the wavelength of UV light employed is a radiation least absorbed by bulk water. One possible explanation is that UV light may generate free radicals in the bulk water which may cause the further production of protons and hydronium ions in solution. These free radicals may also destroy, or reduce exclusion zones at the Nafion surface, similar to how free radicals produced by UV light harm biological systems.

2.9. Electrical potential measurements and spectroscopy

The electrical potential of the exclusion zone has already been measured and characterized in previous investigations[105-106], therefore experimental details and methodologies will not be covered here. Briefly, when a glass microelectrode typically used in electrophysiological measurements was translated from the bulk water region and through the exclusion zone (**figure 42a**), measurements demonstrated that the exclusion zone possessed a negative electrical potential relative to a distant reference electrode located in the bulk water (**figure 42b**). Immediately adjacent to the Nafion surface, electrical potentials measured nearly -150 mV.

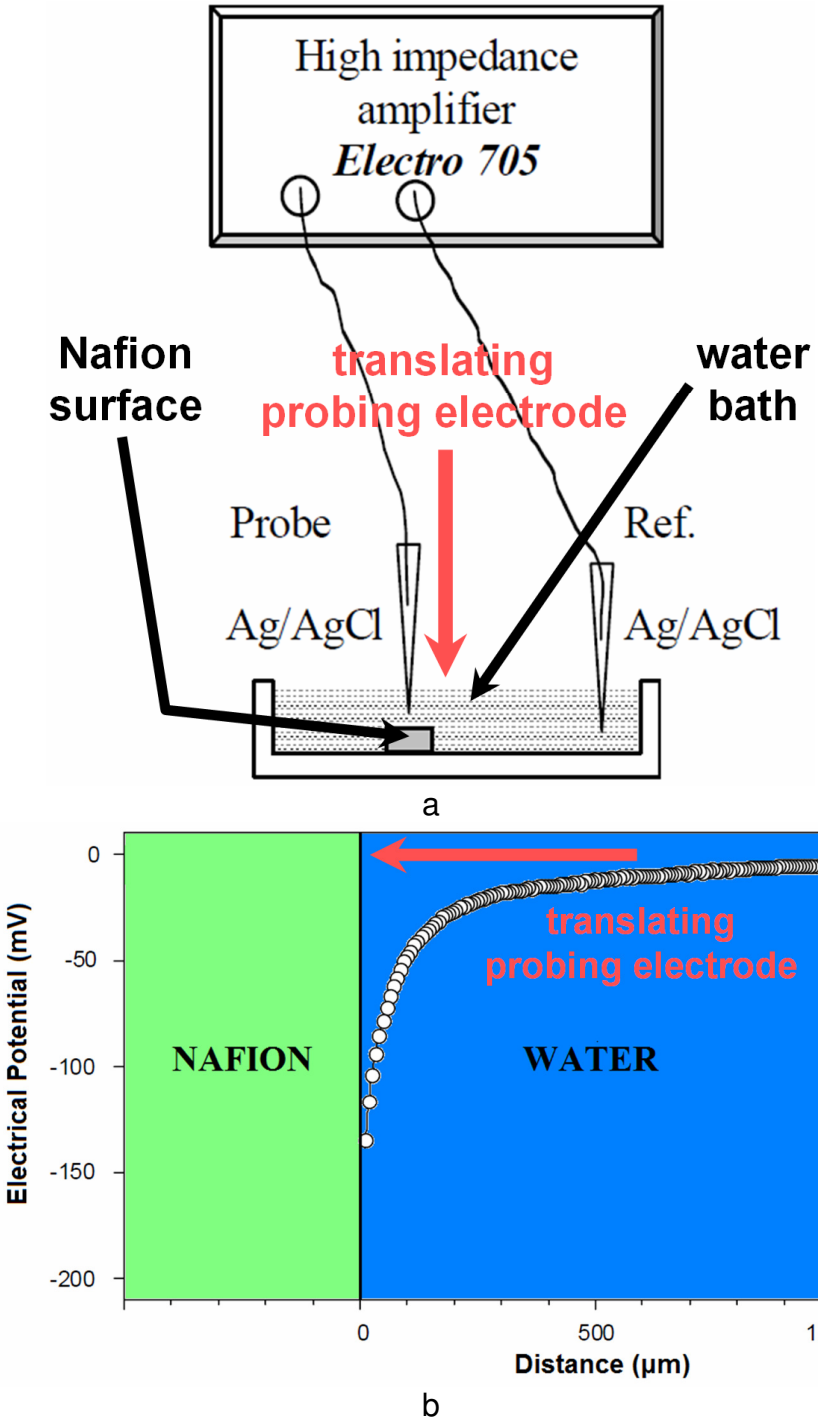

Figure 42: Electrical potential measurements of the exclusion zone. a) A probing glass microelectrode was translated towards the surface of a Nafion block and recorded the electrical potential difference relative to a distant reference electrode placed in the bulk water solution. b) The electrical potential distribution of the exclusion zone was negative and extended nearly 1000 µm from the Nafion surface.

UV-vis spectroscopy was also performed on the exclusion zone water adjacent to a Nafion surface. Information on the exact experimental details can be reviewed in an earlier study[108], but findings demonstrated that the exclusion zone has a unique spectral absorption profile with a signature absorption peak at 270 nm (**figure 43**).

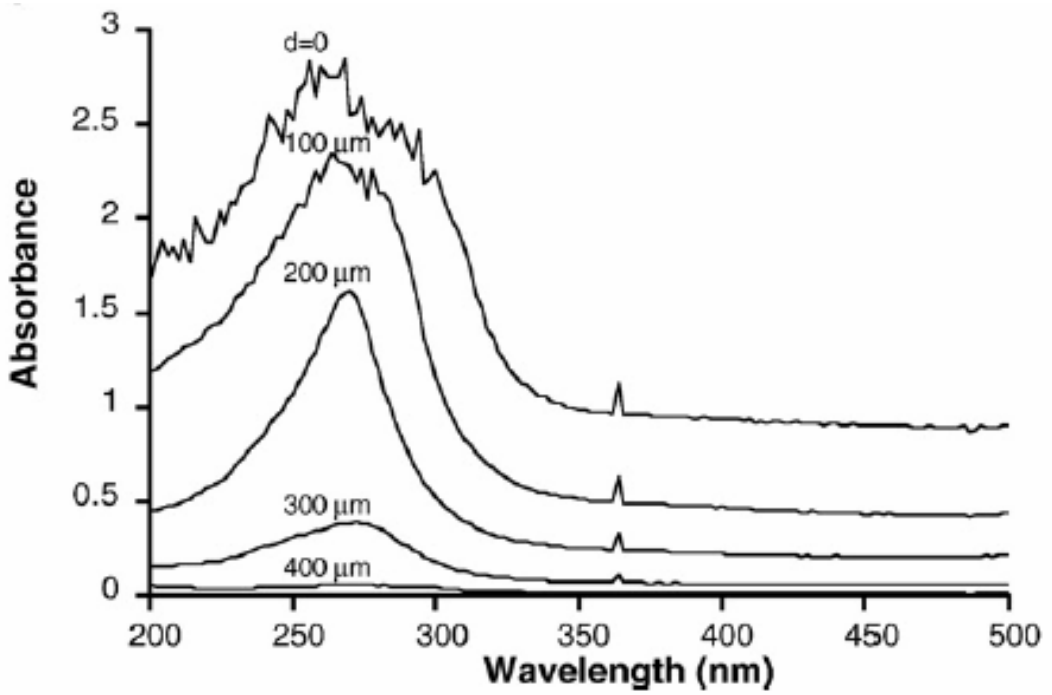

Figure 43: UV-vis absorption spectrum of the exclusion zone adjacent to a Nafion sheet. Peak absorption of the exclusion zone was found at 270 nm. The spectral response of the exclusion zone was maintained through the region and up to nearly 500 µm from the Nafion surface.

2.9.1. IR properties

IR imaging of the exclusion zone has been studied in the past[106], but measurements were repeated here for vertically-oriented Nafion tubes so as to gauge the exclusion zone's properties within this particular chamber and setup. A forward-looking IR camera (Camera, FLIR SC6000 4.1, λ = 3-5 µm; IR Lens, Janos Technology, Model #40494-

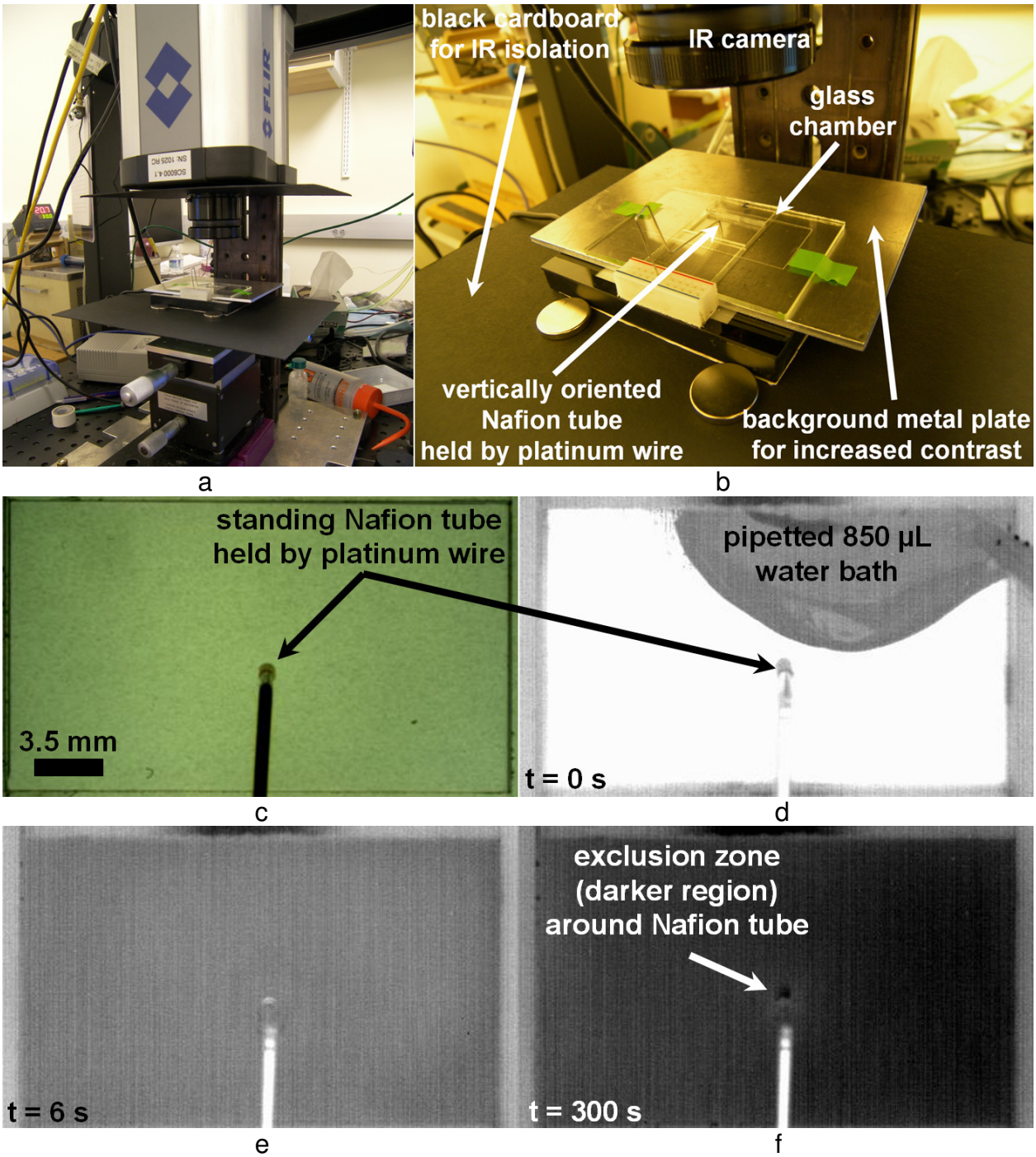

Figure 44: IR imaging of the exclusion zone. a) Overall macroscopic setup from far away. b) Close-up perspective of a. c) Camera image of experimental area. d-f) IR gray scale image of c as a water bath was pipetted in. The region adjacent to the Nafion tube (the exclusion zone) is much darker than the surrounding, homogeneous bulk water environment. Control experiments were conducted when a Nafion tube was absent and just the "L"-bent tube holder was present in the water bath.

0484) was used to record movies (**figure 44a-b**) of the environment around the Nafion tube as a water bath was added to the chamber (**figure 44d-f**).

A control experiment was carried out when just a platinum wire was present (**figure 45a**). Gray scale values of the movie recordings for both experiment and control were plotted in false color as a three-dimensional surface to better visualize the IR emission and difference when an exclusion zone was present (**figure 45b**). IR movie recordings demonstrated that while the bulk water maintained a homogeneous IR emission, the region around the Nafion surface was much darker in comparison to the same region when a Nafion tube was absent. See **figure 45** for details.

2.10. Miscellaneous observations and experiments

2.10.1. Nafion blocks and exclusion zone projections

Early on (**figure 27**), projections of the exclusion zone with microsphere suspensions were shown to grow and extend far into the bulk solution in several experiments. Although, this was also found in experiments using pH-dye, other microsphere-based observations will be presented here concerning this phenomenon.

After a Nafion block was cut to a dimension of 50 µm, the sample was then superglued to a small metal probe and a standard carboxylate microsphere suspension was washed into a chamber containing the Nafion block-attached probe (**figure 46**).

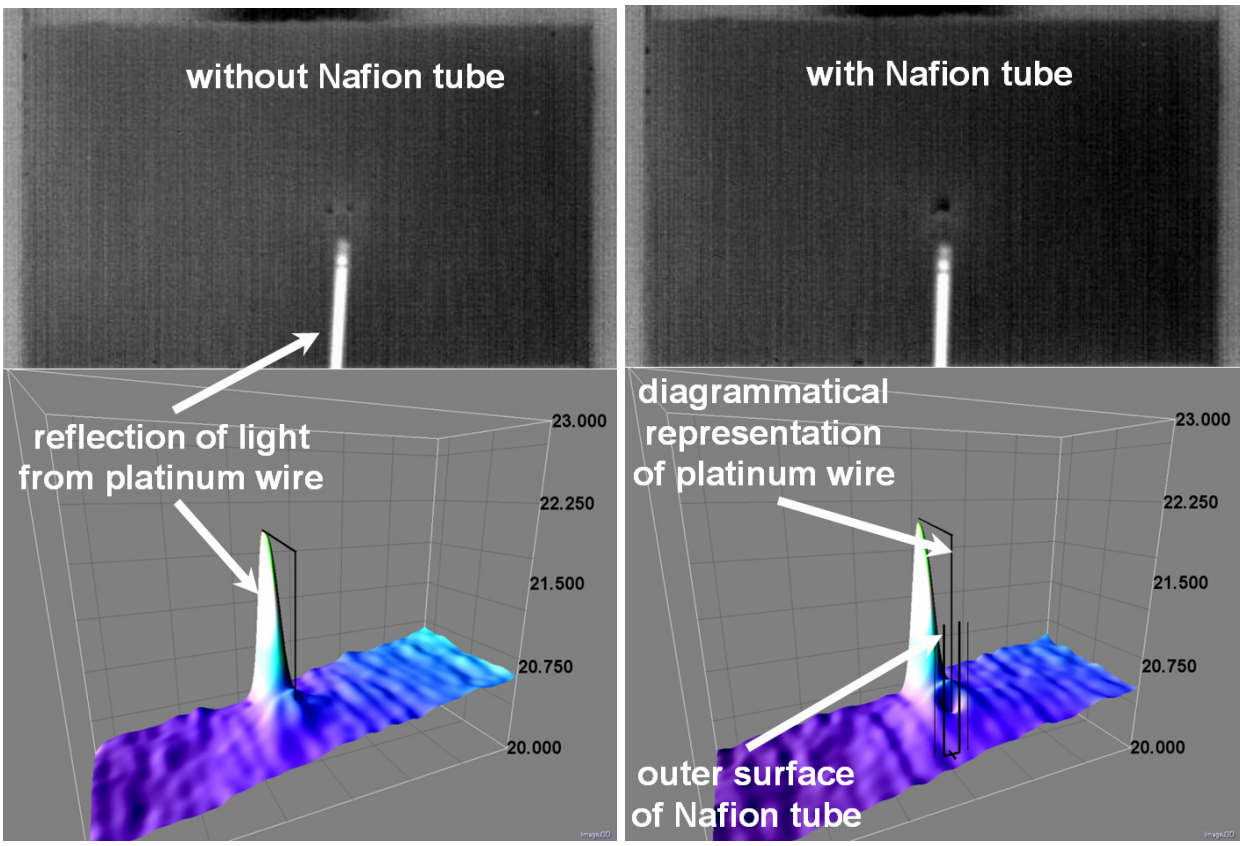

Figure 45: Comparison of IR images at the end of 10 min movie recordings when a Nafion tube was fitted onto the end of the platinum wire mechanical scaffold. a) The control experiment. Being metal, the platinum wire reflected a large portion of the IR light towards the camera (top) and was thus colored white. In the surface plot (bottom), this reflection was seen as a large peak in the middle of the false-color surface. The black "L"-shaped line represents (to scale) the "L"-bent platinum wire. b) The experiment with an attached Nafion tube. Because the xy-plane of the three-dimensional space represents distance, the outer diameter of the Nafion tube was indicated by the small crosshairs drawn at the bottom of the "L"-shaped line, so that the middle point of the crosshairs was aligned with the central axis of the Nafion tube. The thick vertical lines at the ends of the crosshairs represent the outer diameter of the Nafion tube. Thin vertical lines parallel to these lines were positioned so that they intersected the three-dimensional surface plot at the top of each "lip" of the volcano-like structure. The distance between the dark and light vertical lines was ~475 μm. This distance was comparable to the size of the exclusion zone. In the gray scale video, this region was very black, implying that the region (the exclusion zone) had a lower emissivity than the surrounding bulk water. In previous work, it was concluded that lower emissivity reflected the highly-ordered water within the exclusion zone[106]. Results here are thus consistent with previous findings.

After a stable exclusion zone formed (**figure 46a**), the probe with the attached Nafion block was slowly translated in a path that followed an upside-down "U", or horseshoe pattern. The results were dramatic. The exclusion zone was observed to stretch into a projection that was not only greater than 2 mm, but the projected region had virtually no microsphere concentrations (**figure 46d**).

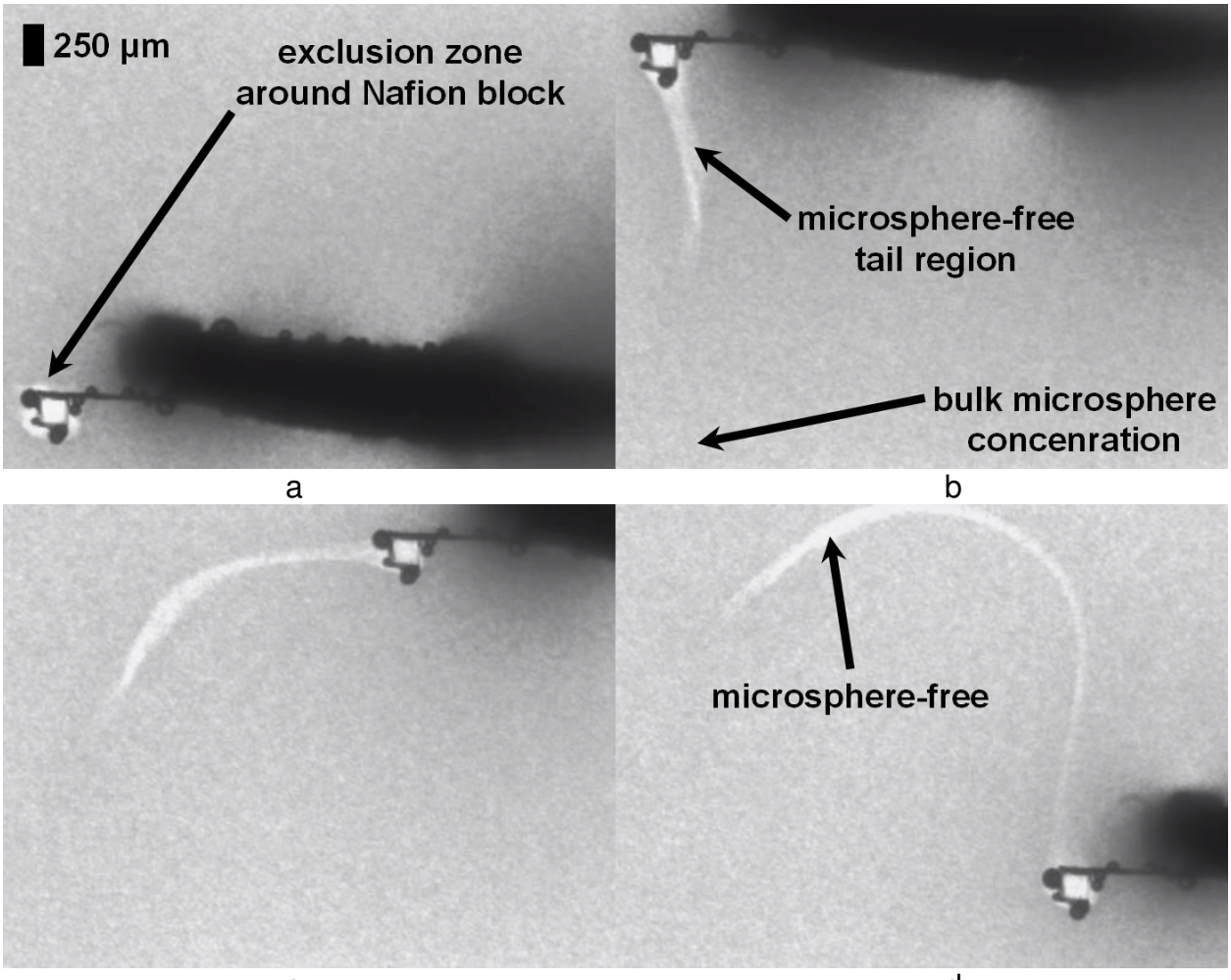

Figure 46: Pulling an exclusion zone into a projection. The projection was microsphere-free and extensive. In the above experiment, the extensive projection was maintained for nearly 10-15 min.

In another experiment, the Nafion block was making contact with a Nafion tube. After a stable exclusion zone formed, the block was pulled away and the corresponding

exclusion zone projection was used to write the first initial of the author's name (**figure 47i**). The projection was similarly extensive and the concentration of microspheres within the region was nearly two times less than the bulk suspension. Measurements were accomplished by simply comparing the averaged gray scale intensity area of a given projection region to an area located in the bulk microsphere suspension.

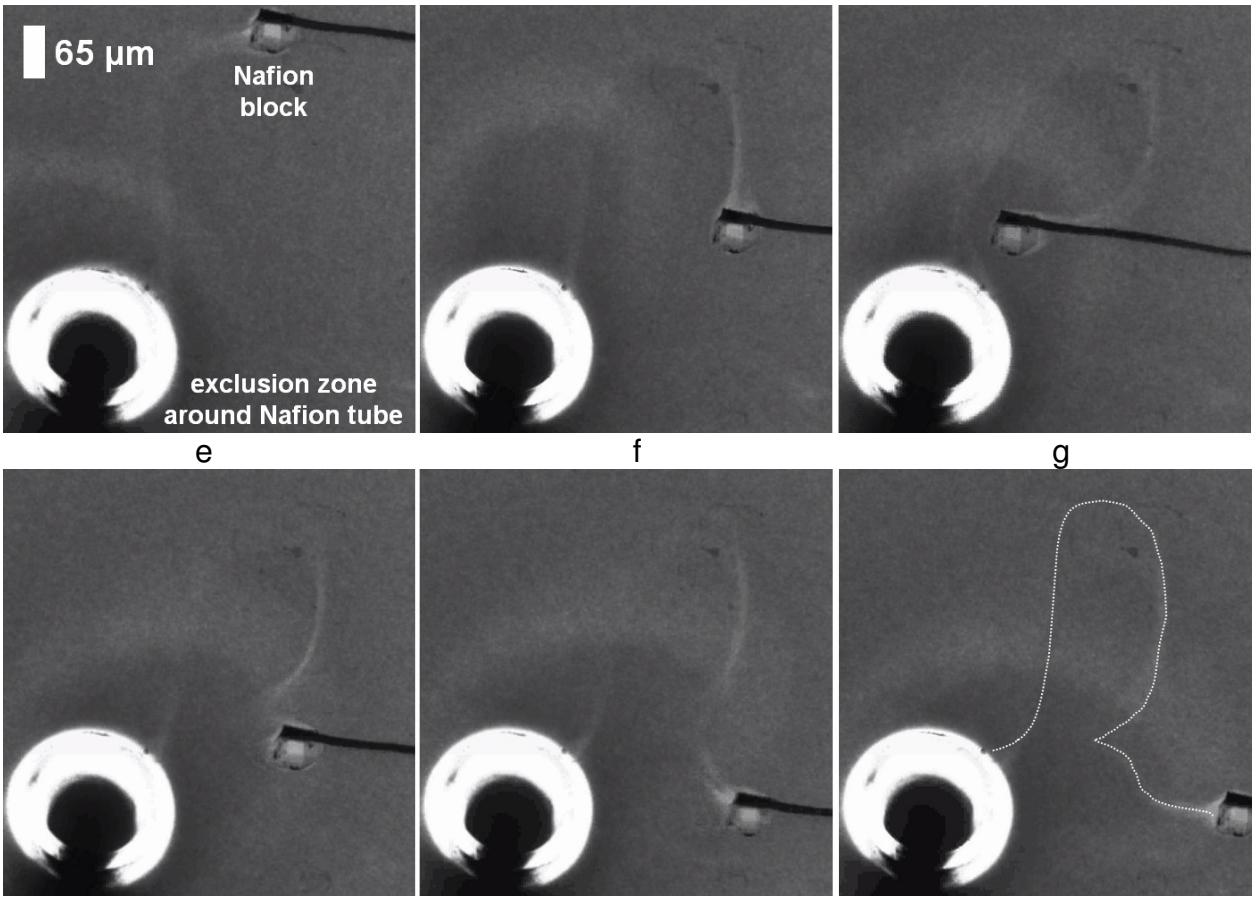

Figure 47: Writing the first initial of the author's name with a projection of the exclusion zone. The "R"-shaped projection was 1500 µm in length and persisted in shape for about 10 min.

Although the hypothesized mechanism behind the exclusion zone is covered later in the dissertation, charge separation and the water bound to the Nafion's molecular structure are thought to be responsible for such projections of the exclusion zone.

Water at the Nafion surface exhibits mechanical properties distinct from bulk water[114-116], therefore mechanical disruption, or mechanical pulling of this interfacial water is considered a possibility since the water is ice-like. For example, imagine hair-gel in a chamber filled with water: while the gel is a different phase of matter from the liquid water, a probe can pick at the hair-gel and pull projections into the bulk water while the gel maintains a continuous, mechanical structure. Therefore, is this mechanical structure of the projections simply stabilized by the electric field between the protons and the negatively charged exclusion zone projections?

It is hypothesized (also discussed later in the dissertation) that protons do not diffuse into the exclusion zone since its molecular structure is unique. However, this can only be accomplished when the zone is adjacent to a charged, hydrophilic surface. Therefore, a remaining issue is how the exclusion zone very far from the nucleating surface can be maintained. In the previous experiments, after 15-20 min, microspheres eventually invaded the exclusion zone projections, thus it is possible that protons diffused into the exclusion zone and eventually neutralized the region. Nevertheless, until this diffusion occurs, how are the projections maintained for those initial 10-15 min time periods?

Although conjecture, if charges are fixed within the exclusion zone's molecular structure, then pulling this structure alters the charge density of the projections. Hence, projections near the Nafion surface have a greater negative electrical potential than further regions. Also, further projected exclusion zones most likely have a weaker

ordering of water than zones closer to the hydrophilic surface. A simple test of this hypothesis would be to pull the exclusion zone from a Nafion surface into a linear projection and verify that diffusion of microspheres into distal regions is faster than proximal regions. A follow-up study could be performed using pH-dye.

2.10.2. Properties of Nafion

All of the work presented in this dissertation uses the polymer Nafion. Aside from robust, stable exclusion zone formation at the surface of the polymer, Nafion itself also has many interesting properties that will be briefly addressed.

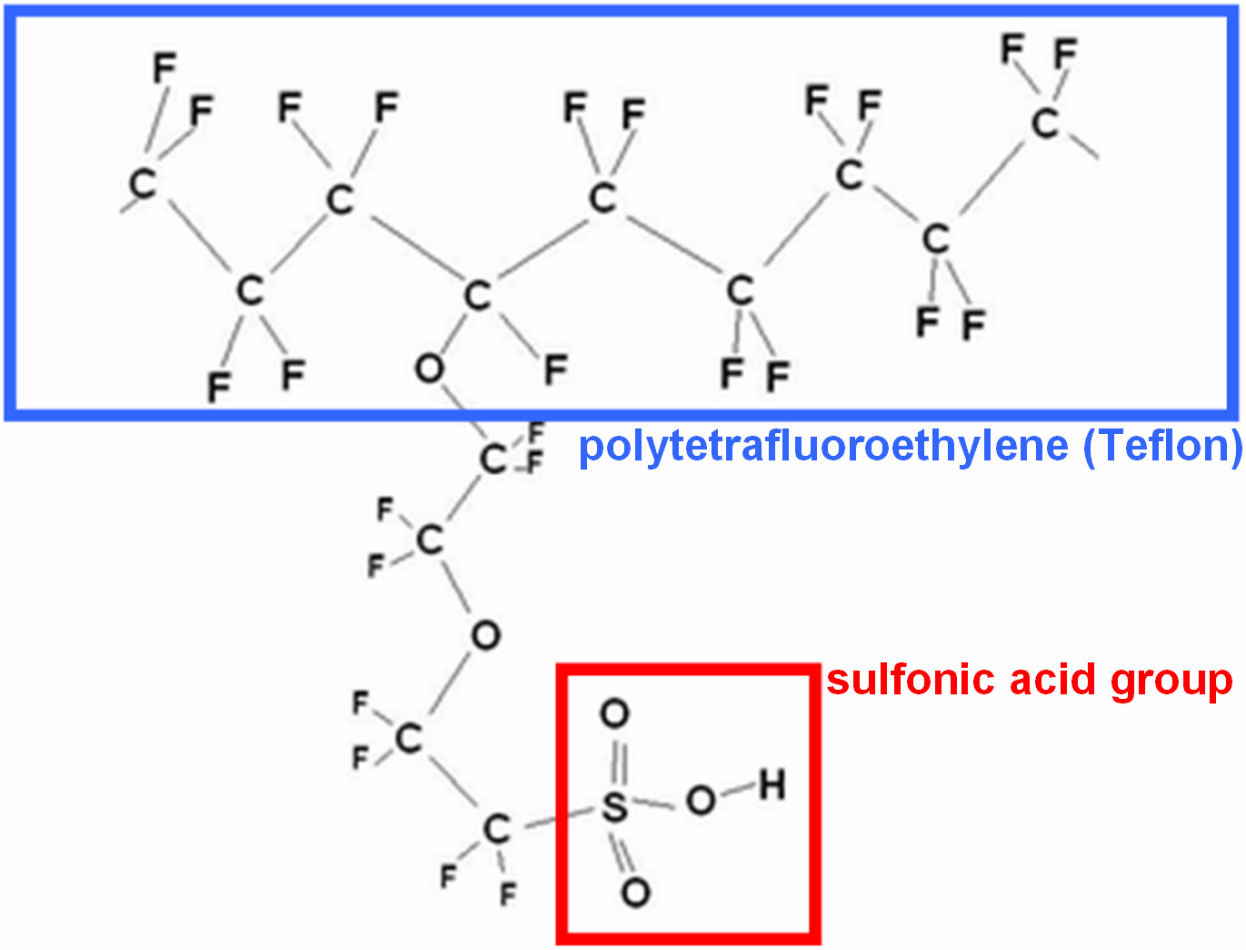

Figure 48: Molecular structure of Nafion.

Nafion was discovered by accident in the late 1960s by Walther Grot, who worked for DuPont. As a material, Nafion is ideal for modeling proteins since its molecular structure (**figure 48**) is both hydrophobic and hydrophilic (**figure 48-49**). Nafion consists of (hydrophilic) sulfonic acid groups, which project like branches from the (hydrophobic) polytetrafluoroethylene (Teflon) molecular backbone. Because of these groups, Nafion is also a proton conductor[114], which is similar to protein-like structures that interact with aqueous environments through pH- (and proton-) mediated processes.

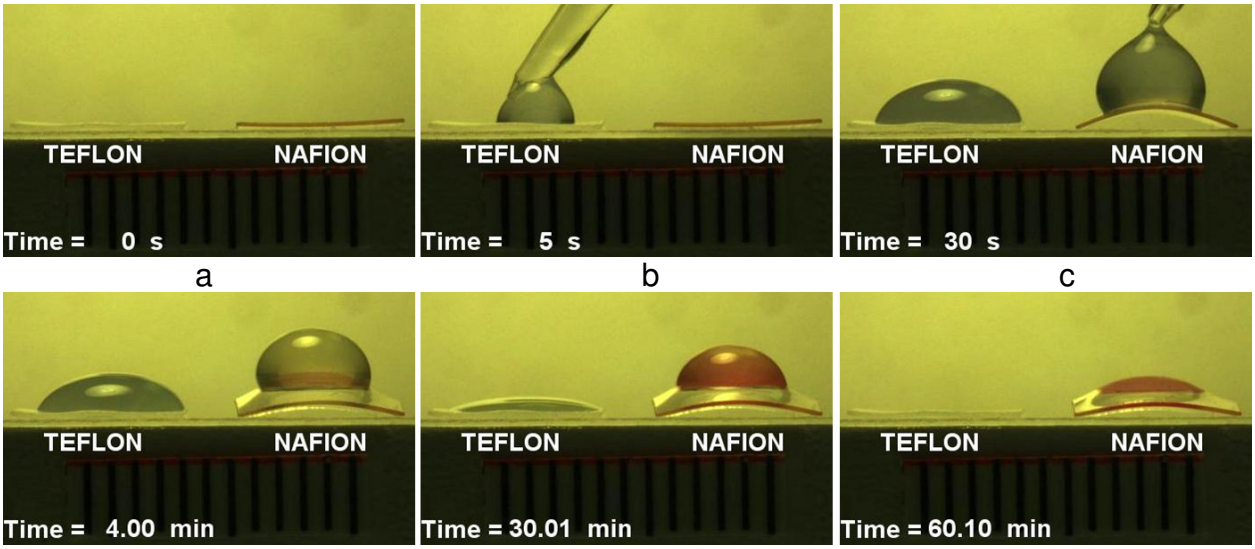

Figure 49: Nafion contact angle experiments. a-b) A drop of water with pH-dye is pipetted onto a Teflon and Nafion sheet. c) Because Nafion is both hydrophobic and hydrophilic, the drop on the polymer has a similar contact angle to the drop on Teflon. The Nafion sheet itself also buckles and bows because it is being hydrated on one side. If more water was added, then the Nafion sheet would completely hydrate, and the membrane and water drop would flatten out. The corresponding contact angle of the water drop would then be nearly 0 deg. d-f) After a drop was added to each sheet, evaporation of the water drop from Teflon took about 45 min, while the same volume of water remained bound to the Nafion membrane for nearly an hour. Even after evaporation, the Nafion membrane still maintained a bow shape. Eventually the polymer flattened out due to the evaporation of the bound, hydrated water within the Nafion polymer matrix. Note the color change of the pH-dye in the water drop over the longer time periods. pH-dye indicates that the bulk water within the drop becomes more acidic, or proton-rich (denoted by the red color).

Another feature of Nafion is its incredible ability to hydrate and quickly absorb water. By weight, Nafion absorbs at least 20% water (**figure 50**)[114-116]. With a density of nearly

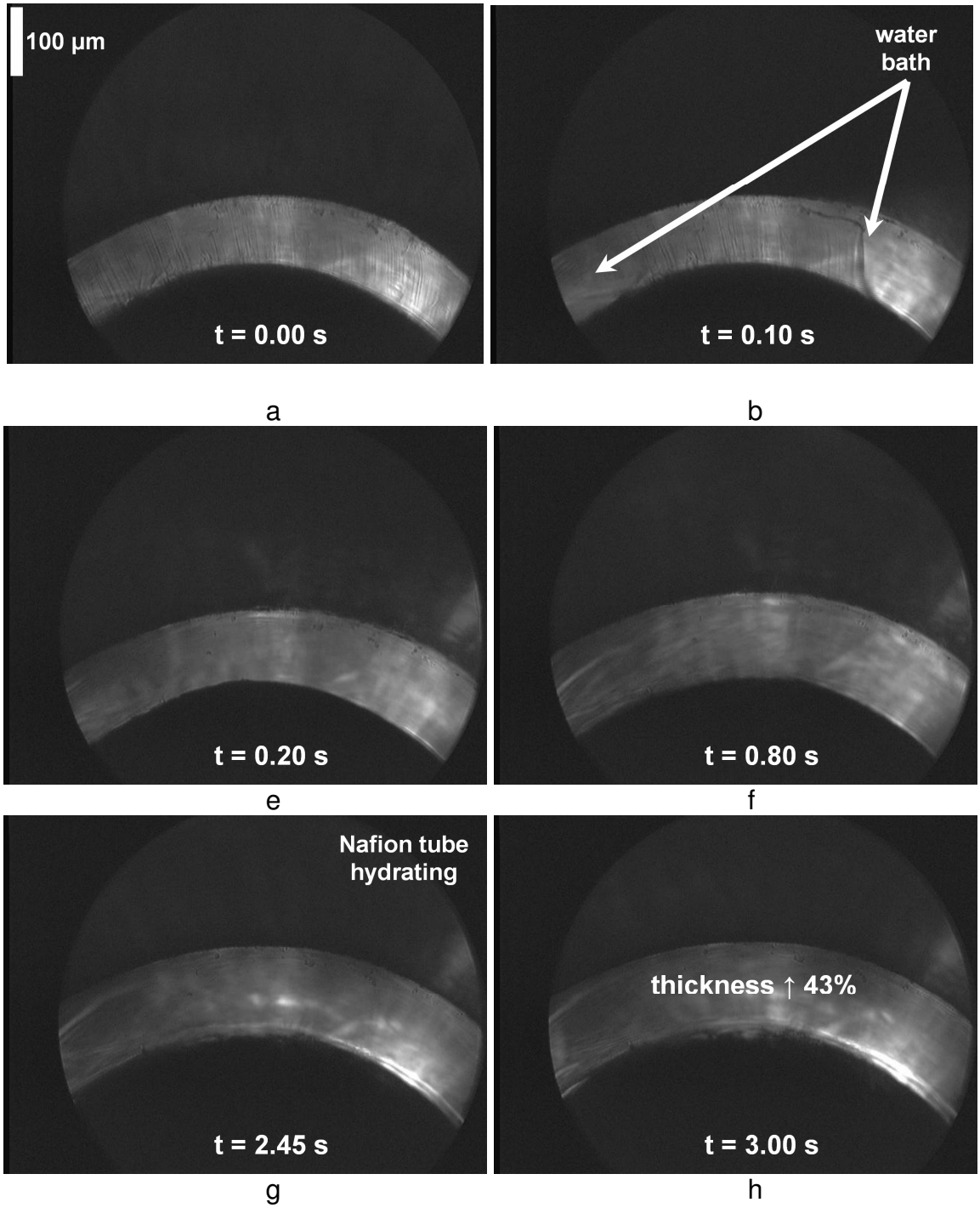

Figure 50: A hydrating Nafion tube. a-h) Water was added to a chamber with a standing Nafion tube. Note between b and e how the incoming water bath causes an initial expansion of the Nafion tube in those regions making contact with the liquid.

twice that of water (1.91 g/cm^3), Nafion tubes were measured before (**figure 50a**) and after (**figure 50b-h**) they were immersed in a water bath. In under 5 s, Nafion tubes hydrated and expanded, such that their wall thickness and height increased by nearly 45% and 10%, respectively. This corresponded to a 70% increase in volume and a 40% absorption of water by weight.

2.11. A brief summary

Long-range water ordering was visualized in the formation of the exclusion zone. Using a simple microsphere suspension and a Nafion surface (**figure 20-21**), exclusion zones were seen through microsphere-free regions adjacent to the polymer and are the most widely-recognized feature of the phenomenon. Measured on the order of 100-300 μm (**figure 20-21, 24**), exclusion zones have been found at many different kinds of surfaces using a diverse range of microparticles and indicators (**figure 28**). While IR properties of the exclusion zone (**figure 44**) demonstrated a more ordered phase of water occupying the region, UV-vis spectroscopy found that exclusion zones characteristically absorbed light at a signature peak of 270 nm (**figure 43**).

The unique water ordering was reflected in not just mechanical, but also electrical properties. Microspheres were not only excluded from Nafion surfaces, but were also done so in experiments where the surface was oriented against gravity, implying that a force exists at the interface (**figure 30**). Similarly, projections of exclusion zones and connections between corresponding zones have shown gel-like, viscous type behavior

(**figure 27**, **29**, **46-47**). Electrically, exclusion zones seemed to be readily influenced by applied electric fields and collapsed when a voltage was applied across the entire region (**figure 36**). Salt additionally reduced zone size, but did not eliminate exclusion zones altogether, even in solutions containing high salt concentrations (**figure 37**).

Nonetheless, the most revealing evidence for the mechanism behind the exclusion zone was found in pH-dye and electrical potential measurements (**figure 24**, **42**). While pH-dye turned to a red color (denoting the presence of protons) in regions beyond the exclusion zone's periphery, electrical potential measurements characterized the exclusion zone as being negatively charged. Therefore, it is possible that exclusion zones may be based upon the separation of charge, which occurs between the interfacial negative region adjacent to the hydrophilic Nafion surface and the farther positively charged bulk water zones. Consequently, there may exist a significant electrostatic force between these two regions and is thus explored in the main objective of this dissertation.

Chapter 3: Hypothesis and specific aims

3.1. Hypothesis

We hypothesize that separation of charge at the exclusion zone (EZ) may produce a significant electrostatic force between the exclusion zone and the bulk water proton-enriched zone (PEZ) beyond. Here we describe the testing of our hypothesis by measuring the underwater deflection of a ribbon-like beam sensor bearing a Nafion sample in the form of a Nafion tube.

3.2. Specific aims

Specific aim #1

Establish that charge separation occurs at the Nafion-water interface between the EZ and the PEZ.

Specific aim #2

Determine the magnitude of electrostatic attraction between the EZ and the PEZ.

Chapter 4: Specific aim #1

4.1. pH-dye experiments

To measure the proton distribution in the bulk water beyond the exclusion zone, universal pH-sensitive dye was added 1:50 v/v to 850 µL of ultrapure water; the solution was then pipetted into a glass chamber containing a 500 µm long Nafion tube (PermaPure, LLC, Nafion tube, Model #TT-030, nominal outer diameter = 840 µm). The experiment was recorded via digital camera at 1 fps.

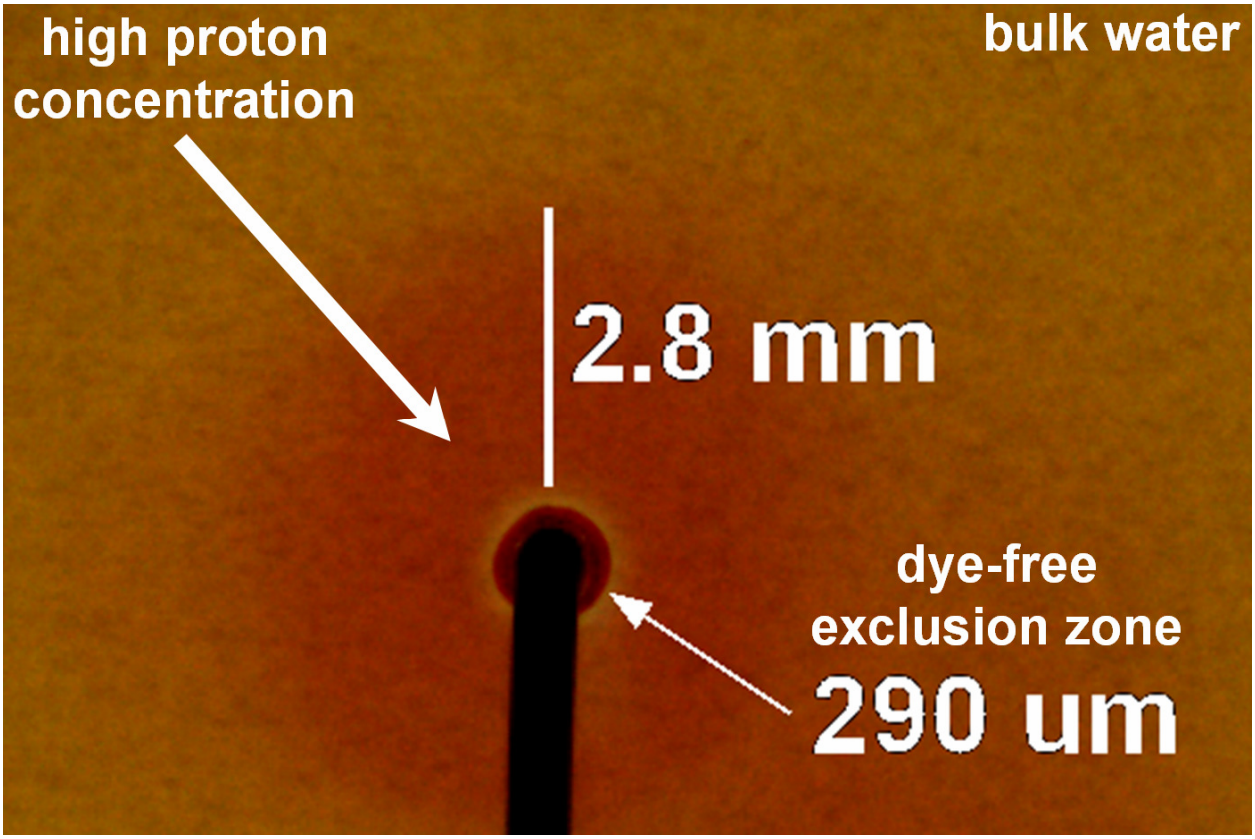

Figure 51: pH-dye distributions. Movie image at 5 min, after pH-dye was pipetted into the chamber. An exclusion zone (~300 µm thick) is seen here as a clear, yellow-white ring (see arrowhead) around the Nafion tube. In the bulk water, a high concentration of protons (denoted by the red color) was observed.

Within seconds after adding water with pH-dye to the chamber containing the Nafion sample held by the platinum wire, a dye-free exclusion zone of ~200 µm formed at the tube surface. This was similar to previous studies where microsphere-free regions were observed when microsphere suspensions were used (**figure 20-21**). pH-dye in the bulk water immediately turned red, denoting a low pH and a high concentration of protons. Over 5 min (**figure 51**), the exclusion zone had grown and remained constant at approximately 300 µm, while the proton-rich region beyond the zone was approximately 10 times thicker and continued to grow into the surrounding bulk water.

4.2. Electrical potential experiments

In order to measure the electrical potential difference between the exclusion zone and bulk water, several modifications were made to the setup described above. First, the platinum wire that originally served as a scaffold was now doubled as a probing electrode. And second, an additional platinum wire acting as a reference electrode was placed in the bulk water beyond the exclusion zone. The two electrodes, one enveloped by the Nafion tube, were then similarly immersed in 850 µL of ultrapure water without pH-dye. Electrical potential difference was measured after 15 min between the probing electrode, whose Nafion tube generated an annular exclusion zone along its outer surface, and the reference located in the bulk water (**figure 52**). Measurements were made as the electrode separation distance was varied. Control experiments consisted of measuring the electrical potential difference between the electrodes when

the Nafion tube was replaced with hydrophobic tubes (Teflon and Tygon) and when a tube was absent altogether. At each separation distance, measured control data were subtracted from experimental data and results were subsequently plotted.

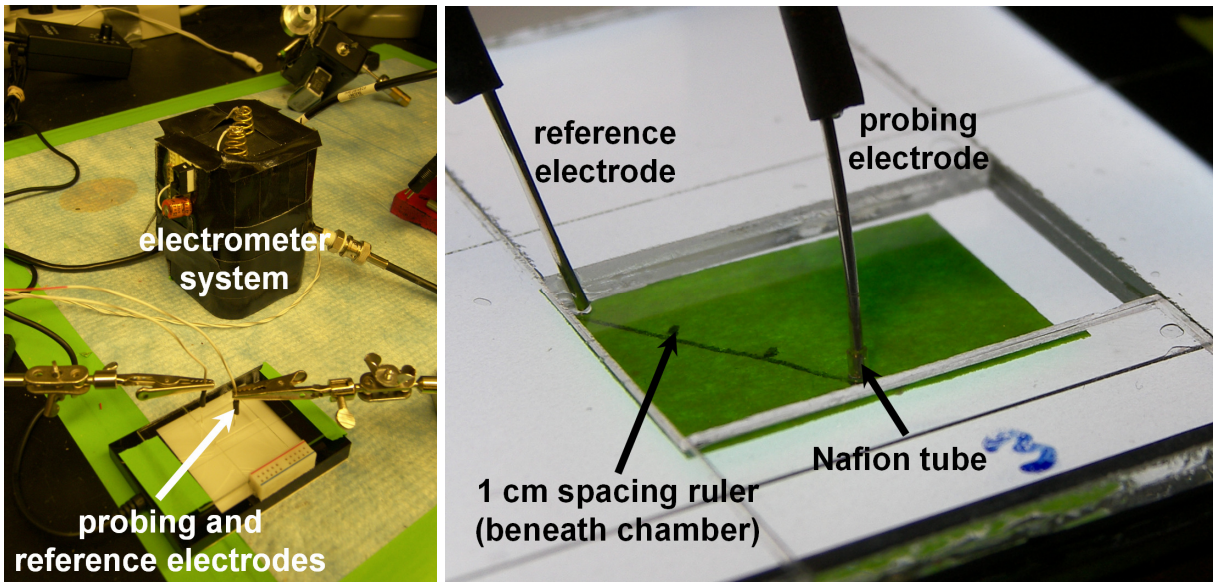

a b

Figure 52: Electrical potential difference measurement setup. a) The custom-designed electrometer system. b) The actual setup sitting on top of the illumination platform. A ruler was drawn on a piece of lab tape which was stuck to the platform, but beneath the glass chamber. Electrical potential difference was measured between the probing and reference electrodes. The probing electrode was covered with a Nafion sleeve that produced an exclusion zone.

The electrical potential difference was measured by connecting the platinum electrodes to a high input impedance amplifier (Analog Devices, Inc.). The amplifier was DC-powered and low-pass filtered, which eliminated power line and unwanted noise. Voltages were recorded using LabVIEW hardware and software, and analyzed offline in MATLAB using custom-written analysis programs.

In the voltage measurement configuration, the platinum wire inserted snugly into the Nafion tube was used as a probing electrode, while a similar wire was placed in the bulk

water as a reference electrode. The electrical potential difference between the wires was measured as a function of the distance between the wires. Relative to control experiments, the electrical potential difference was negative and increased in magnitude as the distance between the wires was increased (**figure 53**). Measured differences were similar at large separation distances and is visualized in **figure 53** within the plateau region between 20 and 30 mm. When electrodes were brought as close together, separated only by the Nafion tube, the voltage was still slightly negative, most likely due to the thin exclusion zone layer between the Nafion tube's outer surface and the reference electrode.

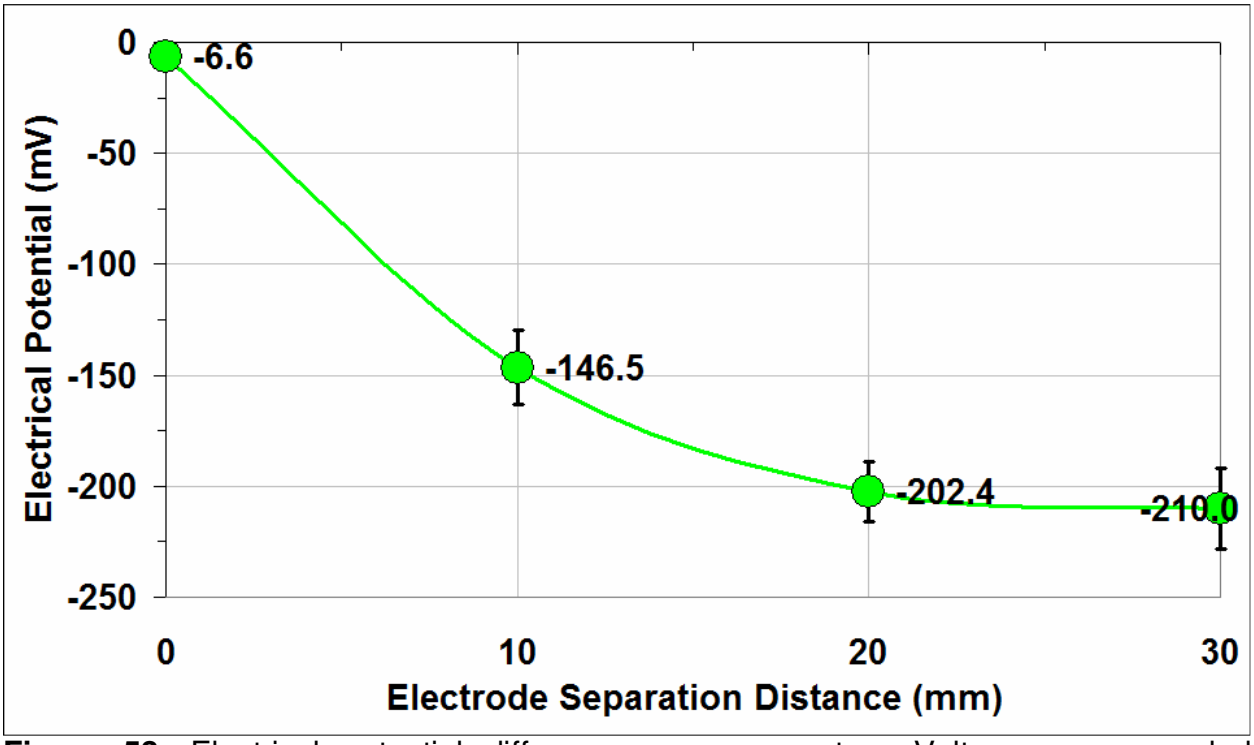

Figure 53: Electrical potential difference measurements. Voltage was recorded between platinum wires (one with a Nafion tube) as their separation distance increased. The exclusion zone demonstrated a consistent negative electrical potential relative to the surrounding bulk water. The voltage levels out at further distances (20-30 mm) from the Nafion tube. The absolute magnitudes of the measured voltages are comparable to the electrical potentials measured in figure 42 using glass microelectrodes. Each datapoint here represents the average of 5 controls (Nafion tube absent, just water) subtracted from their individual experiments (Nafion tube present). The plotted error is one standard deviation of the data.

4.3. Discussion

pH-dye distributions demonstrated a low pH ~2.3 region beyond the exclusion zone that was 10 times thicker than the size of the exclusion zone and continued to grow over time. Although the experiment characterized pH distributions, exclusion zones were dye-free, thus pH measurement of only one zone (the PEZ) was achieved.

Exclusion zones are known to be regions of negative charge, thus electrical potential measurements should decrease with distance from this region. However, the results in these experiments showed the reverse. Voltage magnitude increased because the measurement reflected the contribution of not just one zone, but two: the EZ and PEZ (**figure 54**).

If the negative charges are fixed within the exclusion zone, then the negative electrical potential distribution from the EZ to the bulk water should also be fixed. Therefore, as the reference electrode was moved to further distances, the electrode reflected the contribution of the positively charged PEZ. Hence, the region should have a positive electrical potential distribution that begins somewhere in the bulk water and decreases in magnitude towards the EZ periphery. Consequently, the voltage measured between the probing electrode (which reflected the negative electrical potential of the EZ) and the reference electrode (which reflected the positive electrical potential of the PEZ) resulted in a magnitude of voltage which increased with distance and confirmed our hypothesis.

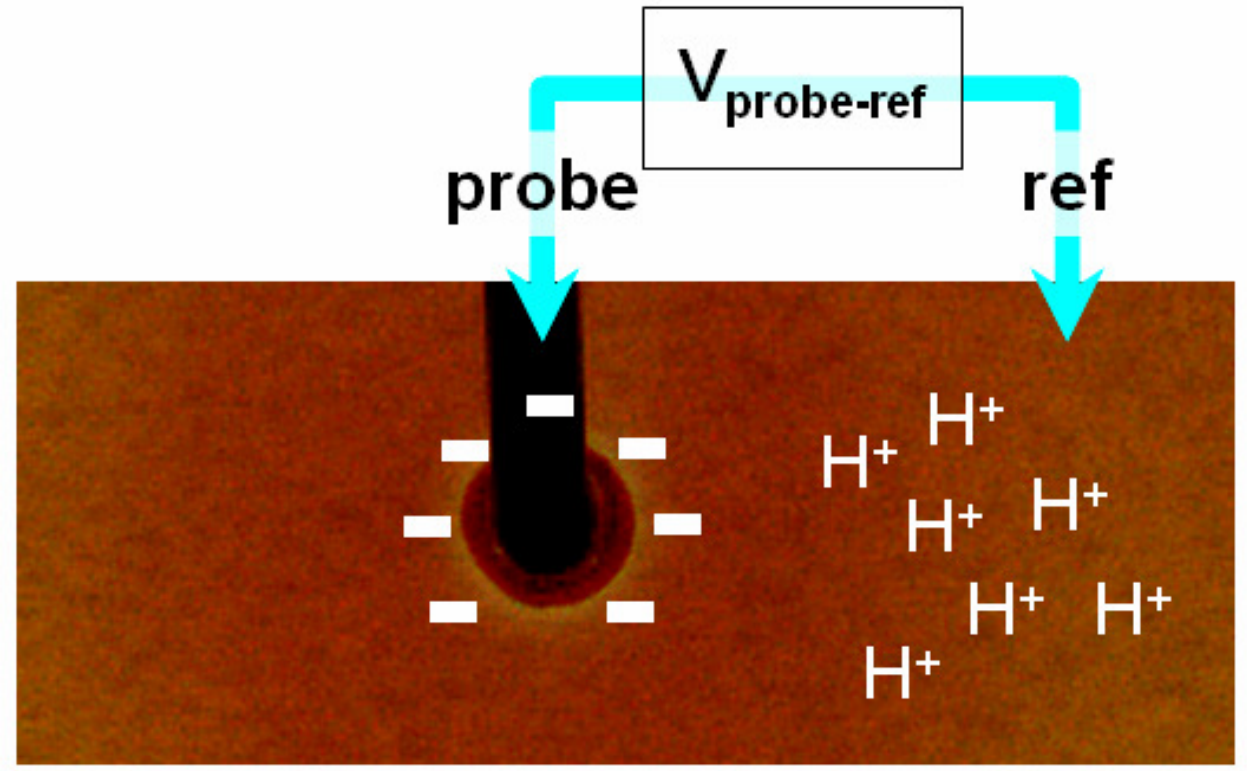

Figure 54: Diagram of combined pH-dye and electrical potential measurements.

One subtle feature of the results is diffusion. Proton diffusion is assumed to be fast, much faster than what pH-dye distributions revealed with red color. The reason why pH-dye indicates such slow diffusion is most likely due to the fact that the large pH-dye indicator molecules diffuse much slower than the protons themselves. Thus, while one dye molecule indicates the presence of a proton (or low pH) by red color, the diffusion rate of the population of protons is not accurately captured by the pH-dye.

Nevertheless, a consequence of proton diffusion is that while the proton concentration at the EZ periphery is high during the initial formation of the zone, after 15 min, the bulk water beyond should have a homogeneous proton concentration and distribution. Therefore, voltage measurements after 1 mm (**figure 42**) should

top off and remain constant at 10, 20 and 30 mm electrode separation distances. This was partially confirmed, since the electrical potential difference increased in magnitude from 0 to 20 mm and then was constant from 20 to 30 mm. The only logical explanation for such a gradual rise in the magnitude of the voltage is that the electrical potential of the EZ is much greater in amplitude and distribution than what was previously measured (**figure 42**).

Although microsphere-free and pH-dye free regions provide a measurement for the thickness of the EZ, the mere presence of these indicators may not reflect the true EZ size and hence, the true electrical potential distribution of the EZ. Electrical potential measurements using glass microelectrodes (**figure 42**) demonstrated that the EZ may extend as far as 1000 μm from the Nafion surface. However, glass microelectrodes are typically filled with a high concentration of KCl in order to make the measurement. It is therefore possible that while the system measured the EZ's electrical potential, leakage of the salt solution from the glass-pulled measurement electrode decreased the overall EZ size, as is known to occur with concentrated salt solutions (**figure 37**). Therefore, platinum electrodes, which are simple metal surfaces, may have more accurately revealed the extent of the EZ's electrical potential distribution. Based upon the measured data, the experiment implies that the negative electrical potential of the EZ may extend as far as several millimeters from the nucleating, hydrophilic Nafion surface. In support of such a claim, refer to the extensive EZs and the EZ projections, which are known to occur in experiments with microsphere suspensions as well as pH-dye (**figure 27**, **46-47**).

Chaper 5: Specific aim #2

5.1. Rationale

To test the hypothesis that electrostatic force exists between the EZ and PEZ (**figure 55**), we used the apparatus diagrammed in **figure 56**. A Nafion tube ~200 µm long was glued to the tip of a simple cantilever (**figure 56a**). The tube created an EZ with protons in the bulk water beyond. The ribbon-like cantilever was characterized with a high aspect ratio: the large face attached to the Nafion sample was as wide as the tube was tall (**figure 56b**). We hoped this feature would restrict most protons to one side of the cantilever. Hence if electrostatic attraction between the negative exclusion zone and the positive bulk was of significant magnitude, the Nafion tube-attached cantilever would bend away from its stiff reference beam, which could be measured optically.

5.2. Ribbon fabrication and mechanical sensor development

5.2.1. Silver wire flattening procedure

To develop a mechanical sensor with the required specifications, 75 µm diameter silver wire (A-M Systems, Inc., PFA-coated silver wire #785500) was obtained and flattened by a mechanical apparatus consisting of two rotating bearings (**figure 57**). Bearings were initially pushed together by hand to a point where further compression would

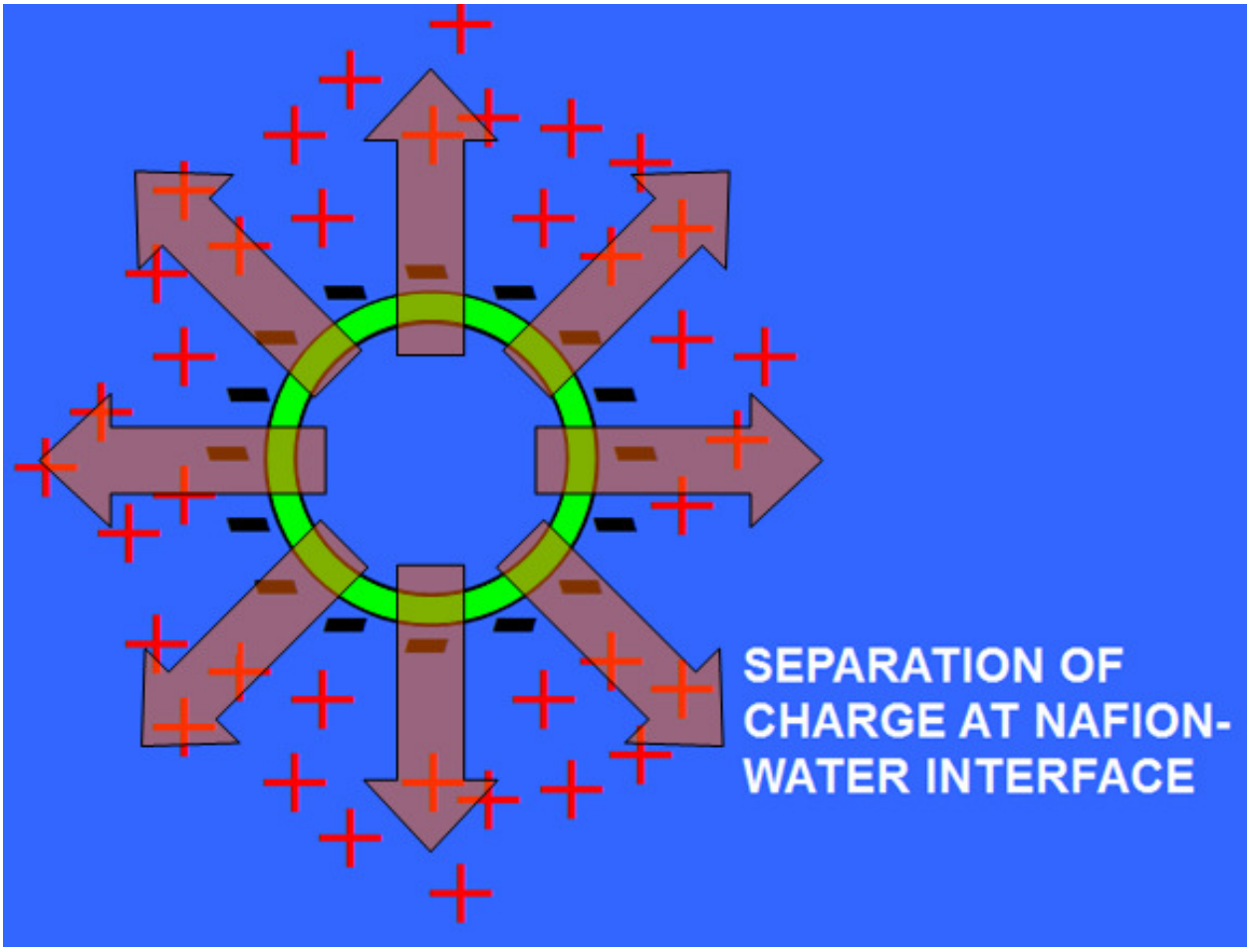

Figure 55: Hypothesized electrostatic force between the EZ and PEZ.

prevent one, or both bearings from freely rotating. Silver wire was then fed between the bearings as they were rotated by hand (**figure 58**).

Ribbon length was measured using a simple, digital caliper. Both ribbon width and thickness were measured through the microscope. In order to measure the thickness of a given sensor, the ribbon was bent into a "L"-shape and was then stood vertically on a slide that was positioned on the stage of the microscope. The edge-on (thickness) of the ribbon sensor was measured directly by the microscope objective at high magnification.

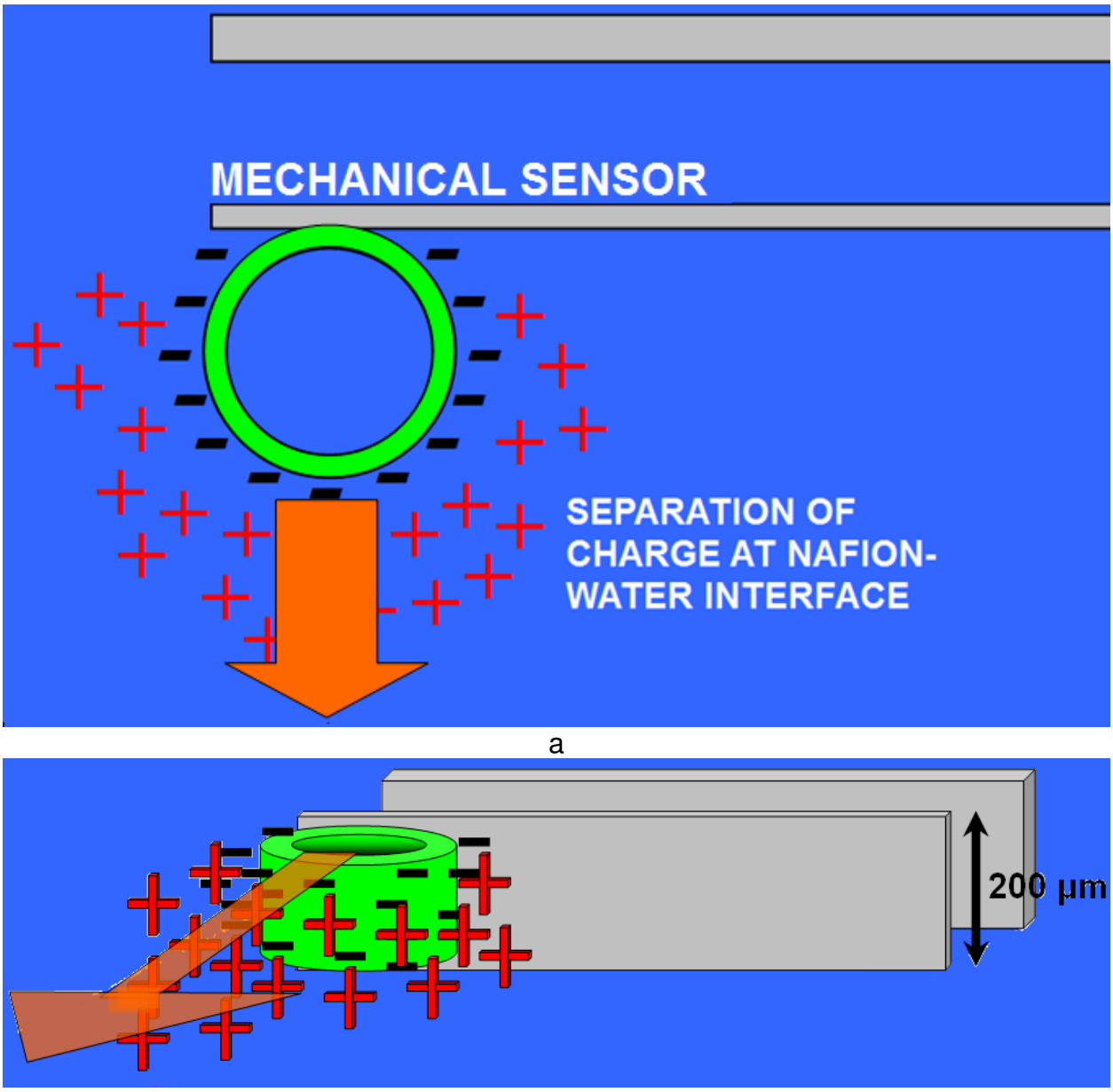

Figure 56: Electrostatic force measurement by a cantilever beam mechanical sensor. a) A Nafion tube attached to a cantilever beam would generate a negatively charged EZ with a corresponding PEZ in the bulk water beyond. b) Force would be measured optically through the microscope as the cantilever beam would deflect within a focal plane lateral to the chamber bottom. Success of the experiment depended on a critical feature of the experimental setup, that is if protons would be obstructed by the mechanical sensor on one side (a). This would result in unilateral electrostatic force development (orange arrow). Hence, it was essential that the cantilever beam mechanical sensor was wide as the Nafion tube was tall.

Nearly 80 ribbons were fabricated for experiments. Samples of ribbons were randomly selected for dimension measurements; an average and one standard deviation was calculated for several measurements ("measurement count") of either length, width, or thickness for a group of ribbons ("ribbon count") (**table 1**).

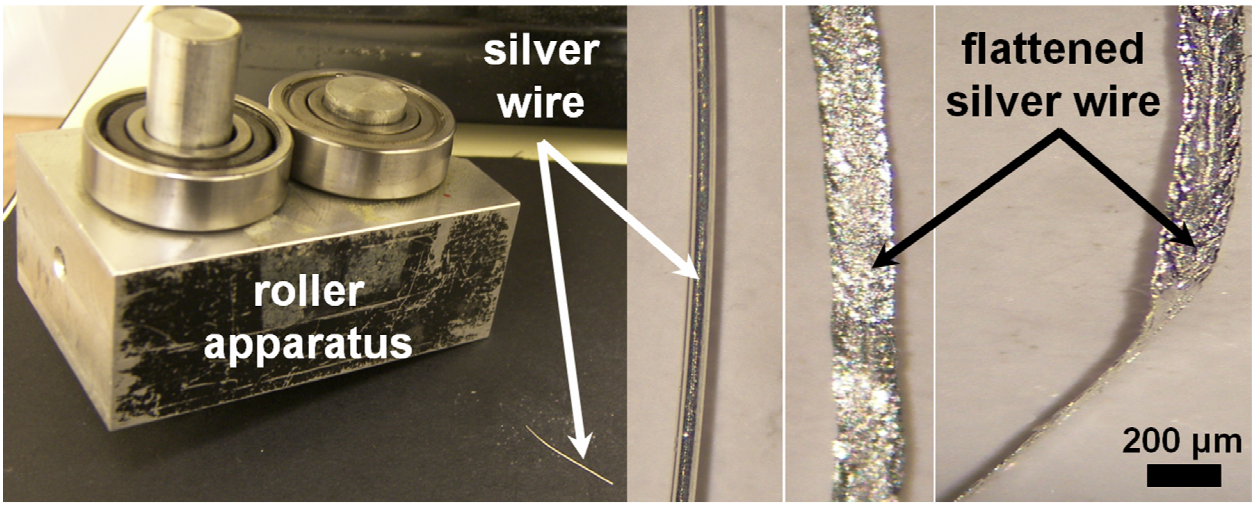

Figure 57: Mechanically flattening bare silver wire into a ribbon-like sensor. a-b) The mechanical roller apparatus and bare silver wire. c-d) After the silver wire was flattened, the width of the largest face of the ribbon-like sensor consisted of a dimension ~200 µm. Twisting the ribbon, one can visualize the large aspect ratio of the sensor, i.e. the width of the ribbon sensor is much larger than its thickness.

Ribbon Dimension	Measurement Count	Ribbon Count	Mean	Standard Deviation	% Error
Length (µm)	3	5	5037	150	3.0
Width (µm)	10	15	206	10	4.9
Thickness (µm)	5	10	32	3	9.4

Table 1: Ribbon dimension measurements. Ribbons were randomly selected and their lengths, widths and thicknesses were measured and averaged. Dimension measurements of the fabricated ribbons did not vary by more than 10%.

5.2.2. Attachment of ribbons to beam holders

Attachment of the ribbon-like sensor was made to a beam holder, which consisted of a flattened, large bore hypodermic needle (Small Parts, 18G hypodermic needle

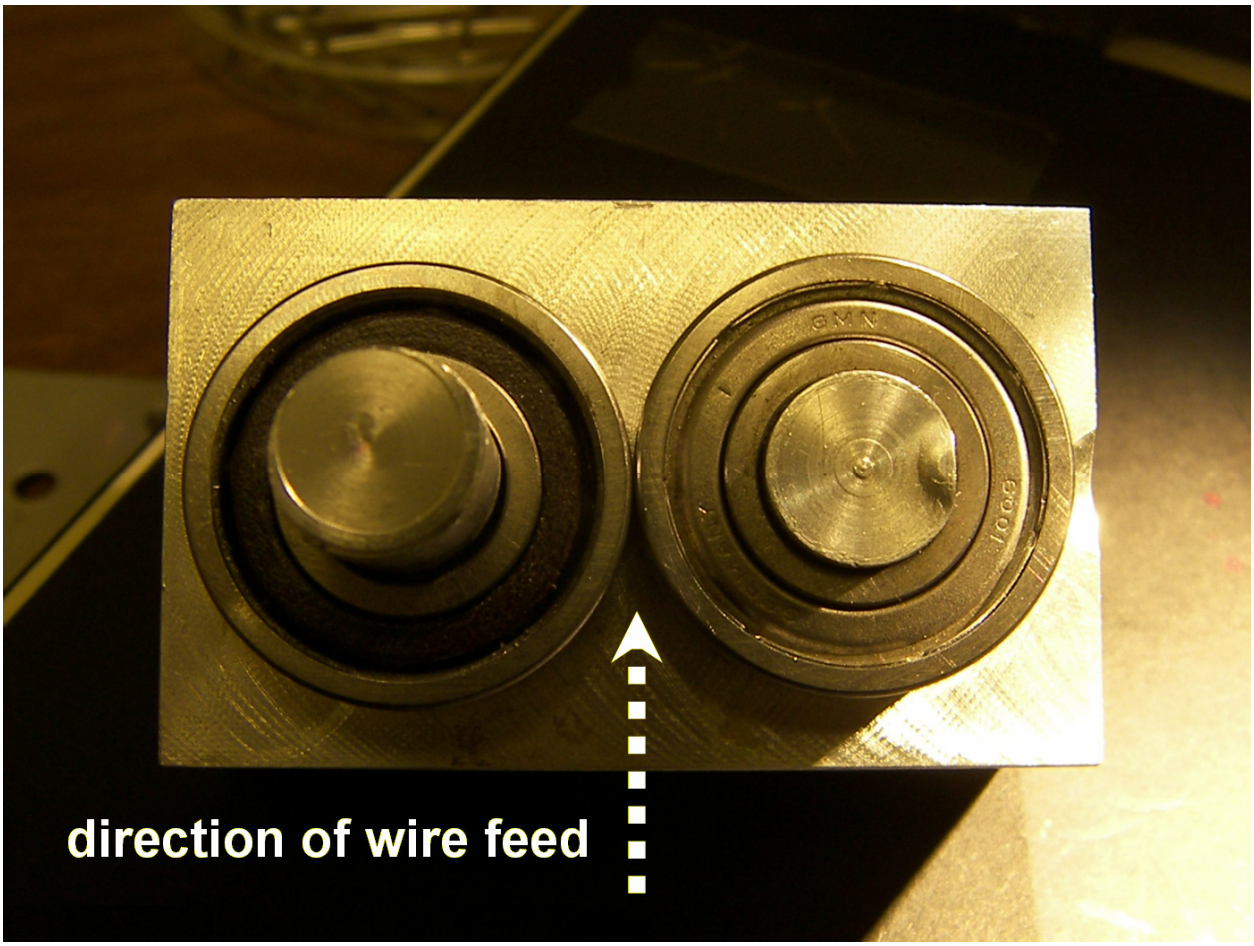

Figure 58: The mechanical roller apparatus. The white dashed arrow indicates how the silver wire was fed into the apparatus. The apparatus itself was consisted of two rotating bearings which had a diameter of 27.98 mm (left) and 28 mm (right). The spacing between the bearings was approximately 20 µm, which closely matched the thickness of the developed ribbon-like sensors.

#NE-183PL-C). The hypodermic needle was 4 cm long and 1.5 mm in diameter. After the Luer-lock connector of the needle was removed, the last 8.5 mm of the needle was completely flattened using a standard vice. The needle was released and the rounded end was then held firmly by the same vice so that the flattened end was free. The orientation of the needle was such that the largest face of the flattened end was parallel to the ground. A large head pliers was subsequently used to grip the flattened end of the needle, and was then twisted axially 90 deg counter-clockwise and 45 deg away

from the ground to create a "hockey stick" geometry. The geometry allowed for the attachment of the ribbon sensor and a reference beam using superglue on opposite sides of the beam holder (**figure 59a**).

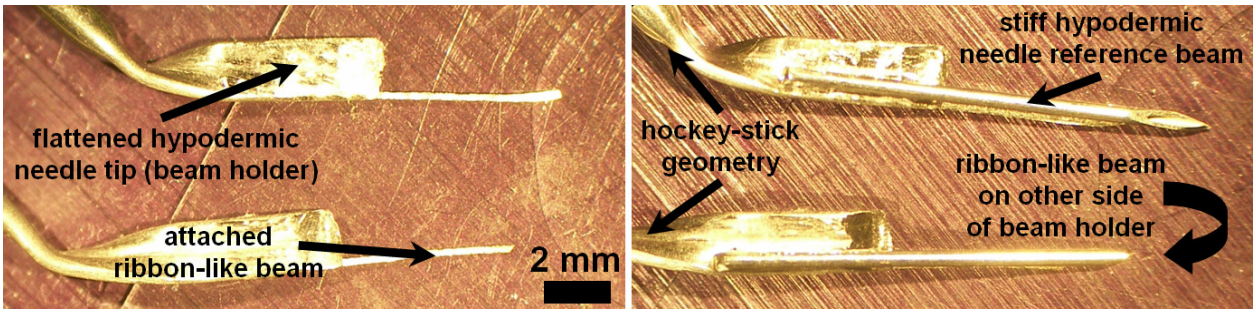

a b

Figure 59: Attachment of the ribbon-like sensor and reference beam to the holder.

A reference beam consisted of another hypodermic needle (BD Medical, 26G 1/2 hypodermic needle #305111) that was chosen because of its diameter and high elastic modulus (E_{SS304} = 194 GPa versus E_{Ag} = 83 GPa). The beam was a stainless steel grade 304 hypodermic needle (**figure 59b**) that was 12.5 mm long and 450 µm in diameter. After cutting-off the luer-lock connector, the needle diameter was measured under the microscope in three places along the shaft for 10 random samples to check manufacturing consistency. Measurements did not vary by more than 1% from manufacturer specifications.

In comparison to the previously used nanolevers for force measurement at the exclusion zone (**figure 31-33**), ribbon-like sensors were approximately 8 times longer and occupied a much greater cross sectional area (**figure 60**) than their batch microfabricated counterparts.

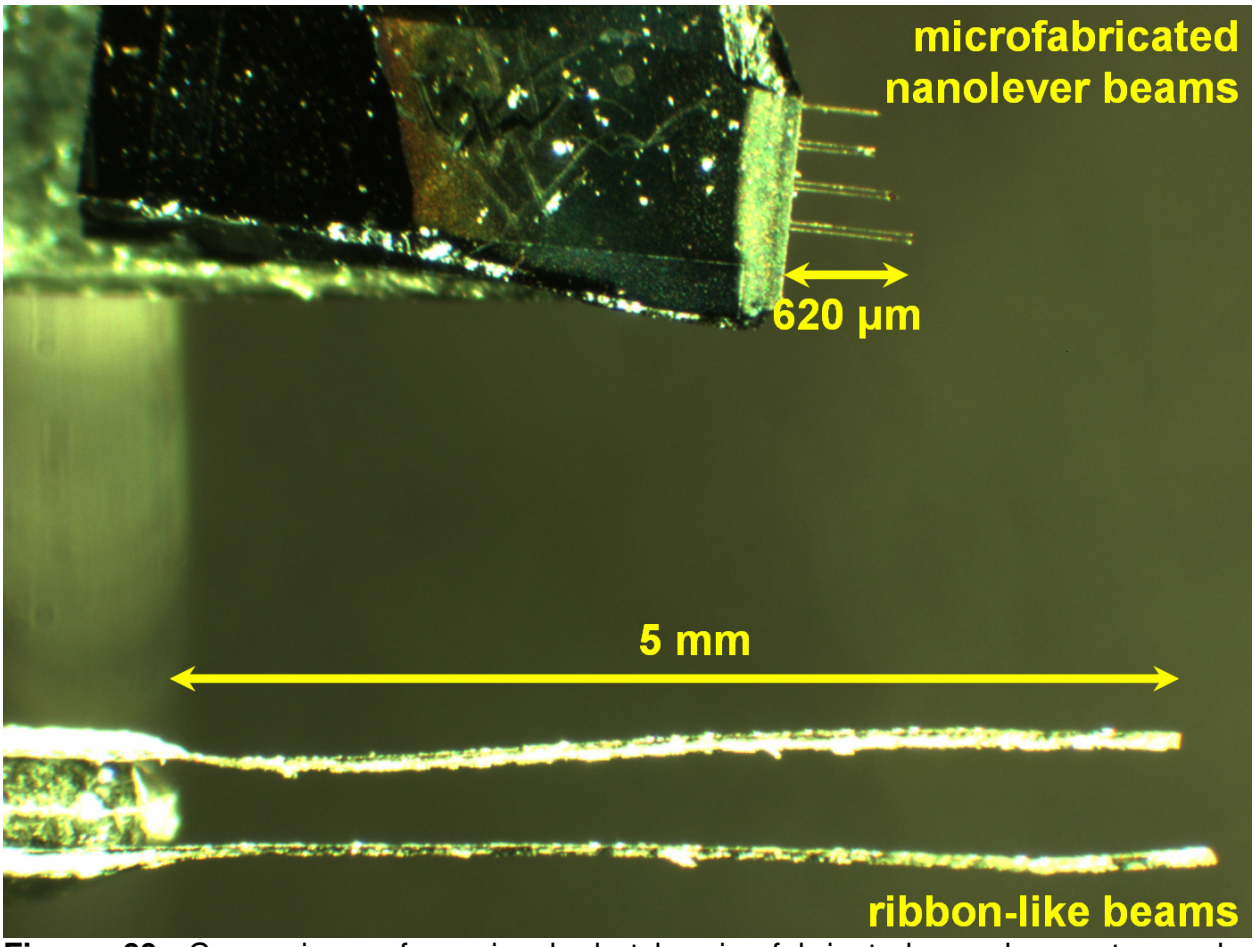

Figure 60: Comparison of previously batch microfabricated nanolevers to newly-developed ribbon-like beam sensors.

5.2.3. Stiffness and characterization of ribbon-like sensors

To characterize and measure the stiffness of the mechanical sensors, Euler-Bernoulli beam equations (**figure 61**) were utilized in conjunction with the measured beam dimension data. Due to chamber geometry and experimental constraints, ribbon and reference beam lengths were fixed at 5 mm for EZ experiments.

Beam dimension measurements were inputted into the corresponding equation and stiffness was thus calculated. For comparison, stiffnesses of the original silver wire, the

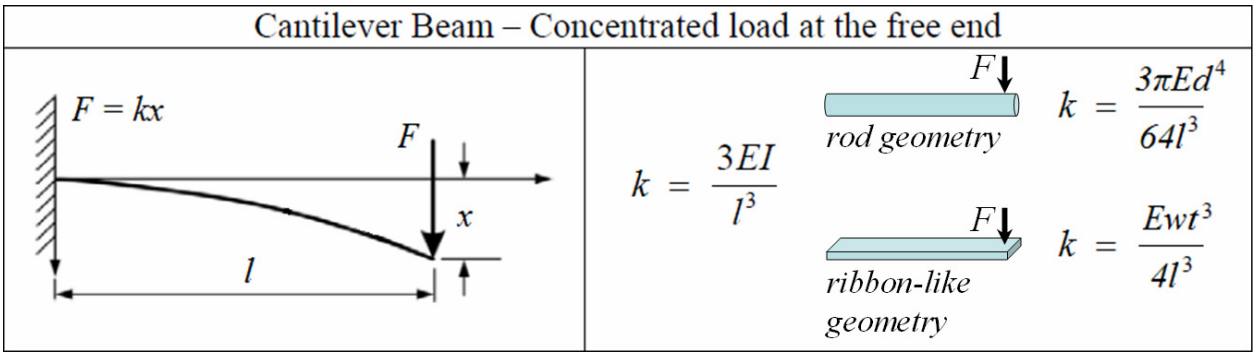

Figure 61: Euler-Bernoulli equations for a bending cantilever beam. Based upon cylinder and thin rectangular prism geometries, measured dimensions of each shape yielded stiffness coefficients for the specific cantilever beam of interest.

Beam Geometry	Stiffness k (pN/nm)	% Error	Factor Greater Than Ribbon
silver wire	**14877**	**12**	**14**
flattened silver wire (ribbon)	**1061**	**15**	**1**
ribbon in transverse direction	**45299**	**7**	**43**
reference beam	**3435889**	**4**	**3200**

Table 2: Ribbon sensor stiffness and the comparison to other beam orientations, beam types and geometries.

ribbon in the transverse (or edge-on) direction and the reference beam were also calculated from physical measurements (**table 2**).

Measured physical dimensions of the ribbon also allowed the calculation of the sensor's dampening coefficient. In air, the 5 mm long ribbon sensors have a dampening coefficient of $\zeta = 0.02$, which corresponds to an underdamped system. In water, however, sensors are nearly critically damped ($\zeta = 0.90$), thus response time for deflection (and hence force) measurement is optimal.

An alternative measurement of stiffness was accomplished through recording the resonant oscillation frequency of the sensor. By physically tapping on the beam holder,

mechanical impulses were delivered to ribbon sensors, which oscillated at their natural resonant frequencies. Resonant frequency was then inputted into an equation that yielded ribbon stiffness, such that

$$k = (2\pi f)^2 * \rho_{Ag} V$$

where k = ribbon stiffness in pN/nm, ρ_{Ag} = the density of silver (10.49 g/cm^3) and V = the measured volume of the ribbon sensor.

Two experimental methods were used to measure resonant frequency. The first method was simply a video recording at 1000-2000 fps of the ribbon tip position, after the sensor was placed above the objective and a mechanical impulse was delivered to the assembly (**figure 62a**). For shorter (stiffer) ribbons, the natural resonant oscillation frequency was too fast for the camera system. Therefore, a second system (**figure 62b**) involved positioning the ribbon in the light path of an IR emitter and pin photodiode (PD) detector. The PD detector recorded variations in the light intensity at 10,000 Hz, thus light intensity variation was directly correlated to the oscillating ribbon.

Subsequent movies of the ribbon tip for the first method were broken into individual frames (**figure 63**). The optical center of mass of the ribbon tip was then calculated for each movie frame and plotted over time. In the second method, variations in the IR light intensity were acquired and recorded as an electrical signal, and also plotted over time.

Both methods produced position history data (**figure 64**), where the ribbon's oscillation harmonically decayed over time.

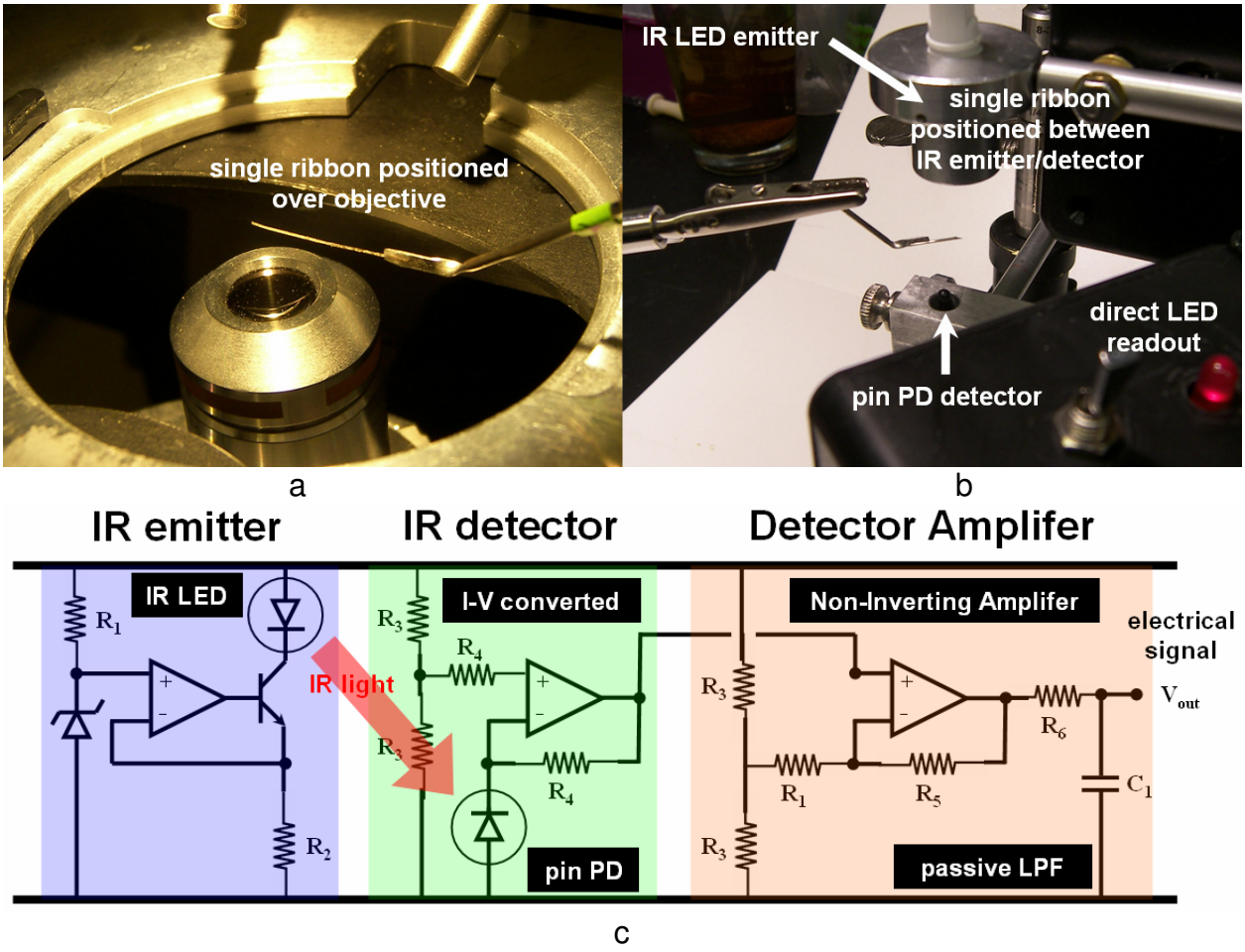

Figure 62: Alternative methods for measuring ribbon stiffness. a) The microscope objective and camera system recorded the tip of the ribbon as it oscillated at its natural resonant frequency once a mechanical impulse was delivered to the beam holder. b) Ribbon oscillation was recorded by the pin PD detector via the variation in the IR light originally transmitted by the IR emitter. c) The supportive custom-built circuitry for the IR emitter-detector system. A constant current source drove an IR light emitting diode (LED) to transmit light to a PD detector, which transduced the information into an electrical signal. The signal was passed through to a current-to-voltage converter and amplified. The amplified and filtered signal was then fed into a data acquisition system (National Instruments, Inc., NI USB-4009), which was controlled by a custom-written program in LabVIEW 8.5. Data were recorded and then analyzed in MATLAB10.

A fast Fourier transform (FFT) of the position history data for both methods was then performed and the corresponding frequency response curves were subsequently plotted

(**figure 65**). The dominant (peak) frequency of the curves was found and inputted into the stiffness equation to yield a stiffness for the ribbon sensor being tested.

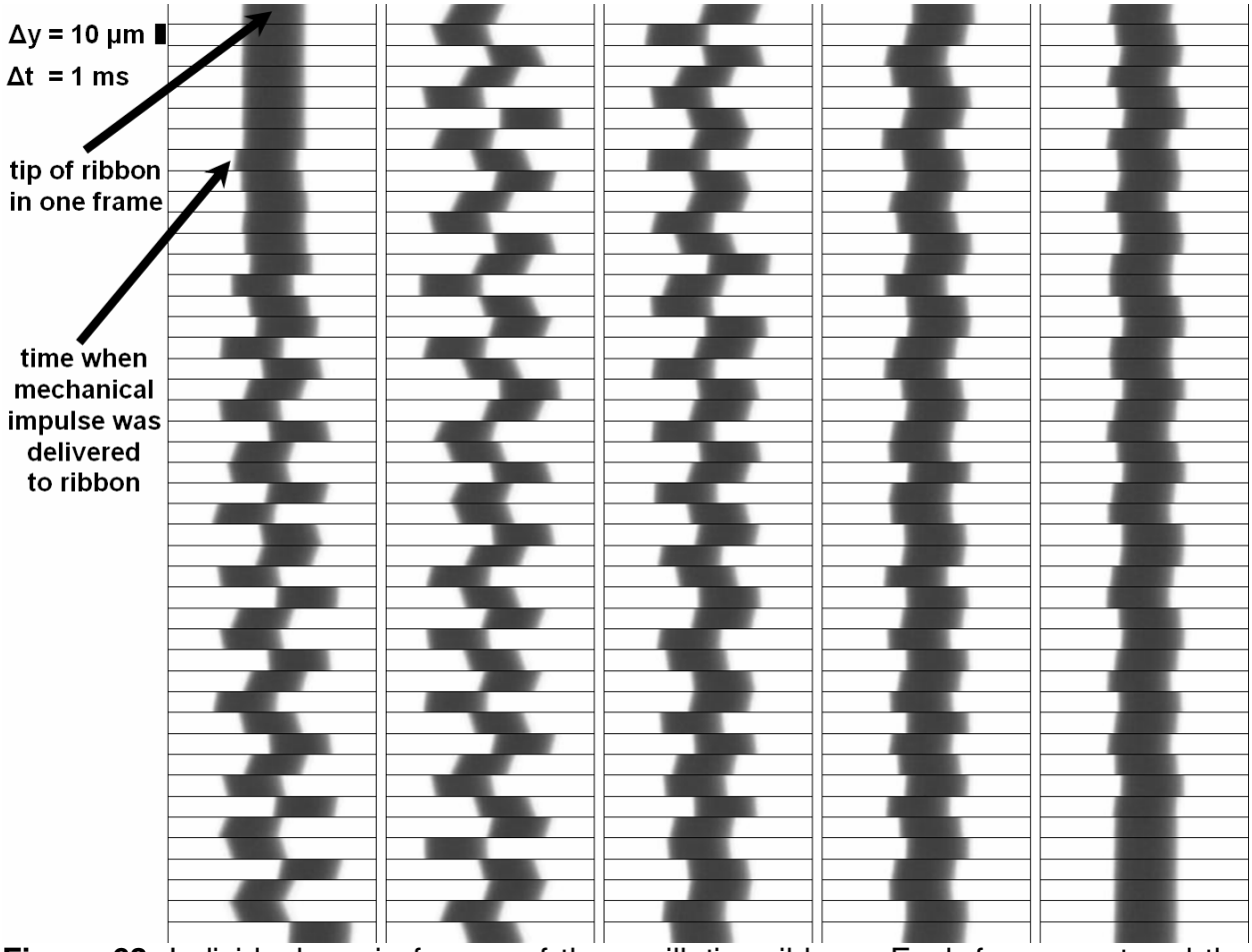

Figure 63: Individual movie frames of the oscillating ribbon. Each frame captured the very tip of the ribbon (and hence its position) in order to ascertain the stiffness coefficient of the sensor. See text for more details.

Ribbon sensor dimensions from **table 1**, were used to theoretically calculate different ribbon stiffnesses as a function of length (**figure 66**, in gray). Fabricated ribbons of various lengths were then used within the two methods described to measure ribbon resonant frequency. Five mechanical impulses were delivered to each ribbon length and the resonant frequencies were measured and averaged for a given ribbon.

Stiffnesses were then calculated based upon these resonant frequency measurements and plotted on the same graph (**figure 66**, in blue).

In **figure 66**, the plot demonstrates that both methods measured a consistent ribbon stiffness for a given sensor length. Additionally, resonant frequency methods verified that simply taking physical dimension measurements of the ribbon and inputting these data into the cantilever beam equation was sufficient in determining sensor stiffness.

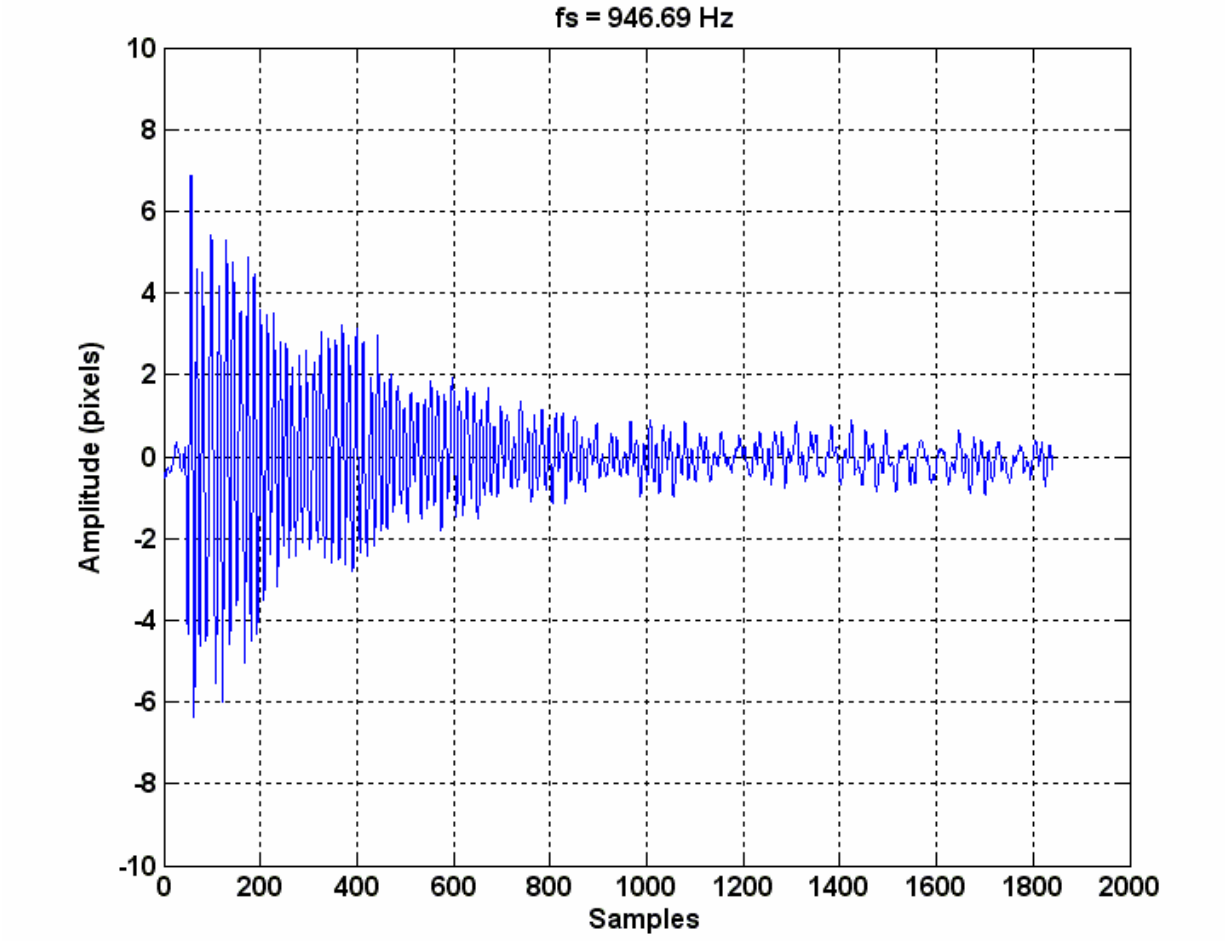

Figure 64: Position versus time of the oscillating ribbon sensor. The format of the position history data was the same for both methods since the optical center of mass of the ribbon tip in the movie for the first method and the variation in the light intensity of the second method were simply one-dimensional arrays of sample data over time.

Consistency of stiffness measurement for both methods also demonstrated the repeatability of the mechanical roller apparatus.

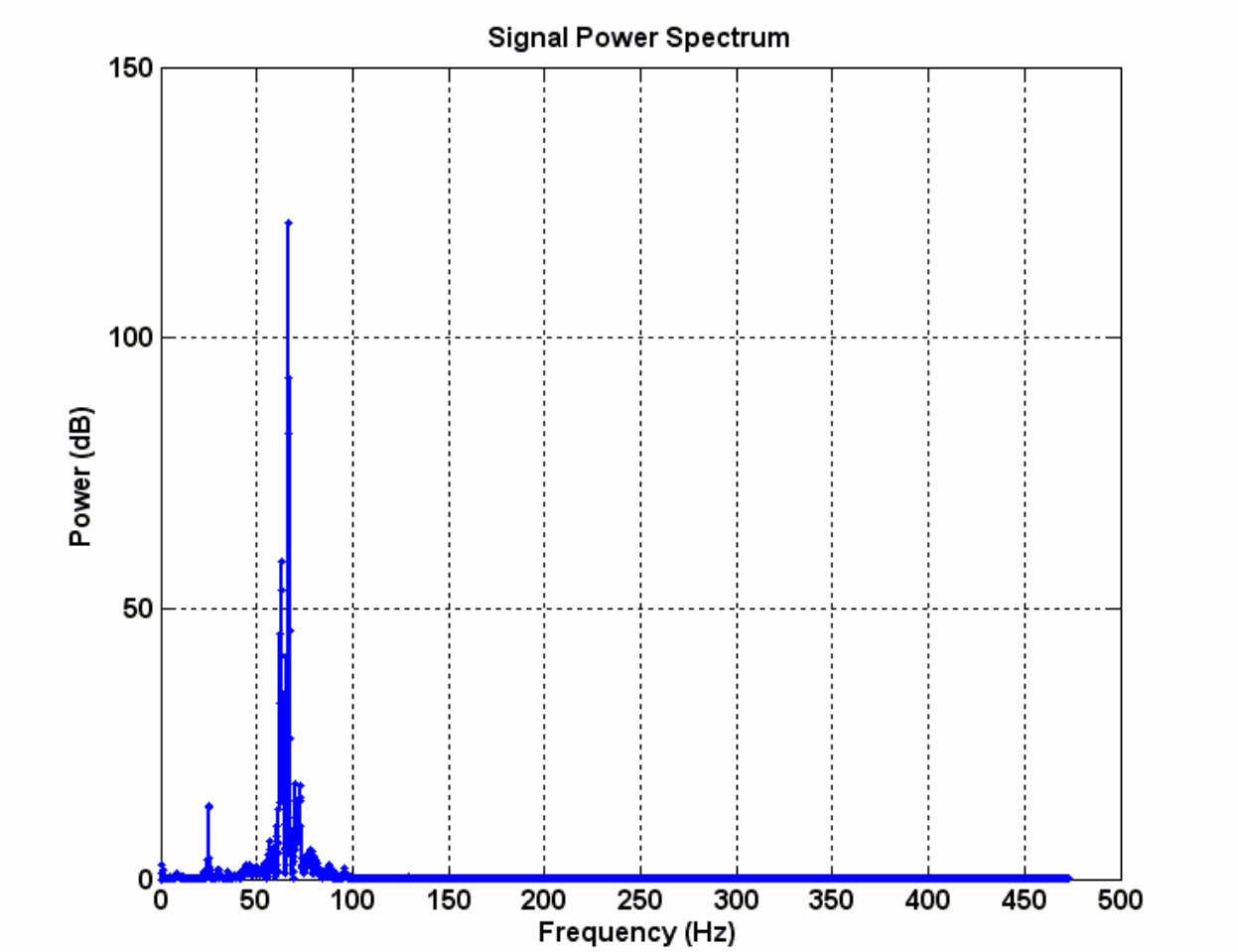

Figure 65: FFT of the position history data. The resonant frequency (denoted by the peak frequency above) was easily found from the frequency response curve of the ribbon sensor since the noise level of the measurement method was very low (illustrated by the flatness of the data outside the 50-100 Hz range).

For the 5 mm long ribbon sensors used for EZ experiments with Nafion tubes, ribbon stiffness was 1061 pN/nm and in the transverse (edge-on) direction was 43x greater than this stiffness. Reference beam stiffnesses were 3200x greater than the ribbon sensors themselves.

Additionally in **figure 66**, ribbon sensors from 1 to 20 mm lengths demonstrate a stiffness range from 150-0.010 nN/nm. When this information is combined with the field-of-view and spatial resolution of the camera system for the various experiments, the range of force that can be dynamically measured is 150 mN to 1 nN.

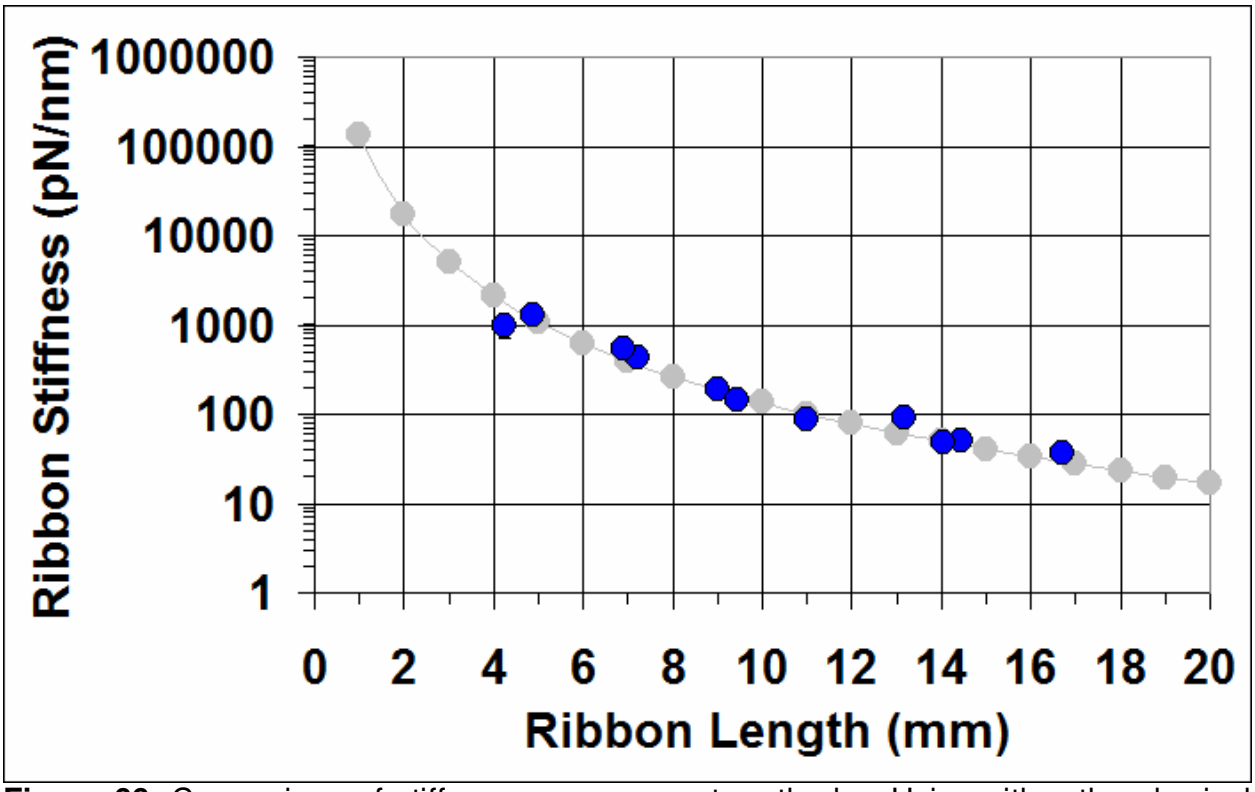

Figure 66: Comparison of stiffness measurement methods. Using either the physical dimensions of the ribbon (gray), or the ribbon's resonant frequency (blue) is sufficient for ascertaining the stiffness of a given ribbon sensor since both methods are consistent with each other. Data in blue are also shown with one standard deviation error bars.

To comprehend such a range of force, see **figure 67**. With the given optical specifications and settings, the ribbon-like force sensors could measure forces on the order of what an activated muscle fiber bundle generates to the effective weight of a single grain of sand 500 μm in diameter. This range of force was also compared to the nanolever force sensors. Ribbon-like sensors were versatile and covered a large

dynamic range of force. Force resolution was also limited only by the camera system and not the sensor itself.

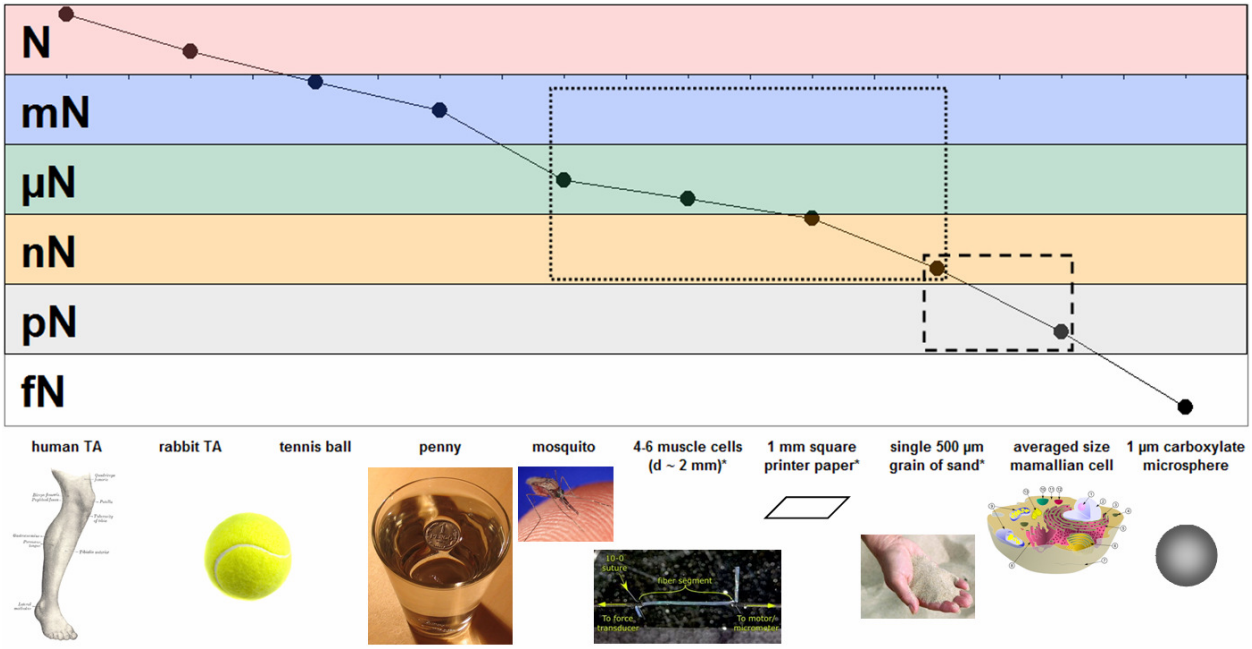

Figure 67: Ribbon sensor range of force. The large dotted box indicates the range of force for the ribbon sensors at the fixed field-of-view and spatial resolution of the camera system. The smaller dotted box indicates the range of force measurement for the previously developed nanolever force sensors.

5.2.4. Nafion tube samples and tube cutter

In order to block proton diffusion on one side of the Nafion tube and to also ensure consist results, Nafion tubes had to be cut in a precise and accurate fashion such that the fabricated ribbons were as wide (or wider) than the length of the Nafion tube. Therefore, a Nafion tube cutter was developed to cut Nafion tube samples in a fashion similar to the way a salami cutter operates. Thin microscope coverslips were used as spacers to fashion channels in which Nafion tubes were precisely cut. Details of the method are found in **figure 68**.

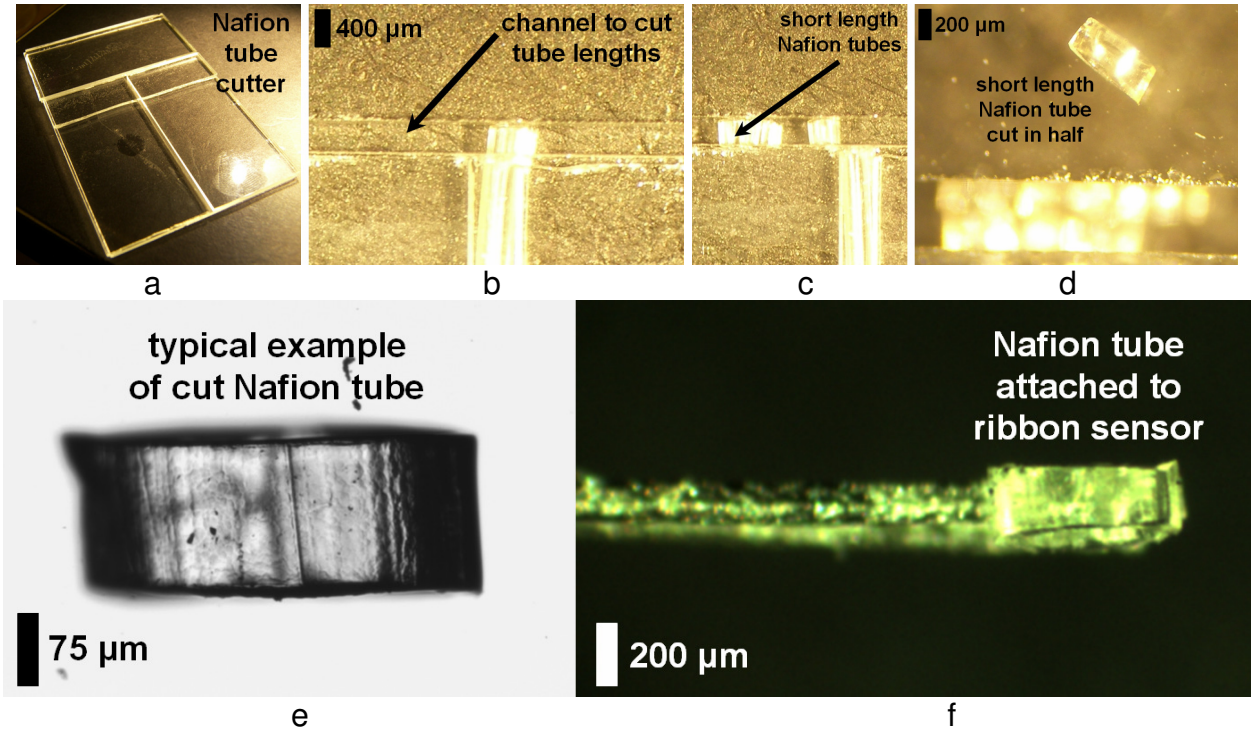

Figure 68: Nafion tube cutter and attachment. a-d) The Nafion tube cutter was made from glass microscope slides arranged in a configuration so as to make a T-channel. UV-curing (Norland Optical Adhesive, Model #NOA 72) glue was then used to fix the microscope slides in place. Nafion tubes were cut to corresponding lengths similar to the sizes used in experiments measuring pH-dye and electrical potential distributions (figure 51-52). e) A Nafion tube sample as observed under the microscope. Nafion tube samples were randomly selected and measured under the microscope. The average length was 200 ± 15 µm (n = 10 tubes), slightly less than the width of the fabricated ribbon-like sensors. f) Nafion tubes were then attached to the tips of ribbon sensors using superglue.

5.3. The completed sensor assembly

Once assembled (**figure 69a**), the mechanical sensor was placed in the middle of the chamber (**figure 69b**). The chamber (**figure 70a**) was the same as the one that was used for previously described experiments (**figure 51-52**). An identical volume of water was also added over a period of one minute (**figure 70b-g**) in order to minimize the disruptive effects of turbulence.

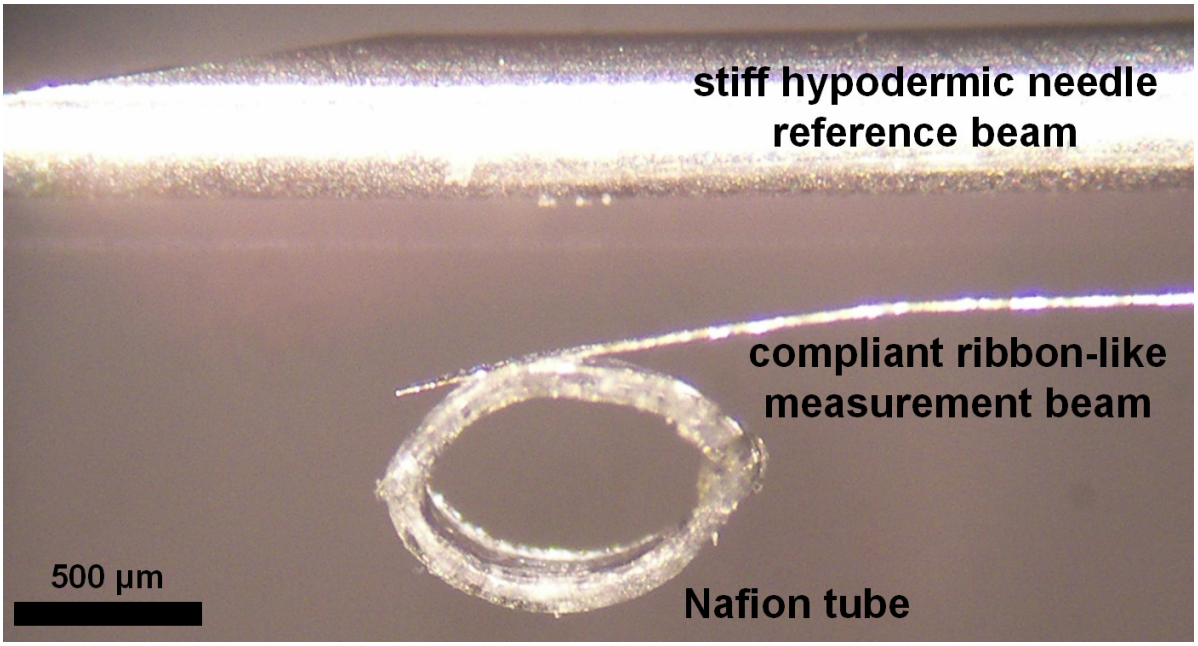

a

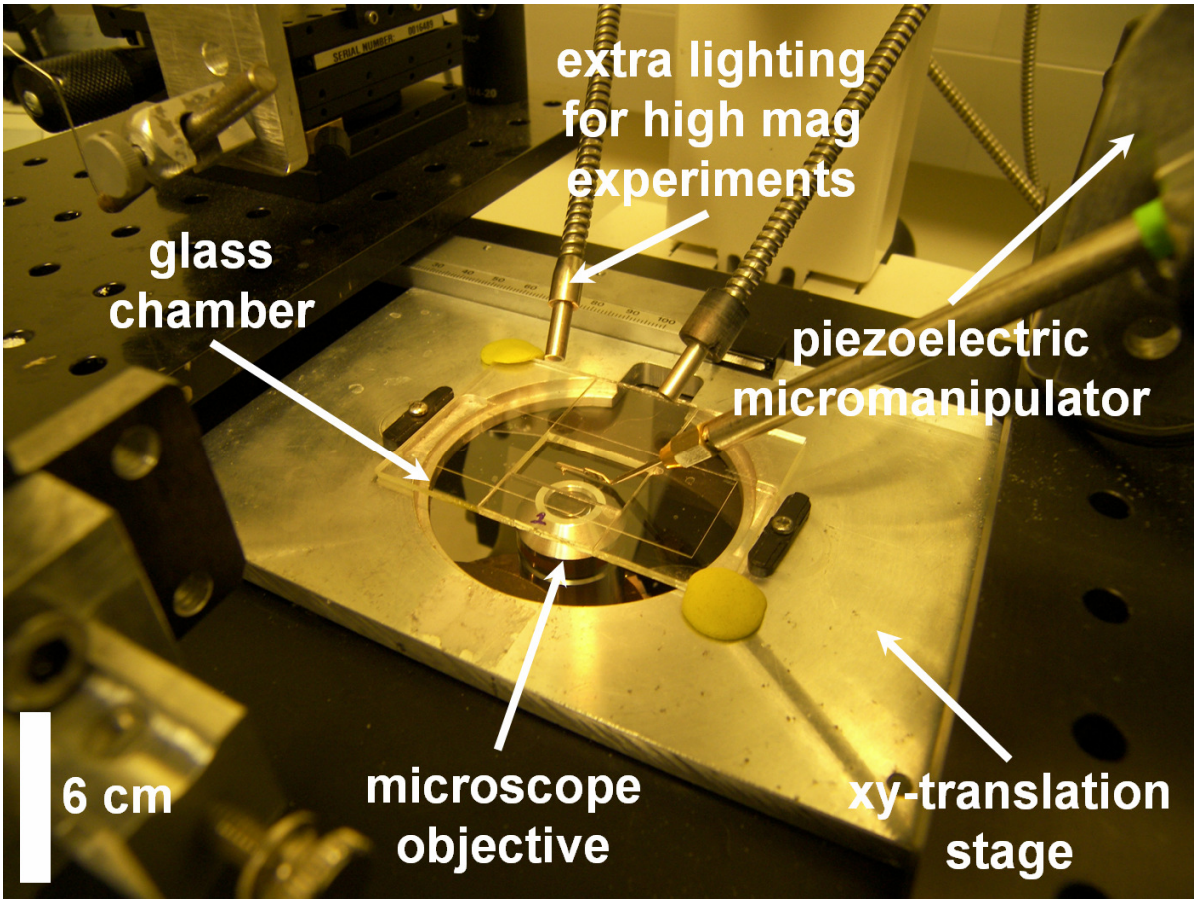

b

Figure 69: The completed mechanical setup. a) A Nafion tube-attached ribbon sensor and the corresponding stiff reference beam. b) The completed assembly was positioned in the center of the chamber located on the modified microscope stage.

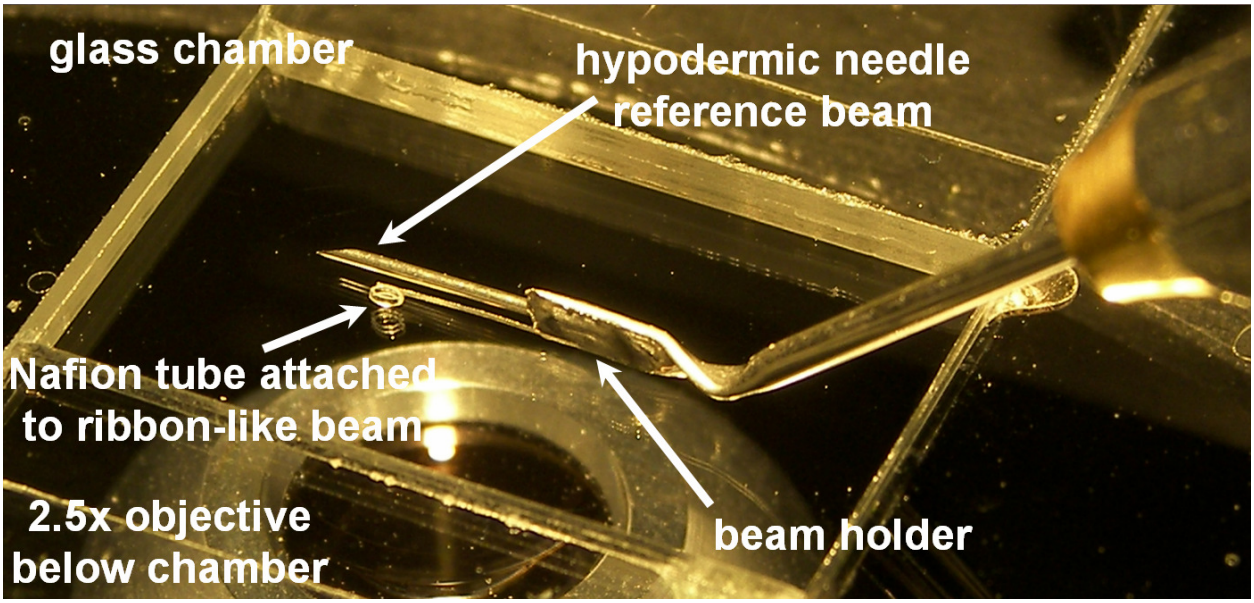

a

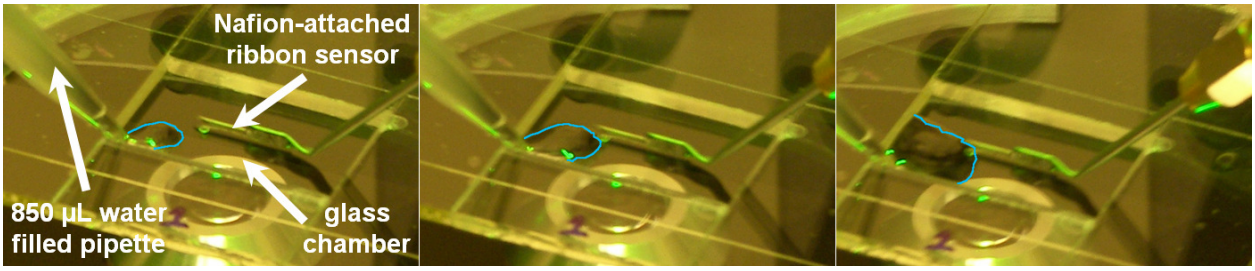

b c d

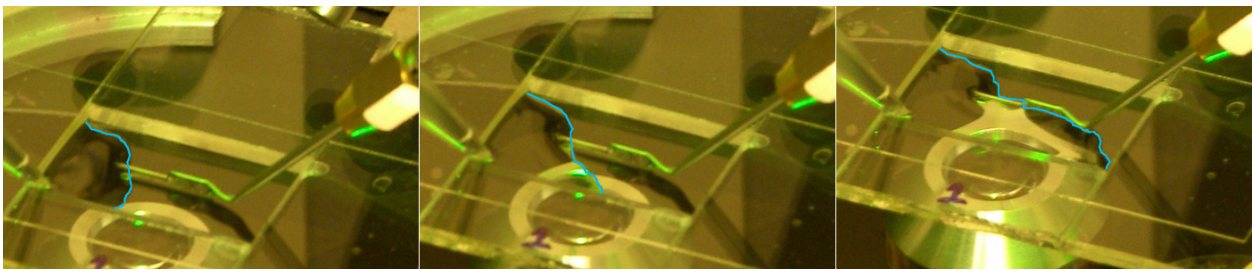

e f g

Figure 70: The completed assembly and chamber filling. a) Close-up view of the completed sensor assembly from figure 69b. b-g) Filling the chamber with a bath of ultrapure water. The chamber was slowly filled as to avoid excessive turbulence. The blue line outlines the boundary of the 850 µL water bath front as it filled the glass chamber. To fill the chamber, the pipette was always positioned in the bottom left corner. This was determined by trial-and-error to generate the least amount of turbulence since the filling is affected initially by surface tension and capillary effects.

5.4. Sensor deflection and force measurement

Measurement and reference beam positions were recorded in a movie (**figure 71**) at 5 fps using a LabVIEW-controlled camera (**figure 22**). A MATLAB-based algorithm measured and analyzed effective beam positions in the movie (**figure 72**) and plotted their positions over time. Control experiments consisted of the same experimental procedures, but without an attached Nafion tube.

Selected movie frames at the beginning, middle and end of a representative run are displayed in **figure 71**. The ribbon deflection is visualized by the vertical position change of the pink arrow. After water was added at 0 min, the sensor deflected away from the stationary reference beam. By 20 min, deflection in this run was ~25-30 µm. Quantitative records of beam positions over time and corresponding records for experiments without an attached Nafion tube are plotted in **figure 73**.

Approximately 75% of the maximum recorded deflection occurred within the first 90 s of adding the water bath (**figure 73**-top); deflection continued for the duration of the experiment. When no Nafion tube was attached to the sensor (**figure 73**-bottom), the sensor remained relatively static, varying no more than 1-3 µm throughout the experimental run.

Experiments, both with and without a Nafion tube attached to the sensor, were repeated 10 times each. A point-by-point mean and one standard deviation were calculated for

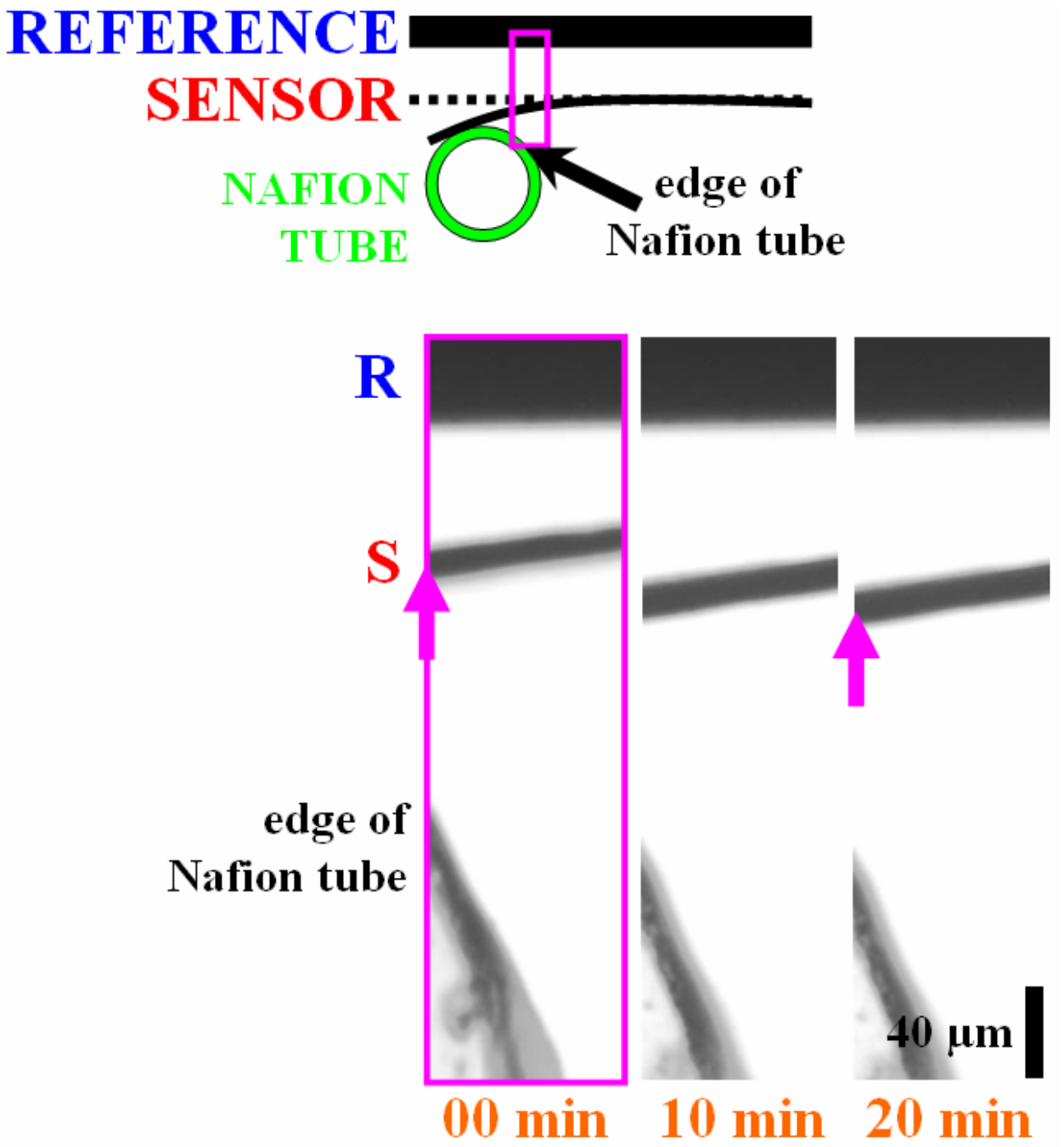

Figure 71: Representative experiment measuring ribbon deflection when an exclusion zone-generating Nafion tube was attached near the ribbon sensor's tip. The pink rectangle in the diagram defines the area of the experiment recorded by the camera system and is expanded for the individual movie frames. Individual movies frames at 0, 10 and 20 min are displayed. Water was added just prior to the 0 min movie frame. The pink arrows point to the midpoint of the linear distance spanning the ribbon's thickness (edge). Exact beam positions were found through the calculation of the optical center of mass from an intensity profile and is discussed in figure 72.

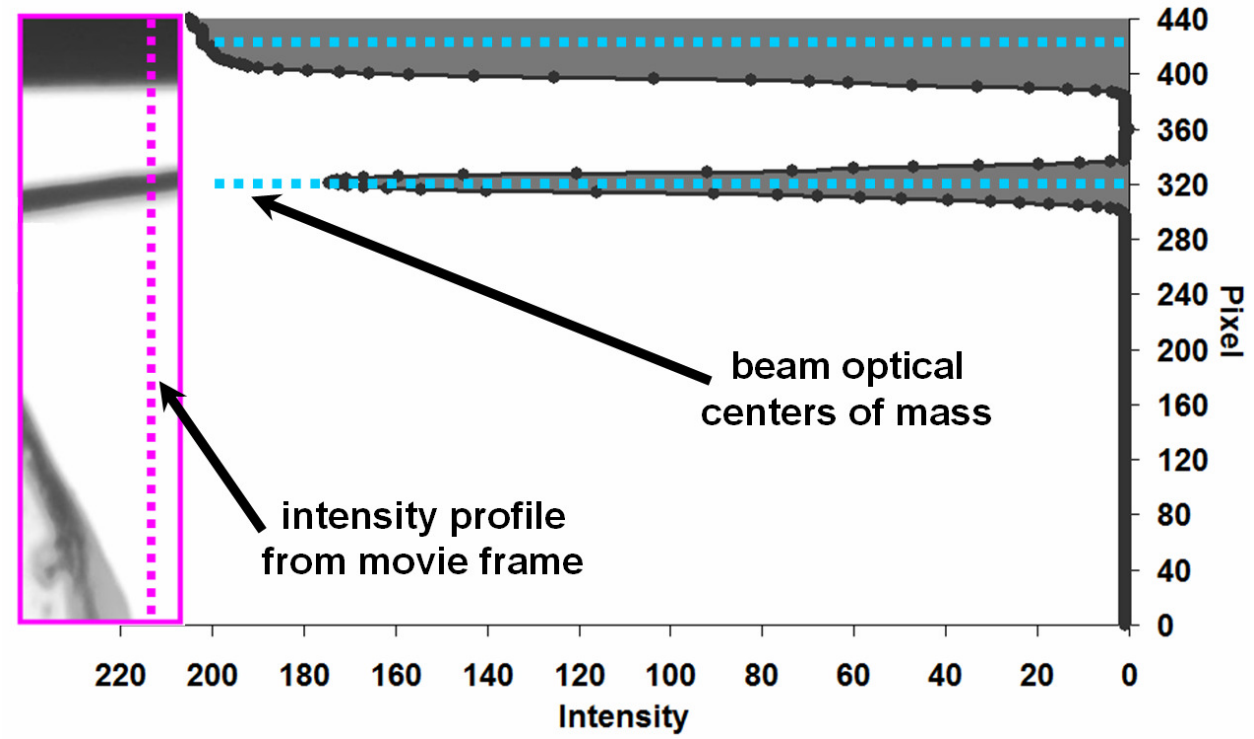

Figure 72: Measurement of beam positions. A single intensity profile was taken from each frame of the recorded movie. The centers of mass for the optical distributions of the corresponding beams was then calculated using a custom-written MATLAB10 program and plotted over time. Although the peak positions of the optical distributions were initially tracked, recorded and used in analyses, the center of mass proved to be a more accurate and sensitive parameter to measure beam position.

all experiments and plotted in **figure 74**. The averaged record (**figure 74**, in green) was significantly greater than control, when no Nafion tube was attached (**figure 74**, in blue).

Measured deflection data were then converted to force values in **figure 75** using the ribbons' stiffness coefficient. At the end of the 20 min runs, the measured force averaged 22 ± 2 μN. To understand the magnitude of such a force, refer to **figure 67** mentioned earlier.

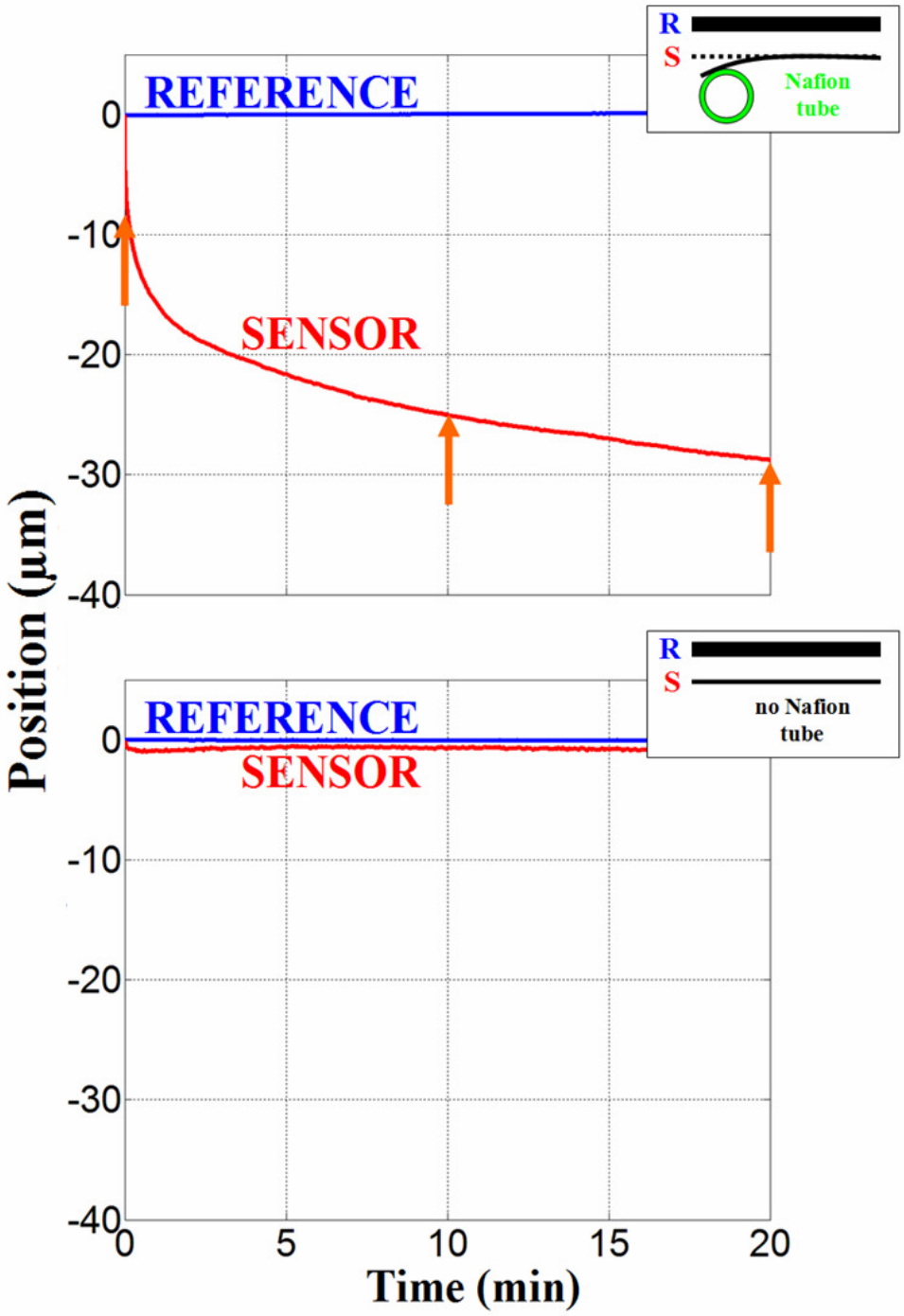

Figure 73: Quantitative records of the representative experiment. Position history of the sensor and reference beams (top) demonstrate the sensor has deflected by 30 µm over the time of the experimental run. Orange arrows correspond to time points of the movie frames in figure 71. Bottom panel shows traces when no Nafion tube was attached to the sensor. Note that in the experiment, the Nafion tube-attached sensor does not reach steady-state, or a static position, even after a 20 min experimental run.

Many natural processes exhibit exponential behaviors; therefore the force data of **figure 75** were fit with a double exponential function (**figure 75**, in red). Using the "fminsearch" root-finding method in MATLAB, the program calculated the ideal coefficients (A = 11, b1 = 3.2, b2 = 0.2) for the exponential function. A correlation coefficient of R^2 = 0.98 reflected how well the coefficients fit the function to the averaged force data.

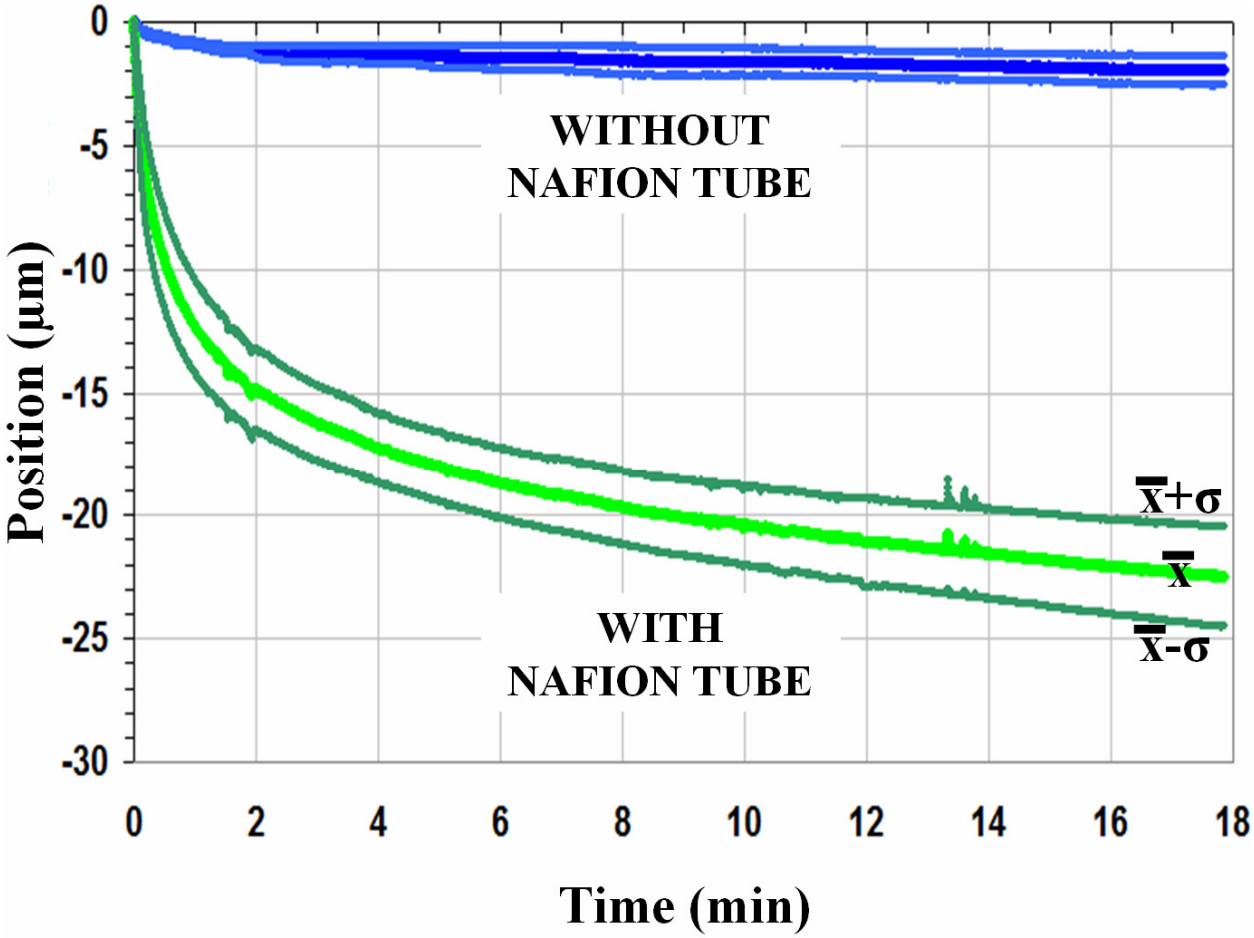

Figure 74: Summary of mechanical results. Point-by-point average (bright green trace) and one standard deviation (dark green traces) of 10 mechanical deflection records obtained when a Nafion tube was attached to the sensor. Blue traces represent experiments when no Nafion tube was attached. Even after averaging, note that the sensor in the experiment has still not reached a steady-state deflection.

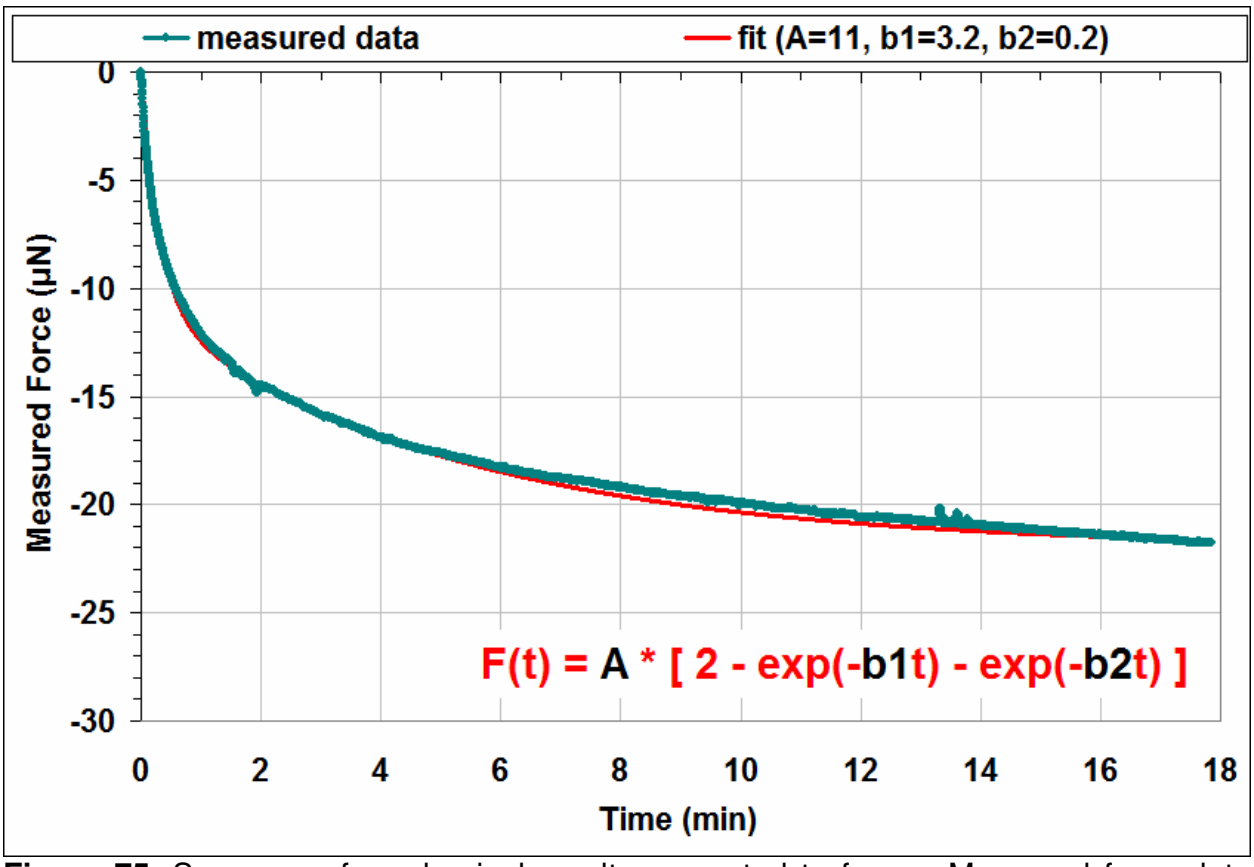

Figure 75: Summary of mechanical results converted to force. Measured force data (dark green) converted from data in figure 74 were fit with a double exponential function (red), $R^2 = 0.98$.

5.5. Proton obstruction and distribution

An attractive force was confirmed to exist between the EZ and PEZ and its magnitude was measured. However, existence of the force did not necessarily fully confirm the proposed hypothesis, or ensure that the phenomenon was based upon an electrostatic interaction. Therefore, the next goal of the study was to observe proton distributions and confirm that the ribbon design indeed restricted protons to one side of the mechanical sensor.

Hence, to observe that proton efflux was essentially unilateral on the ribbon, pH-dye (1:50 v/v in water) was pipetted into chambers containing the ribbon with an attached Nafion tube. Movies were recorded at 1 fps. Within the experimental run, an asymmetric proton distribution was visible and persisted over time (**figure 76**).

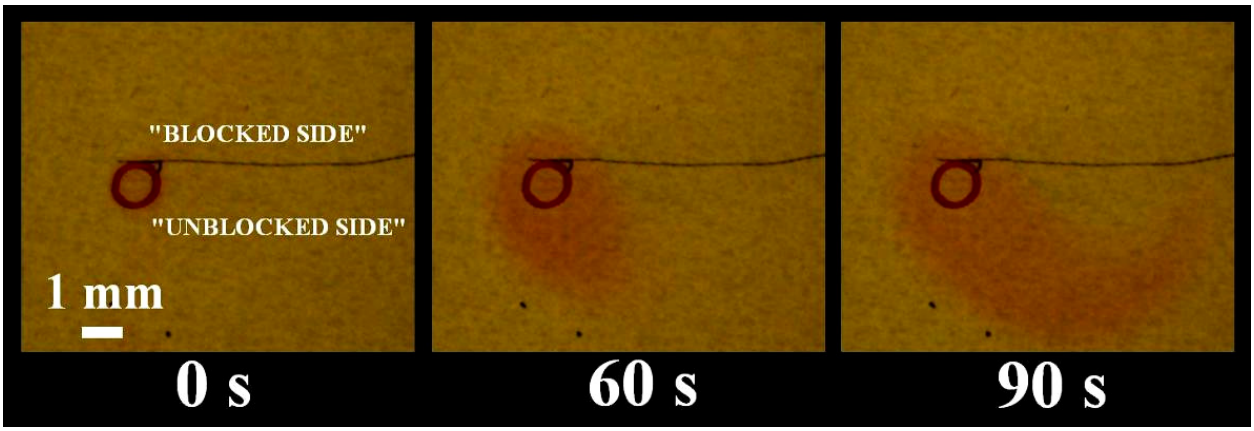

Figure 76: Proton distribution near the ribbon sensor with an attached Nafion tube. Most protons, indicated by the red color, were restricted to the side of the ribbon containing the Nafion tube. The tail-like formation at 90 s occurred randomly, but when present, never proceeded in the same direction on the unblocked side.

A MATLAB program analyzed the proton distributions of corresponding experiments over time. An intensity profile was thus obtained along a line perpendicular to the ribbon and passing through the tube's axis. The profile was divided into two segments, corresponding to the "blocked" and "unblocked" sides, and was plotted as a function of distance from the Nafion tube (**figure 77**).

The area under the curve (AUC) for both the blocked and unblocked sides was then plotted as a function of time (**figure 78**). Interestingly, the AUC for the pH-dye distributions reached a maximum between 60-90 s, a time period when 75% of the maximum recorded force was measured (**figure 75**). The proton distribution was therefore more heavily weighted on the same side where force was measured.

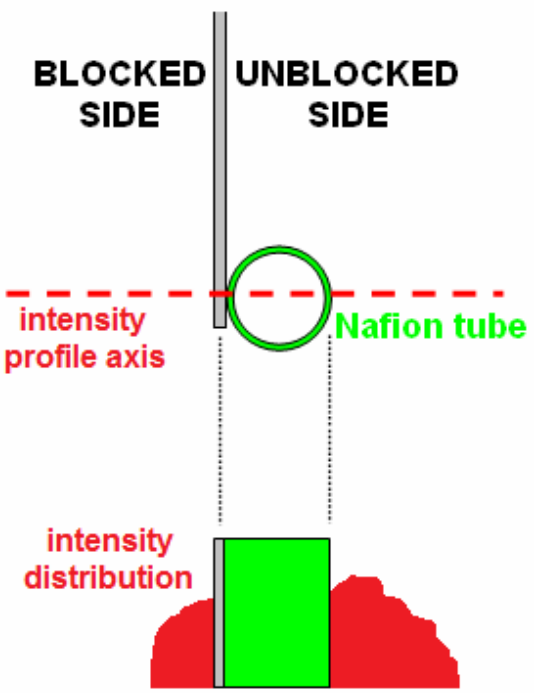

Figure 77: Method to measure proton distributions around the ribbon sensor. Intensity profiles were obtained from the blocked and unblocked sides within successive movie frames and were plotted as distributions.

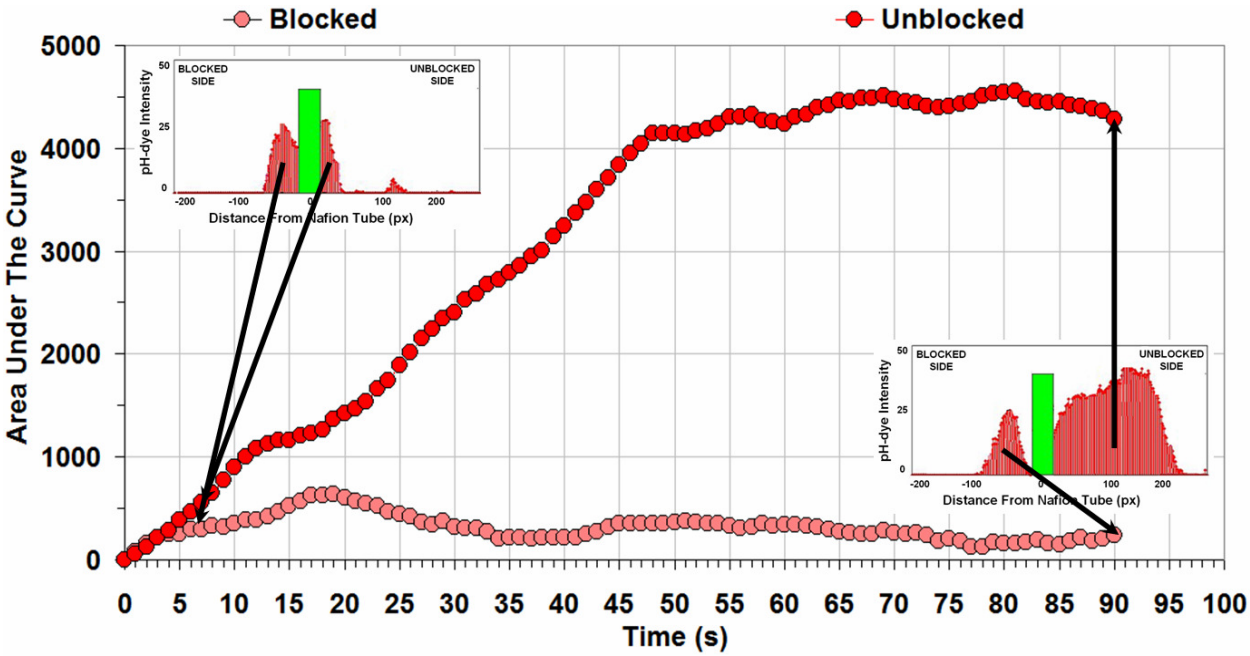

Figure 78: AUC of proton distributions versus time. The AUC is greatest on the unblocked side. Within seconds, the measured data on the blocked side reaches steady-state, indicating that proton diffusion was indeed obstructed, or was more heavily blocked.

5.6. Electrostatic calculation and correlation

In order to further correlate experimental measurements with (the hypothesized) electrostatic force, a simple theoretical calculation was employed using the data that were obtained from the pH-dye distributions (**figure 76-77**).

pH-dye distributions on either side of the Nafion tube-attached ribbon sensor were recorded and plotted (**figure 79**). Because an earlier calibration was performed with the pH-dye, pH value (and hence charge) and its distribution were calculated from the intensity profiles of the recorded movies. These data were then entered into an equation for computing electrostatic force. The purpose was to compare the computed electrostatic force with the measured mechanical force from **figure 75**.

If electrostatic force indeed exists between the (negative) exclusion zone and (positive) bulk water, a net force should drive the ribbon toward the unblocked region as was seen mechanically and qualitatively using pH-dye. Therefore, the ribbon's time course should be similar to the measured force time course. To calculate the electrostatic force, the standard expression for Coloumbic force was modified to account for charge distributions on both sides of the sensor. Thus,

$$F_{net} \sim (q_{- unbl}\, q_{+ unbl} / r_{unbl}^{2}) - (q_{- bl}\, q_{+ bl} / r_{bl}^{2})$$

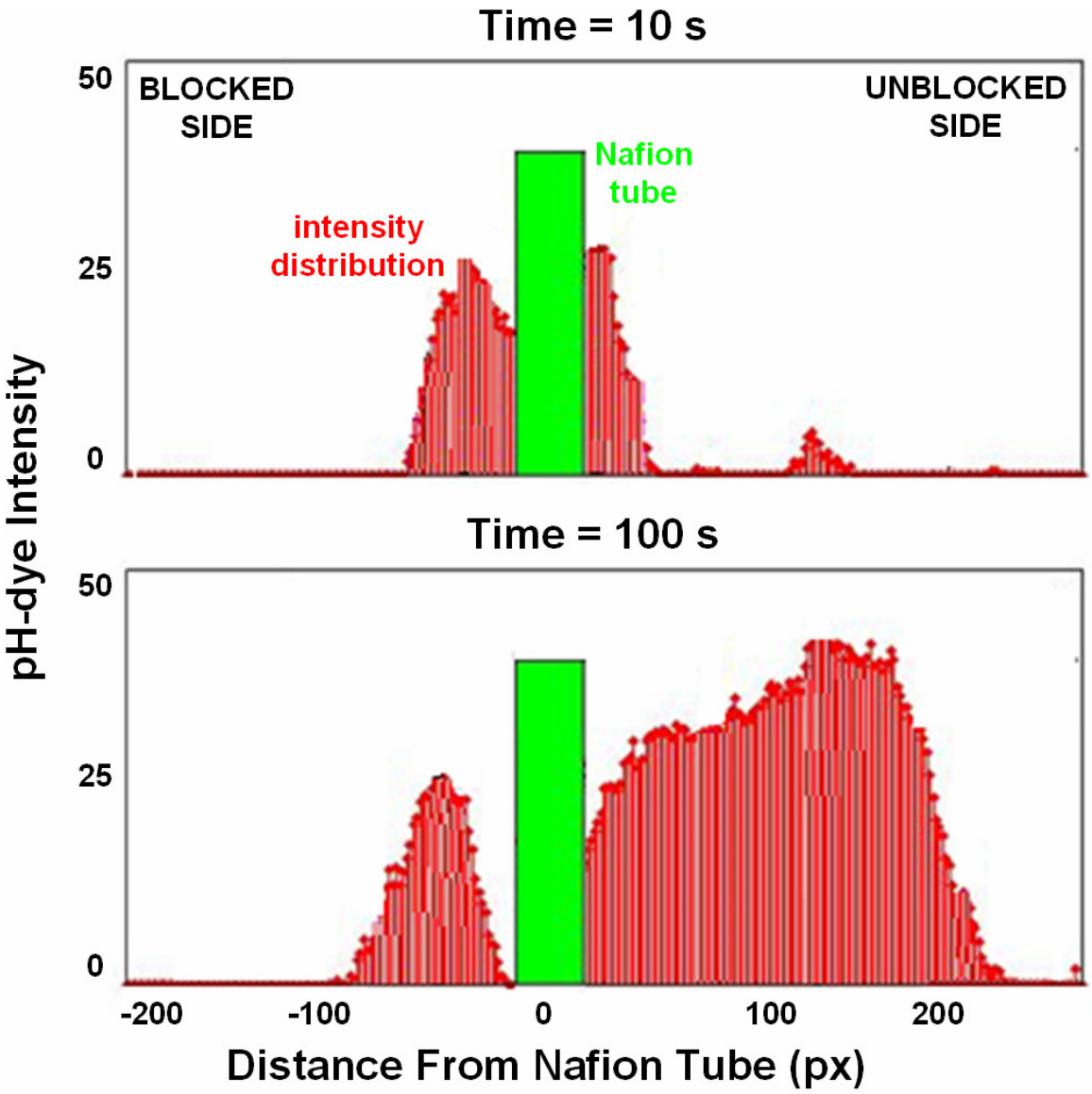

Figure 79: Quantitative measurement of proton distributions on both sides of the sensor. Red colored pH-dye intensity distribution data obtained from the blocked and unblocked sides at 10 s (top) and 100 s (bottom) into the experiment. Data show a distribution overwhelmingly weighted towards the unblocked side (where the Nafion tube was attached).

where F_{net} is the net force, $q_{-\ unbl/bl}$ is the total negative charge of the EZ on the unblocked/blocked side, $q_{+\ unbl/bl}$ is the total positive charge of the PEZ on the unblocked/blocked side and $r_{\ unbl/bl}$ is the separation distance between the unlike charged zones on the unblocked/blocked side. Since exclusion zones adjacent to

Nafion tubes were dye-free, the total negative charge of the exclusion zone was assumed to be equal to the total positive charge separated and measured by the pH-dye. Hence

$$F_{net}(t) \sim \Sigma [q_{i+\ unbl}{}^2 / r_{i\ unbl}{}^2] - \Sigma [q_{i+\ bl}{}^2 / r_{i\ bl}{}^2]$$

where $F_{net}(t)$ is the net force at time frame t of a movie recording and $q_{i+\ unbl/bl}$ is the charge magnitude located at a distance $r_{i\ unbl/bl}$ from the Nafion tube on the unblocked/blocked side at time frame t. The calculated electrostatic force was averaged across three experiments and plotted in red (**figure 80**). Measured force was plotted in green for comparison.

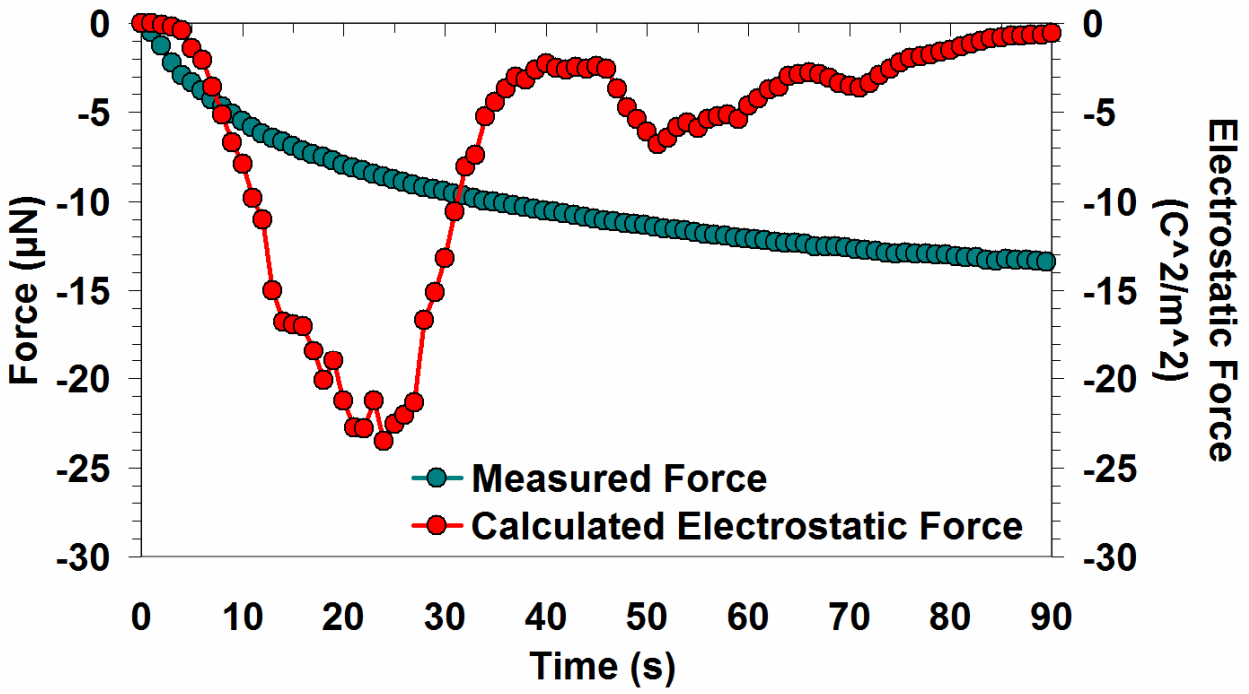

Figure 80: Correlation of calculated electrostatic force data (red) with measured force (green). The relative permittivity of the exclusion zone is unknown; therefore the units of the calculated force were kept in C^2/m^2.

The calculated force roughly tracked with measured force data initially, reaching a peak between 20-30 s, a period during which the measured force reached approximately half of the recorded maximum. The calculated force then dropped and eventually returned toward zero. This outcome shows that electrostatic forces can account for the initial bending of the ribbon, but after 30 s, additional factors must be considered, such as proton diffusion within the measured region (see discussion).

5.7. Discussion

Here, we tested the hypothesis that a significant force exists between the exclusion zone and the proton-enriched region beyond it, and we measured the magnitude of this attractive force. Mechanical force between the exclusion zone and bulk water was measured through the deflection of a ribbon-like force sensor attached to a Nafion tube (**figure 70a**). As the Nafion tube hydrated, the exclusion zone formed and was electrostatically attracted to the protonated bulk water, consequently drawing the mechanical sensor away from its reference beam (**figure73**-top). Deflection experiments demonstrated that a significant force on the order of 20 μN was measured between the exclusion zone and the bulk water. This finding confirmed our hypothesis that an attractive force exists between the exclusion zone and the proton-enriched zone in the bulk water.

However, in order to further support the hypothesis that this attractive force was electrostatic in nature, the geometry of the mechanical sensor was critical. Because the

ribbon-like sensor was wider than the Nafion tube, proton diffusion was largely obstructed on the side of the tube which was attached to the ribbon. This configuration isolated a majority of the protons to one side of the sensor (**figure 76**), thus the asymmetric proton distributions were heavily weighted in the same direction as the deflection (force) measurements of the sensor. Consequently at 90 s, when approximately 75% of the maximum recorded force was measured (**figure 75**), pH-dye distributions on the unblocked side extended more than 2.5 times greater into the bulk water than when compared to the blocked side (**figure 76**, at 90 s, **79**-bottom). The only logical explanation for the attractive force in this environment with a skewed proton distribution is an attractive electrostatic interaction between the exclusion zone and the bulk water region beyond.

When a simple, electrostatic calculation was employed using intensity profile measurements of the pH-dye distributions, the calculated record was well correlated with the measured force data for the first 30 s of the experiment (**figure 80**) and then decayed to zero. Proton diffusion may be responsible for such an error in the calculation. Overall red color intensity in a single one-dimensional profile decreases as protons diffuse three-dimensionally into the bulk water. While calculations showed an initially promising correlation and validated the hypothesized electrostatic attraction, future work will take into account intensity areas on the blocked and unblocked sides of the sensor than simple, one-dimensional intensity profiles, and resolve the sudden decay of the calculated force record.

Because the deflection of the mechanical sensor did not reach steady state even at 20 min (**figure 74-75**), a double exponential was fit to the force data (**figure 75**) to determine the time at which the sensor would reach a static position. Based upon the coefficients, mechanical deflection would have reached steady state in just over 2 hr. Although beyond the scope of this dissertation, three experiments with pH-dye and Nafion tubes were left overnight and demonstrated that the proton-rich region not only grew into the bulk water, filling the entire chamber, but that the dye continued to turn a darker red color. Therefore, it is unknown whether deflection would continue for such long time periods. Nevertheless, experiments on these timescales would have to be carefully conducted as to avoid significant evaporation of the 850 µL water bath.

Chapter 6: Control experiments and artifacts

Because of the unexpected nature of the observed force, we considered a number of possible artifacts that could have been responsible for the observed force.

6.1. Thermal gradients

The first and most obvious potential artifact was the possible existence of thermal gradients. Although Nafion's specific heat capacity (4.188 J/kg*K[114,117-118]) varies no more than 0.2% from that of water at room temperature, its thermal conductivity (0.12-0.18 W/m*K[114,117-118]) is three times lower than water's. This difference imply that in ambient conditions, the water bath should increase in temperature faster than the Nafion sample, resulting in a thermal gradient established between the Nafion tube and the surrounding water bath.

Thermal gradients in this case would be based on thermophoresis. However, while thermophoresis occurs at millimeter scales, similar to the scale of the various experiments conducted, thermophoretic movement opposite a thermal gradient is indicative of much smaller particles, on the order of 0.5-1 μm. Thus, it is not possible for the large macroscopic Nafion tubes, which have a much greater mass, to move in this fashion and cause the deflection measured by the mechanical sensors.

A second possibility is a temperature gradient in just the water bath itself. The temperature gradient, however, would have to be in a preferential direction, otherwise it would be impossible for a consistently measured unidirectional deflection to be caused by random convection. Therefore, simple thermocouples with a 1° C resolution were placed in the direct vicinity of the Nafion tube, within the surrounding water environment and at the chamber boundary. The position of the thermocouples was kept at the same level as the Nafion tube, i.e. midway between the air-water interface and the chamber bottom. For the duration of the experiment, the measured temperatures did not change within the 1° resolution. Significant temperature differences during the filling procedure itself were also not measured.

An IR camera (**figure 44**) with a resolution of 0.1° C was additionally used to record the temperature variations within the mechanical sensor setup as the water bath was pipetted into the chamber. False-color imaging was applied to the IR movies and is displayed in **figure 81**. Although very small thermal gradients were found around the sensor holder at the air-water interface, in three experiments, no gradients were found around the Nafion tube located at the tip of the mechanical sensor.

If water on the blocked side of the ribbon sensor was heated to a greater degree than the unblocked side due to the silver metal (which has a specific heat capacity and thermal conductivity 18x and 750x greater than water, respectively), then convection of water from the blocked to the unblocked side could have been responsible for a deflection of the mechanical sensor. Therefore, drops of hot water were added to the

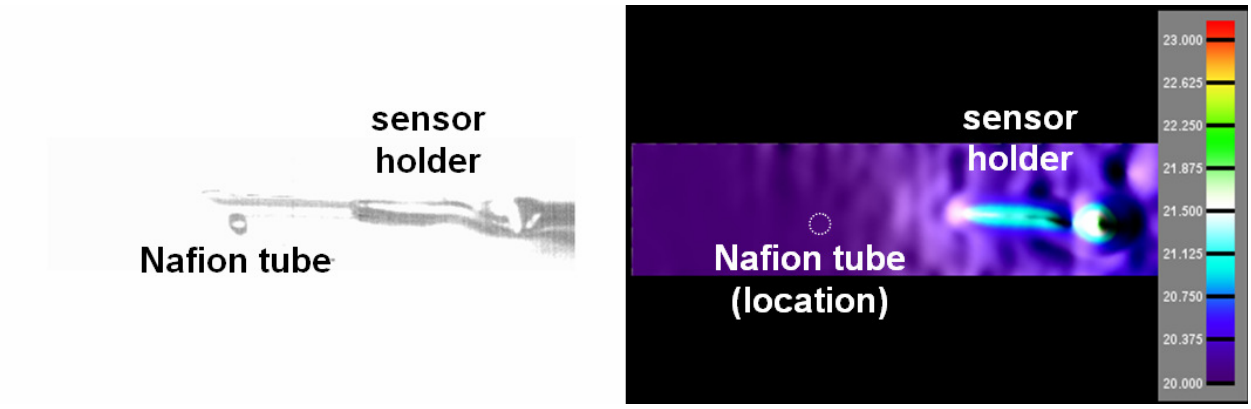

a b

Figure 81: IR imaging of the mechanical sensor with the attached Nafion tube. a) Gray scale image of the sensor and the Nafion tube. b) False color IR image of the setup after water was added. Scale bar is in Celsius. No significant gradients were visualized at the sensor tip, where the Nafion tube was attached.

water bath at the corners of the chamber and at the location of the mechanical sensor while the camera recorded the position of the sensor with no attached Nafion tube. No deflection was recorded in the sensor, except for minute perturbations when the drops made contact with the bath surface. The same perturbations were seen when drops of room temperature water were similarly added.

Perturbations were eliminated altogether by adding small water volumes beneath the air-water interface using a micropipette. However, aside from the smaller perturbations of the sensor caused by physically pipetting the water volume, no significant effect on the ribbon sensors was seen when hot, or cold water was added. Therefore, taking into account the previous data, we could find no evidence of thermally-driven convective gradients as a cause for the measured mechanical deflection.

6.2. Increasing density of a hydrating Nafion tube

Nafion's density is nearly twice that of water (1.91 g/cm^3) and it absorbs at least 20% water by weight (**figure 50**). Therefore, one possible artifact is the bending of the ribbon as the weight of the Nafion tube increased. The high aspect ratio of the ribbon ensured a high transverse stiffness, which we hoped would prevent "droopage" of the sensor in the transverse (edge-on) direction if the added water weight was significant. This droopage would be greatest in air, where no buoyancy force is present. Consequently, ribbon position in air with a dry versus hydrated Nafion tube was compared using a camera. The camera imaged the sensor axially and edge-on, similar to the mechanical experiments conducted above. No deflection with respect to the hydrated Nafion was visualized.

Also, during experiments, prior to and following each mechanical measurement underwater, the translation of the ribbon was verified to occur within the same focal plane. This was qualitatively confirmed by comparing the before and after images of the Nafion tube's top and bottom edges, or through simple observation via the eyepieces of the microscope.

Even the force generated by a theoretical mass of a fully hydrated Nafion solid cylinder accounts for no more than 5% of the maximum recorded force measured by the mechanical sensor. Solid Nafion cylinders (not tubes) were assumed to be hydrated by at least 50% w/w. When calculated, the amount of down-force produced by the cylinder

would be about 1.1 μN, which is less than a 1 μm deflection of the ribbon-like beam if the sensor was vertically oriented (i.e., deflection occurred perpendicular to the chamber floor). Because the ribbon was oriented laterally, the deflection would be significantly reduced and would have virtually no effect on the experiment.

6.3. Tube hydration

Tube hydration was also considered a possible artifact. As a Nafion tube is immersed in the bath, water rushing into the tube wall causes tube expansion due to hydration (**figure 50**). This could have possibly caused a deflection of the sensor due to unbalanced water flow. However, this artifact would be transient, and with one side of the Nafion tube blocked by the ribbon, water flow into the unblocked side would impede any deflection of the sensor. This predicted effect was contrary to our observations and measurements of sensor deflection.

6.4. Sensor mechanical polarization and inertness

To create sensors, a roller apparatus (**figure 58**) was used to make ribbons. The ribbons may have had a preferential bending direction, similar to a heated bimetal strip. Fabricated ribbons were therefore cut into sister pieces. A Nafion tube was attached to one ribbon and another was attached to the opposite side of its corresponding sister piece. Experiments were then conducted with both assemblies. Results confirmed that sensor deflection remained unaffected by mechanical polarization.

Both ribbon-like sensors and the beam holder were also put into a pH-dye/water bath to determine if any adverse pH effects, or stray charge was caused by the materials themselves (**figure 82**). When immersed in pH-dye, no pH-dye colors, or pH-dye color gradients were seen around any of the components of the mechanical sensor.

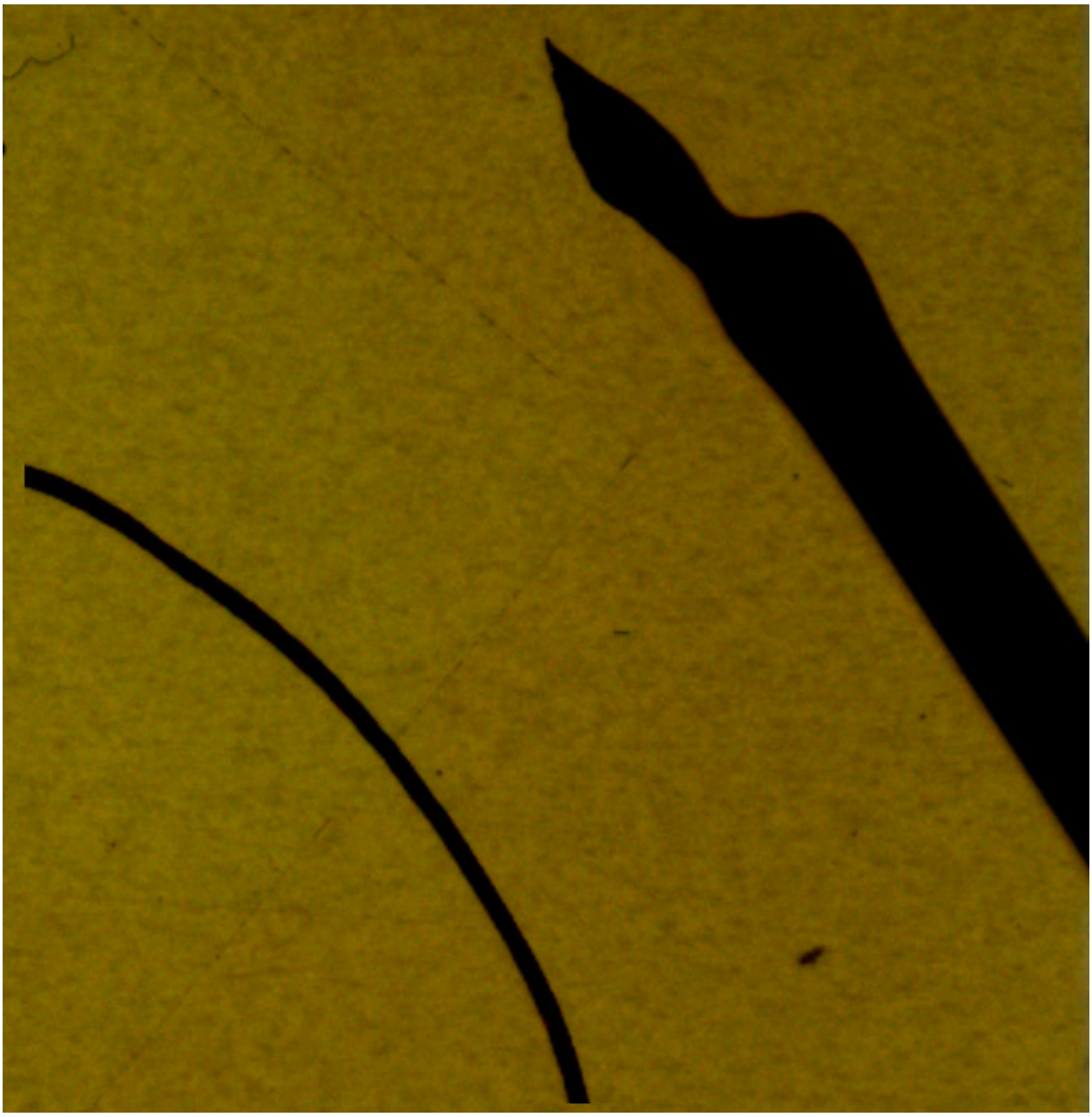

Figure 82: pH-dye observations around mechanical sensor components. No pH-dye color change, or pH-dye color gradients are seen next to the ribbon (left) itself, or the beam holder (right).

Chapter 7: Discussion and final conclusions

Many hydrophilic surfaces generate exclusion zones in the adjacent water. One such surface is Nafion, a charged, hydrophilic polymer that has been repeatably shown to generate a negatively charged zone that excludes colloids, microspheres and at least some solutes (**figure 20-21**, **24**, **51**). These exclusion zones are coupled with a proton-enriched region in the surrounding bulk water (**figure 24**, **51**). Therefore, understanding this charge separation phenomenon will provide insight into the long-range ordering of water at hydrophilic surfaces. Here, we tested the hypothesis that a significant force exists between the exclusion zone and the proton-enriched region beyond it, and we measured the magnitude of this attractive force.

To achieve such an objective, a benchtop system was designed to characterize the exclusion zone phenomenon through measurements of pH (**figure 24**), electrical potential (**figure 52-53**) and mechanical force (**figure 56**, **69-70**), under identical water bath conditions using similar sized, vertically-oriented Nafion tubes. Tubes surrounding a fitted platinum wire (**figure 20b**) visibly excluded universal pH-sensitive dye (**figure 24**, **51**). Although the dye could not reveal the pH distribution within the exclusion zone itself, dye distributions permitted thickness measurements of the exclusion zone and simultaneously provided an indicator of the proton-rich bulk water region. When the fitted platinum wire was used as a probing electrode, electrical potential differences between the probe and a reference platinum wire, placed at distant locations within the protonated water (**figure 52**), revealed a negative voltage measurement. This voltage

increased in magnitude as the separation distance between the wires was increased and plateaued at far distances (**figure 53**).

Finally, mechanical force between the exclusion zone and bulk water was measured through the deflection of a ribbon-like force sensor attached to a Nafion tube (**figure 56**, **70**, **71**, **73**). As the Nafion tube hydrated, the exclusion zone formed and was electrostatically attracted to the protonated bulk water, consequently drawing the mechanical sensor away from its reference beam (**figure 73**-top). Deflection experiments demonstrated that a significant force on the order of 20 μN (**figure 75**) was measured between the exclusion zone and the bulk water. This finding confirmed our hypothesis that an attractive force exists between the exclusion zone and the proton-rich bulk water.

The presumption that this attractive force is electrostatic in nature was confirmed through pH-dye experiments. Because the ribbon-like sensor was wider than the Nafion tube (**figure 56**), proton diffusion was largely obstructed on the side of the tube which was attached to the ribbon. This configuration isolated a majority of the protons to one side of the sensor (**figure 76**), thus the asymmetric proton distribution was heavily weighted in the same direction as the deflecting mechanical sensor. A mismatching of proton distributions on either side of the sensor and the measured mechanical deflection in the direction of the greater proton distribution directly implies electrostatic interaction. This was further validated through correlations of the measured mechanical

force to theoretical electrostatic calculations based upon intensity data obtained from pH-dye distributions of proton diffusion (**figure 80**).

Proton diffusion in the experiment also raises one simple question: why do the negatively charged exclusion zone and the proton-rich region not simply collapse and neutralize one another? Spectroscopic studies of the interfacial water zone at the Nafion surface[115,119-120] have demonstrated that the water at the interface exhibits a distinct ice-like organization: water molecules are neither organized in a fully coordinated tetrahedral arrangement like ice, nor are they simply free water molecules exhibiting random O-H stretching. The organized water along the Nafion polymer is also shown to be mechanically different and tightly bound to the Nafion's molecular structure[115-116,119-120], resisting evaporation even under intense vacuum[119]. Therefore, an accumulation of protons occurring at the outer boundary of the exclusion zone may cause the initial, rapid deflection of the mechanical sensor and reflect the bringing together of two unlike-charged zones, instead of simple charge neutralization and the collapse of corresponding zones.

Simultaneously, however, chemical potential forces the repulsion of like-charged protons to run down their chemical gradient and to diffuse into the bulk water region. This is further demonstrated in the voltage measurements (**figure 53**), where the probing electrode measured a negative electrical potential relative to the reference electrode, which was found in the proton-rich environment (**figure 52**). Because the voltage plateaued at farther distances (20 and 30 mm), proton diffusion must be rapid,

resulting in a homogeneous concentration of protons in these regions. Since proton concentration must be equal, if not greater near the boundary of the exclusion zone, the decrease in the voltage magnitude at 10 mm implies that the exclusion zone's negative electrical potential distribution may extend much further into the bulk water than previously measured. Similar, extensive microsphere-free exclusion zones have been observed growing into the bulk (**figure 27**, **46-47**) and provide supportive evidence for such long-range water ordering.

A next step in investigating this phenomenon is to see whether results are specific for the hydrophilic Nafion polymer, or if similar mechanical deflections are measured with other hydrophilic materials, such as biological surfaces. Nafion is a sufficient model for biological surfaces, such as intracellular protein, since it is not only highly charged and hydrophilic, but Nafion also absorbs a significant water volume (**figure 50**).

While exclusion zones have been repeatably observed next to Nafion and other, similar hydrophilic materials, a recent study compared exclusion zones to well-established unstirred layers (**figure 19**), which are found in biological environments adjacent to many diverse, biological surfaces. Hundreds of microns to millimeters in thickness, unstirred layers are a well-known example of long-range water ordering and are very similar to exclusion zones. Therefore, the charge separation phenomenon found with exclusion zones may additionally be a mechanism behind unstirred layers and other examples of long-range water ordering, such as the organization of water in hydrogels like PAMPS (**figure 15**). When hydrated, PAMPS consists of nearly 99.999% water

(3000:1 water-to-polymer weight ratio), but do not leak when held. Traditional views of the simple orientation of dipole water molecules along the hydrophilic polymer is not sufficient and also do not apply in light of recent spectroscopic evidence of ice-like water near hydrophilic surfaces (**figure 12**). A separation of charge and the development of significant electrostatic force at the interface may shed light on the nature of the bound water within hydrogel materials.

In solid state materials, charge separation is well-characterized at the P-N junction, or the interface between two adjacent semiconductor crystals. Diffusion of electrons (and hence separation of charge) from one crystal to the other is balanced by an opposing electric field in an interfacial area known as the depletion zone. The depletion zone is considered the lowest energy state of the semiconductor interface. Analogously, it is possible that proton diffusion from the exclusion zone is balanced by the developed mechanical force between the interfacial and bulk water regions as was measured in this study. While interfacial water has been spectroscopically measured to make up 10% of cell water, the result by many investigators is considered to be a lower-bound estimate. Therefore, if exclusion zones are found everywhere intracellularly, then the charge separation phenomenon may be as ubiquitous as there are interfaces and a process that occurs spontaneously at these interfaces. The mechanical forces measured here may therefore play an important role in biological processes including protein folding and transport, as well as macroscopic processes exhibited by organisms, such as adhesion, or water harvesting.

References

1. **A Yokota, K Tsumoto, M Shiroishi, H Kondo, and I Kumagai**. The role of hydrogen bonding via interfacial water Molecules in antigen-antibody complexation. *The Journal of Biological Chemistry* 278(7):5410-5418, Feb 2003.

2. **S-H Chong, and S Ham**. Impact of chemical heterogeneity on protein self-assembly in water. *Proceedings of the National Academy of Sciences of the United States of America* 109(20):7636-7641, May 2012.

3. **L Zhang, Y Yang, YT Kao, L Wang, and D Zhong**. Protein hydration dynamics and molecular mechanism of coupled water-protein fluctuations. *Journal of American Chemical Society* 131(30):10677-91, Aug 2009.

4. **A Garay-Arroyo, JM Colmenero-Flores, A Garciarrubio, and AA Covarrubias**. Highly hydrophilic proteins in prokaryotes and eukaryotes are common during conditions of water deficit. *The Journal of Biological Chemistry* 275(8):5668-5674, Feb 2000.

5. **GN Ling**. A Revolution in the Physiology of the Living Cell. Krieger Publishing Company, 1992.

6. **GH Pollack**. Cells, Gels and the Engines of Life. Ebner & Sons, 2001.

7. **GH Pollack**. The role of aqueous interfaces in the cell. *Advances in Colloid and Interface Science* 103(2):173-196, Apr 2003.

8. **F Despa, DP Orgill, and RC Lee**. Molecular crowding effects on protein stability. *Annals of New York Academy of Science* 1066:54-66, Dec 2005.

9. **S Honda, K Yamasaki, Y Sawada, and H Morii**. 10-residue folded peptide designed by segment statistics. *Structure* 12(8): 1507-1518, Aug 2004.

10. **K Wang, R Ramirez-Mitchell, and D Palter**. Titin is an extraordinarily long, flexible, and slender myofibrillar protein. *Proceedings of the National Academy of Sciences of the United States of America* 81(12):3685-3689, Jun 1984.

11. **HF Fisher**. A limiting law relating the size and shape of protein molecules to their composition. *Proceedings of the National Academy of Sciences of the United States of America* 51(6):1285-1291, Jun 1964.

12. **JS Clegg**. Intracellular water and the cytomatrix: some methods of study and current views. *The Journal of Cell Biology* 99(1-2):167-171, Jul 1984.

13. **MW Jernega**. Benjamin Franklin's "electrical kite" and "lightning rod". *The New England Quarterly* 1(2):180-196, Apr 1928.

14. **CB Moore, W Rison, J Mathis, and G Aulich**. Lightning rod improvement studies. *Journal of Applied Meteorology* 39(5):593-609, Apr 1999.

15. **Open Stax College**. Conductors and electric fields in static equilibrium. http://cnx.org/content/m42317/latest/?collection=col11406/latest

16. **NS Pesika, H Zeng, K Kristiansen, B Zhao, Y Tian, K Autumn, and J Israelachvili**. Gecko adhesion pad: a smart surface? *Journal of Physics* 21(46):4641321-4641326, Nov 2009.

17. **Y Vaknin, S Gan-Mor, A Bechar, B Ronen, and D Eisikowitch**. The role of electrostatic forces in pollination. *Plant Systematics and Evolution* 222:133-142, 2000.

18. **RP Garrod, LG Harris, WC Schofield, J McGettrick, LJ Ward, DO Teare, and JP Badyal**. Mimicking a Stenocara beetle's back for microcondensation using plasmachemical patterned superhydrophobic-superhydrophilic surfaces. *Langmuir* 23(2):689-693, Jan 2007.

19. **M Griffith and MW Yaish**. Antifreeze proteins in overwintering plants: a tale of two activities. *Trends in Plant Science* 9(8):399-405, Aug 2004.

20. **Wikipedia commons**. Close-up view of Gecko foot on glass surface. http://upload.wikimedia.org/wikipedia/commons/thumb/b/b2/Gecko_foot_on_glass.JPG/250px-Gecko_foot_on_glass.JPG

21. **A Dafni, M Hesse, and E Pacini**. Pollen and Pollination. Springer, 2000.

22. **Digital Ecologies**. http://digitalecologies2011.wordpress.com/teams/yu-brittnay-log-1/log-5/

23. **H Helmholtz**. *Pogg. Ann.* 89:211, 1853.

24. **PC Hiemenz**. Principles of Colloid and Surface Chemistry. Marcel Dekker, 1977.

25. **JThG Overbeek**. Recent developments in the understanding of colloid stability. *Journal of Colloid and Interface Science* 58(2), 408-422, Feb 1977.

26. **G Gouy**. *J. Phys.* 9:457, 1910.

27. **DL Chapman**. *Philos. Mag.* 25:475, 1913.

28. **OZ Stern**. *Electrochem.* 30:508, 1924.

29. **BV Derjaguin, and L Landau**. Theory of the stability of strongly charged lyophobic sols and of the adhesion of strongly charged particles in solutions of electrolytes. *Acta. Phys. Chim. URSS* 14:633-662, 1941.

30. **JN Israelachvili**. Intermolecular and Surface Forces. Elsevier, 2011.

31. **D Kopeliovich**. Stabilization of colloids. http://www.substech.com/dokuwiki/doku.php?id=stabilization_of_colloids

32. **P Ghosh**. Colloid and Interface Science. PHI Learning Private Limited, 2009.

33. **H Butt, and M Kappl**. Surface and Interfacial Forces. Wiley-VCH, 2010.

34. **M Bostrom, DRM Williams, and BW Ninham**. Specific ion effects: why DLVO theory fails for biology and colloid systems. *Physical Review Letters* 87(16):1681031-1681034, Oct 2001.

35. **BW Ninham**. On progress in forces since the DLVO theory. *Advances in Colloid and Interface Science* 83(1-3):1-17, Dec 1999.

36. **V Subramanian**. Effects of long-chain surfactants, short-chain alcohols and hydrolyzable cations on the hydrophobic and hydration forces. *PhD Thesis*, Virginia Technical Institute, 1998.

37. **EA Vogler**. Structure and reactivity of water at biomaterial surfaces. *Advances in Colloid and Interfacial Science* 74:69-117, Feb 1998.

38. **PM Wiggins**. Role of water in some biological processes. *Microbiological Reviews* 54(5):432-449, Dec 1990.

39. **HJ Bakker, MF Kropman, and AW Omta**. Effect of ions on the structure and dynamics of liquid water. *Journal of Physics* 17(45):S3215-S3224, Oct 2005.

40. **L He, Y Hu, M Wang, and Y Yin**. Determination of solvation layer thickness by a magnetophotonic approach. *ACS Nano* 6(5):4196-4202, Apr 2012.

41. **J Israelachvili**. Direct measurements of forces between surfaces in liquids at the molecular level. *Proceedings of the National Academy of Sciences of the United States of America* 84(14):4722-4724, Jul 1987.

42. **J Israelachvili, and Hakan Wennerstrom**. Role of hydration and water structure in biological and colloidal interactions. *Nature* 379(6562):219-225, Jan 1996.

43. **RG Horn, and JN Israelachvili**. Direct measurement of structural forces between two surfaces in a nonpolar liquid. *Journal of Chemical Physics* 75(3):1400-1411, Aug 1981.

44. **JN Israelachvili, and PM McGuiggan**. Forces between surfaces in liquids. *Science* 241(4867):795-800, Aug 1988.

45. **University of Washington, Department of Materials Science and Engineering**. Electrostatic stabilization of colloids. http://depts.washington.edu/solgel/pages/courses/MSE_502/Electrostatic_Stabilization.html

46. **Wikipedia commons**. Salt content of sea water. http://en.wikipedia.org/wiki/Seawater

47. **Water conductivity**. http://www.lenntech.com/water-conductivity.htm

48. **P Whitehead**. Ultra-pure water for ion chromatography. *Journal of Chromatography* A 770(1-2):115-118, May 1997.

49. **Ergonomic Laboratory Equipment**. High purity water for inorganic analysis. http://www.labmanager.com/?articles.view/articleNo/3156/article/High-Purity-Water-for-Inorganic-Analysis

50. **DB Asay, and SH Kim**. Evolution of the adsorbed water layer structure on silicon oxide at room temperature. *Journal of Physical Chemistry B* 109 (35):16760-16763, Aug 2005.

51. **MR Yalamanchili, AA Atia, and JD Miller**. Analysis of interfacial water at a hydrophilic silicon surface by in-situ FTIR/internal reflection spectroscopy. *Langmuir* 12(17):4176-4184, Aug 1996.

52. **V Ostroverkhov, GA Waychunas, and YR Shen**. New information on water interfacial structure revealed by phase-sensitive surface spectroscopy. *Physical Review Letters* 94(4): 0461021-0461024, Feb 2005.

53. **Q Du, E Freysz, and YR Shen**. Vibrational spectra of water molecules at quartz/water interfaces. *Physical Review Letters* 72(2):238-241, Jan 1994.

54. **M Sovago, and M Bonn**. Interfacial water structure studied by vibrational sum frequency generation. Andor Technology, Nov 2009.

55. **JA Curcio, and CC Petty**. The near infrared absorption spectrum of liquid water. *Journal of the Optical Society of America* 41(5):302-304, May 1951.

56. **JB Hasted, SK Husain, FAM Frescura, and JR Birch**. Far-infrared absorption in liquid water. *Chemical Physics Letters* 118(6):622-625, Aug 1985.

57. **W Chen**. X-ray absorption and infrared spectra of water and ice: a first-principles electronic structure study. *PhD Thesis*, Princeton University, Sep 2009.

58. **V Hollis**. Non-invasive monitoring of brain tissue temperature by near-infrared spectroscopy. *PhD Thesis*, University College London, Dec 2002.

59. **M Chaplin**. Water structure and science. http://www.lsbu.ac.uk/water/vibrat.html

60. **NJ Harrick**. Internal Reflection Spectroscopy. Marcel Dekker, Inc., 1987.

61. **MP Goertz, JE Houston, and X-Y Zhu**. Hydrophilicity and the viscosity of interfacial water. *Langmuir* 23(10):5491-5497, Feb 2007.

62. **Y Zhu, and S Granick**. Viscosity of interfacial water. *Physical Review Letters* 87(9):0961041-0961044, Aug 2001.

63. **JE Houston, and TA Michalske**. The interfacial-force microscope. *Nature* 356:266-267, Mar 1992.

64. **JV Alsten, and S Granick**. Molecular tribometry on ultrathin liquid films. *Physical Review Letters* 61(22):2570-2573, Nov 1988.

65. **S Granick**. Motions and relaxations of confined liquids. *Science* 253(5026):1374-1379, Sep 1991.

66. **Q Li**. Interfacial force microscope. Carpick Group.

67. **JC Henniker**. Depth of the surface zone of a liquid. *Review of Modern Physics* 21(2):322-341, Apr 1949.

68. **W Drost-Hansen**. Aqueous interfaces - methods of study and structural properties, part I. *Industrial and Engineering Chemistry* 57(3):38-44, Mar 1965.

69. **W Drost-Hansen**. Aqueous interfaces - methods of study and structural properties, part II. *Industrial and Engineering Chemistry* 57(4):18-37, Apr 1965.

70. **W Drost-Hansen**. Structure of water near solid interfaces. *Industrial and Engineering Chemistry* 61(11):10-47, Nov 1969.

71. **RM Pashley, and JA Kitchener**. Surface forces on adsorbed multilayers of water on quartz. *Journal of Colloid and Interface Science* 71(3):491-500, Oct 1970.

72. **M Tschapek, S Falasca, and C Wasowski**. The undrainable water in quartz sand and glass beads. *Powder Technology* 42(2):175-180, May 1985.

73. **D Fologea, B Ledden, DS McNabb, and J Lib**. Electrical characterization of protein molecules by a solid-state nanopore. *Applied Physics Letters* 91(5):0539011-0539013, Jul 2007.

74. **T Peters, Jr**. Serum Albumin. *Advances in Protein Chemistry* 37:161-245, 1985.

75. **DC Carter, and JX Ho**. Structure of serum albumin. *Advances in Protein Chemistry* 45:153-203, 1994.

76. **Y Osada, and J Gong**. Stimuli-responsive polymer gels and their application to chemomechanical systems. *Progress in Polymer Science* 18(2):187-226, 1993.

77. **Y Osada, and S Ross-Murphy**. Intelligent gels. *Scientific American* 268(5):42-47, May 1993.

78. **N Pernodet, M Maaloum, and B Tinland**. Pore size of agarose gels by atomic force microscopy. *Electrophoresis* 18(1):55-58, 1997.

79. **MM Ozmen, and O Okay**. Superfast responsive ionic hydrogels with controllable pore size. *Polymer* 46(19):8119-8127, Sep 2005.

80. **M Sadeghi, and H Hosseinzadeh**. Synthesis and super-swelling behavior of a novel low salt-sensitive protein-based superabsorbent hydrogel: collagen-g-poly(AMPS). *Turkish Journal of Chemistry* 34:739-752, Apr 2010.

81. **JD Bernal, and CH Carlisle**. Unit cell measurements of wet and dry crystalline turnip yellow mosaic virus. *Nature* 162:139-140, Jul 1948.

82. **H Stebbings, and C Hunt**. The nature of the clear zone around microtubules. *Cell and Tissue Research* 227(3):609-617, 1982.

83. **CF Hazlewood, BL Nichols, and NF Chamberlain**. Evidence for the existence of a minimum of two phases of ordered water in skeletal muscle. *Nature* 22:747-750, May 1969.

84. **DE Woessner, and BS Snowden Jr**. A pulsed NMR study of dynamics and ordering of water molecules in interfacial systems. *Annals of the New York Academy of Sciences* 204:113-124, Mar 1973.

85. **SR Kasturi, DC Chang, and CF Hazlewood**. Study of anisotropy in nuclear magnetic resonance relaxation times of water protons in skeletal muscle. *Biophysical Journal* 30(3): 369-381, Jun 1980.

86. **S Zimmerman, AM Zimmerman, GF Fullerton, RF Luduena, and IL Cameron**. Water ordering during the cell cycle: nuclear magnetic resonance studies of the sea-urchin egg. *Journal of Cell Science* 79:247-257, Nov 1985.

87. **A Bausch, W Moller, and E Sackmann**. Measurement of local viscoelasticity and forces in living cells by magnetic tweezers. *Biophysical Journal* 76(1):573-579, Jan 1999.

88. **VM Laurent, E Planus, R Fodil, and D Isabey**. Mechanical assessment by magnetocytometry of the cytosolic and cortical cytoskeletal compartments in adherent epithelial cells. *Biorheology* 40:235-240, 2003.

89. **GN Ling**. On the large error introduced in the estimate of the density of membrane pores from permeability measurements when diffusion in "unstirred layer" within the cells is disregarded. *Physiological Chemistry and Physics and Medical NMR* 19(3):199-207, 1987.

90. **AA Noyes, and WR Whitney**. *Z. Physik. Chem.* 23:689, 1897.

91. **W Nernst**. Theorie der Reaktionsgerschwindkeit. *Heterogemem Systemem 7 Phys. Chem.* 47:52-55, 1904.

92. **GH Pollack, and J Clegg**. Unexpected linkage between unstirred layers, exclusion zones and water. Phase Transitions in Cell Biology, Springer 2008.

93. **K Green, and T Otori**. Direct measurements of membrane unstirred layers. *Journal of Physiology* 207(1):93-102, Mar 1970.

94. **P Pohl, SM Saparovand, and YN Antonenko**. The size of the unstirred layer as a function of the solute diffusion coefficient. *Biophysical Journal* 75(3):1403-1409, Sep 1998.

95. **IJ Hidalgo, KM Hillgren, GM Grass, and RT Borchardt**. Characterization of the unstirred water layer in Caco-2 cell monolayers using a novel diffusion apparatus. *Pharmaceutical Research* 8(2):222-227, Feb 1991.

96. **FA Smith, and NA Walker**. Photosynthesis by aquatic plants: effects of unstirred layers in relation to assimilation of CO2 and HCO3- and to carbon isotopic discrimination. *New Phytologist* 86(3):245-259, Nov 1980.

97. **RI Sha'afi, GT Rich, VW Sidel, W Bossert, and AK Solomon**. The effect of the unstirred layer on human red cell water permeability. *Journal of General Physiology* 50(5):1377-1399, May 1967.

98. **T Korjamo, AT Heikkinen, and J Monkkonen**. Analysis of unstirred water layer in vitro permeability experiments. *Journal of Pharmaceutical Sciences* 98(12):4469-4479, Dec 2009.

99. **M Lherminier, and F Alvarado**. Virtual elimination of the interference of unstirred water layers on intestinal sugar transport kinetics by use of the tissue accumulation method at appropriate shaking rates. *Pflugers Archiv* 389(2):155-158, Jan 1981.

100. **H Yuasa, T Iga, M Hanano, and J Watanabe**. Comparative assessment of the resistance of the unstirred water layer to solute transport between two different intestinal perfusion systems. *Biochimica et Biophysica Acta* 938(2):189-198, Feb 1988.

101. **D Winne**. Unstirred layer, source of biased Michaelis constant in membrane transport. *Biochimica et Biophysica Acta* 298(1):27-31, Feb 1973.

102. **D Winne, S Kopf, and ML Ulmer**. Role of unstirred layer in intestinal absorption of phenylalanine in vivo. *Biochimica et Biophysica Acta* 550(1):120-130, Jan 1979.

103. **CU Cotton, and L Reuss**. Measurement of the effective thickness of the mucosal unstirred layer in Necturus gallbladder epithelium. *The Journal of General Physiology* 93(4):631-647, Apr 1989.

104. **JM Zheng, and GH Pollack**. Long-range forces extending from polymer-gel surfaces. *Physical Review Letters E* 68(3):0314081-0314087, Sep 2003.

105. **J Zheng, and GH Pollack**. Solute exclusion and potential distribution near hydrophilic surfaces. Water and the Cell, 2006.

106. **JM Zheng, WC Chin, E Khijniak, E Khijniak, Jr, and GH Pollack**. Surfaces and interfacial water: evidence that hydrophilic surfaces have long-range impact. *Advances in Colloid and Interfacial Science* 127(1):19-27, Nov 2006.

107. **BH Chai, JM Zheng, Q Zhao, and GH Pollack**. Spectroscopic studies of solutes in aqueous solution. *The Journal of Physical Chemistry A* 112(11):2242-2247, Feb 2008.

108. **I Klyuzhin, A Symonds, J Magula, and GH Pollack**. New method of water purification based on the particle-exclusion phenomenon. *Environmental Science and Technology* 42(16):6160-6166, Aug 2008.

109. **J-M Zheng, A Wexler, and GH Pollack**. Effect of buffers on aqueous solute-exclusion zones around ion-exchange resins. *Journal of Colloid and Interfacial Science* 332(2):511-514, Apr 2009.

110. **B Chai, H Yoo, and GH Pollack**. Effect of radiant energy on near-surface water. *Journal of Physical Chemistry B* 113(42):13953-13958, Sep 2009.

111. **DT Nhan, and GH Pollack**. Effect of particle diameter on exclusion-zone size. *International Journal of Design & Nature and Ecodynamics* 6(2):139-144, Jun 2011.

112. **ME Fauver, DL Dunaway, DH Lilienfeld, HG Craighead, and GH Pollack**. Microfabricated cantilevers for measurement of subcellular and molecular forces. *IEEE Transactions on Biomedical Engineering* 45(7):891-898, Jul 1998.

113. **Wikipedia commons**. Water absorption spectrum. http://en.wikipedia.org/wiki/Electromagnetic_absorption_by_water

114. **C Heitner-Wirguin**. Recent advances in perfluorinated ionomer membranes: structure, properties and applications. *Journal of Membrane Science* 120(1):1-33, Dec 1998.

115. **R Basnayake, GR Peterson, DJ Casadonte, Jr, and C Korzeniewski**. Hydration and interfacial water in Nafion membrane probed by transmission infrared spectroscopy. *Journal of Physical Chemistry B* 110(47):23938-23943, Nov 2006.

116. **S Goswami, S Klaus, and J Benziger**. Wetting and absorption of water drops on Nafion films. *Langmuir* 24(16):8627-8633, Jul 2008.

117. **JG Pharoah, OS Burheim, PJS Vie, and S Kjelstrup**. Thermal effects in PEMFCS. *Abstract*. 2009.

118. **AA Shah, TR Ralph, and FC Walsh**. Modeling and simulation of the degradation of perfluorinated ion-exchange membranes in PEM fuel cells. *Journal of the Electrochemical Society* 156(4):B465-B484, Feb 2009.

119. **K Kunimatsu, B Bae, K Miyatake, H Uchida, and M Watanabe**. ATR-FTIR study of water in Nafion membranes combined with proton conductivity measurements during hydration/dehydration cycle. *Journal of Physical Chemistry B* 115(15):4315-4321, Apr 2011.

120. **P Majsztrik, A Bocarsly, and J Benziger**. Water permeation through Nafion membranes: the role of water activity. *Journal of Physical Chemistry B* 112(51):16280-16289, Oct 2008.

VITA

Ronnie Das

Education

Doctor of Philosophy in Bioengineering — 2012
University of Washington, Seattle

Master of Science in Bioengineering — 2006
University of Illinois at Chicago

Bachelor of Science in Bioengineering — 2002
University of California, San Diego

Work Experience

Donald W. and Joan P. Baker Fellow — 2012-2013
University of Washington, College of Engineering

Research Associate / Lab Manager — 2006-2012
University of Washington, Department of Bioengineering

Research Associate — 2004-2006
University of Illinois at Chicago, Department of Bioengineering

Research Bioengineer I — 2003-2004
Veterans Affairs Medical Center San Diego

Technician / Research Associate I — 2001-2003
Neurocrine Biosciences, Inc.

Laboratory Assistant — 2001
The Scripps Research Institute

Educational Counselor — 1997-2003
Score! Educational Center

Academic Experience

Lab Instructor 2009
University of Washington, Department of Bioengineering, Bioinstrumentation / Lab

Teaching Assistant / Lab Instructor 2009
University of Washington, Department of Bioengineering, Bioengineering Systems Analysis / Lab

Teaching Assistant 2007
University of Washington, Department of Bioengineering, Biostatistics

MATLAB Instructor 2006
University of Illinois at Chicago, Department of Bioengineering, Bioinstrumentation I / II

Undergraduate Supervisor 2005-2006
University of Illinois at Chicago, NSF REU/RET Program

BioE Department High School Internship Coordinator 2004-2006
University of Illinois at Chicago, Department of Bioengineering

Publications

C Wang, E Nagornyak, **R Das**, GH Pollack. Automatic step-detection algorithm for analysis of sarcomere dynamics. *Comput Methods Biomech Biomed Engin* 11(6):609-614, 2008.

R Das, D Gandhi, S Krishnan, L Saggere, PJ Rousche. A benchtop system to assess cortical neural interface micromechanics. *IEEE Trans Biomed Eng* 54(6):1089-1096, 2007.

TJ Patel, **R Das**, J Fridén, GJ Lutz, RL Lieber. Sarcomere strain and heterogeneity correlate with injury to frog skeletal muscle fiber bundles. *J Appl Physiol* 97:1803-1813, 2004.

RE Petroski, JE Pomeroy, **R Das**, H Bowman, W Yang, AP Chen, AC Foster. Indiplon is a high-affinity positive allosteric modulator with selectivity for α_1 subunit-containing $GABA_A$ receptors. *J Pharmacol Exp Ther* 317:369-377, 2006.